University of California, Merced

Modeling the tribochemical mechanisms of sulfur-containing lubricant additives

by
Karen Mohammadtabar

2022

Committee:
Professor Mehmet Baykara (chair)
Professor Ashlie Martini (advisor)
Professor David Strubbe
Professor James Palko

A dissertation submitted in partial satisfaction of the requirements for the degree of Doctor of Philosophy
in
Mechanical Engineering

This dissertation of Karen Mohammadtabar is approved, and it is acceptable in quality and form for publication on microfilm and electronically:

Professor Ashlie Martini, Advisor	Date
Professor Mehmet Z. Baykara	Date
Professor David A. Strubbe	Date
Professor James Palko	Date

Contents

List of Figures

List of Tables

Acknowledgements

This work was supported by the Austrian COMET-Program (K2 Project InTribology, no. 872176, project coordinator AC2T research GmbH) and partially carried out at the "Excellence Centre of Tribology" (AC2T research GmbH). The computational results presented were achieved in part using the Vienna Scientific Cluster (VSC). Computing resources were also provided by the Multi-Environment Computer for Exploration and Discovery (MERCED) cluster at UC Merced, funded by National Science Foundation Grant No. ACI-1429783.

Curriculum Vita

Education

- Ph.D. (Expected graduation: Fall 2022) in Mechanical Engineering – University of California, Merced, CA
- M.Sc. in Physics – The University of Akron, OH
- B.SC. in Physics – The University of Tehran, Tehran

Publications

- K. Mohammadtabar et al. "Reactive molecular dynamics simulations of thermal film growth from di-*tert*-butyl disulfide on an Fe(100) surface". In: *Langmuir* 34 (2018), pp. 15681–15688
- A. Khajeh et al. "Statistical analysis of tri-cresyl phosphate conversion on an iron oxide surface using reactive molecular dynamics simulations". In: *J. Phys. Chem. C* 123.20 (2019), pp. 12886–12893
- K. Mohammadtabar et al. "Heat-, load-, and shear-driven reactions of di-tert-butyl disulfide on Fe(100)". In: *J. Phys. Chem. C* 123(32) (2019), pp. 19688–19692
- Karen Mohammadtabar et al. "Shear-driven reactions of organosulfur compounds on ferrous surfaces: A molecular dynamics study". In: *Tribology International* 176 (2022), p. 107922

Conference Presentations and Posters

- STLE 76th Annual Meeting Exhibition, Orlando, Florida (Oral presentation), 2022
- STLE Virtual Annual Meeting Exhibition (Oral presentation), 2021
- STLE 75th Annual Meeting Exhibition, Chicago, Illinois (Oral presentation), 2020
- STLE 74th Annual Meeting Exhibition, Nashville, Tennessee (Oral presentation), 2019
- Tribology Frontiers Conference, Chicago, Illinois (Poster presentation), 2018

Modeling the tribochemical mechanisms of sulfur-containing lubricant additives

Karen Mohammadtabar, Ph.D.

University of California, Merced, 2022

Chair of committee: Professor Mehmet Z. Baykara

Abstract

Lubricant additives are chemical compounds that are added to lubricant formulations to enhance their performance. Sulfur-containing additives are an important family of these compounds that increase the life of mechanical components by creating a protective film on surfaces in relative motion to prevent direct metal-metal contact. These additives are widely used in the industry whenever a mechanical system is subject to extreme pressure or wear, but the mechanisms and conditions by which the protective films form are not yet fully understood. This dissertation seeks to address this from an atomistic point of view by investigating the tribochemical reactions between additives and surfaces using reactive molecular dynamics simulations. First, the reactions between a representative sulfur-containing additive (di-*tert*-butyl disulfide) and an iron(100) surface is modeled. Results show that film formation reaction proceeds through three main steps, S–S bond cleavage, Fe–S bond formation, and S–C bond dissociation. These are start of the formation of an iron sulfide layer that can provide protection for the iron surface. The effect of mechanical force on activating chemical reactions is investigated. It is found that mechanical force assists the initiation and the acceleration of these chemical reactions by lowering the reaction energy barrier. Next, a model base oil, dodecane, and an iron oxide surface are modeled to increase the physical realism of the simulations of tribochemical reactions on ferrous surfaces. Results show that this base oil does not chemically interfere with the film formation reaction, however, the physical presence of the base oil molecules impedes the reaction. Conversely, the oxide surface directly changes the reaction pathways that lead to film formation. The oxidation of the additive molecules, their decomposition products, and the surface introduces intermediate steps and reduces the rate at which reactions occur. The kinetics of the reactions are studied in the context of the Bell model and results reveal that the reactions between additives and ferrous surfaces are mechanochemical in nature, and that mechanical force facilitates these reactions by moving the reactants laterally on the surface, weakening their chemical bonds. Finally, another sulfur-containing lubricating material, MoS_2, is studied. First, a ReaxFF force field is developed for Ni-doped MoS_2. The force field is shown to accurately capture material parameters such as bond lengths, lattice constants, and dopant relocation in the presence of vacancies. Lastly, the applicability and accuracy of the force field is demonstrated by modeling the process of deposition and annealing Ni-doped MoS_2 in a reactive molecular dynamics simulation. Overall, the results presented in this dissertation contribute to the understanding of the mechanisms by which sulfur-containing additives function and are an important step towards rational design of more energy efficient and longer lasting lubricated mechanical systems.

Chapter 1

Introduction

1.1 Background

1.1.1 Mechanochemistry and tribochemistry

Chemical reactions are known to be activated by thermal energy. They can also be activated by mechanical energy that is provided to a reaction by external force. [5, 6, 7, 8] Such force can have several effects on the reactions including introducing new reaction pathways [9, 10, 9, 11] and lowering reaction energy barriers. [12, 13, 1] The study of the activation of chemical reactions by mechanical force is called mechanochemistry. [5, 6, 12, 14, 15, 16] Mechanochemistry is relevant to many applications such as synthesis of organic compounds [6, 17, 18], oxides [19, 20], and metal complexes [21, 22], as well as in catalysis [23, 24] and surface reactions. [25, 26, 27, 28, 29, 30] Since mechanical forces are inherent to sliding surfaces, here we focus on mechanochemical reactions that occur between sliding surfaces.

Tribochemistry is the study of chemical reactions that happen at tribological interfaces (between surfaces in relative motion) that are induced by conditions inherent to these interfaces such as shear force and flash temperature rise caused by friction. Tribochemistry is relevant to, for example, coating materials, [31, 32], metalworking processes, [33, 34] and lubricant components. [35, 36, 37, 38] Here we focus on the applications of tribochemistry in reactions of additives with surfaces.

1.1.2 Liquid lubricant additives

Additives are synthetic chemical substances added to lubrication formula that enhance the performance of a base fluid in different ways. Additives can function by influencing the physical and chemical properties of the base fluid or by influencing the physiochemical properties of metal surfaces to provide friction reduction, wear protection, and corrosion inhibition.

The most basic function of lubricating oils is to create a liquid layer between moving surfaces to protect them from direct contact during relative motion. When the liquid between the mechanical parts does not completely separate the moving surfaces, anti-wear (AW) and extreme pressure (EP) additives form protective layers on metal surfaces to reduce wear. There are various compounds that have AW/EP effects. These include organic sulfur and phosphorus compounds, calcium and sodium salts, chlorine compounds, and ionic liquids. [39, 40] Examples of additives based on organic compounds are zinc dialkyl dithiophosphate (ZDDP), tricresyl phosphate (TCP), trixylyl phosphate (TXP) and dilauryl phosphate that have been proven to be good AW and EP additives. They usually contain *"active"* elements such as sulfur and phosphorus for strong adsorption. [41]

In addition to organic compounds, salts such as borates (e.g., calcium borate) have shown not only good extreme pressure and anti-wear properties, but also to be non-toxic and odorless as well as exhibit good thermal oxidation stability, anti-corrosion and anti-rust properties. [42] Moreover, the excellent AW/EP properties of chlorine compounds have been conventionally explained by their ability to coat metal surfaces with a low shear strength metal chloride film under the influence of high pressure and in the presence of traces of moisture. [39]

Ionic liquids have also recently been reported as AW additives for their effective wear reduction. Their wear protection ability, which has been shown to be comparable to the commonly

used additive ZDDP, has made them an interesting focal point for tribology researchers. [37, 40, 43, 44]

One of the most important families of AW/EP additives are sulfur-containing additives. Elemental sulfur has been added to metalworking fluids to improve EP properties since the beginning of lubrication. Sulfur containing additives are divided into two types: active and inactive. The active sulfur carriers have higher reactivity and hence provide better protection, specially at lower temperatures. The downside of active sulfur additives is that they are corrosive to some metals. The inactive type of sulfur-containing additives possess relatively stable S–C bonds which will react at elevated temperatures only. [45] The mechanism of both active and inactive sulfur carriers under EP conditions can be described as physical adsorption followed by chemisorption and finally cleavage of the sulfur and its reaction with the metal surface (Fig. 1.1). Generally, this reaction takes place at temperatures over 600°C. [46] We will be focusing on the reactions between sulfur containing additives and surfaces, their pathways and kinetics.

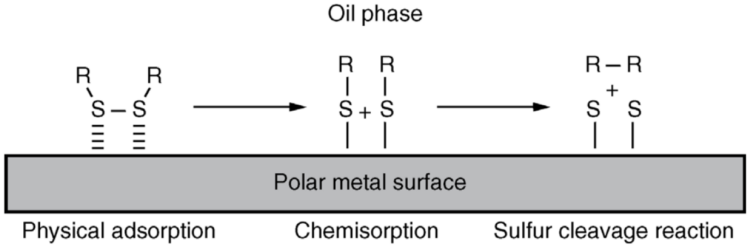

Figure 1.1: Mechanism of sulfur-containing additives under extreme pressure conditions (image from ref. [39])

1.1.3 Solid lubricants

There are some conditions under which the liquid lubricants are improved by the addition of or even replaced by low friction solid materials. These conditions include aerospace/space applications where low temperatures cause liquid lubricants to freeze, dry machining where use of a large amount of liquid lubricant is not cost effective, and food processing where contamination by liquid lubricants is a health hazard. [47] Their stability under extreme pressure, temperature and chemically reactive environments along with their resistance to deterioration in storage have made solid lubricants very popular. For example, graphite with its hexagonal crystal structure provides low friction and easy shear due to its weakly bonded layers. Graphite is thermally stable at very high temperatures (2300 K and above) [48] but since graphite needs moisture to achieve low friction the practical temperature of operation is limited to 900 K. The same need for moisture limits the use of graphite in dry environments, specifically vacuum or space. [49] An example of a solid lubricant that can be used in vacuum is Polytetrafluoroethylene (PTFE). PTFE's lack of chemical activity makes it a good candidate to be used in both atmosphere and vacuum. [50, 51] Unlike graphite, PTFE does not rely on sliding layers to provide low friction. The low surface energy of PTFE enables the macromolecules to move relative to each other easily, ultimately providing very low friction coefficients. [52] The limitations of PTFE are its low load carrying capacity and durability along with its low thermal stability. [53]

Among solid lubricants, MoS_2 has shown great performance in providing lubrication to surfaces. MoS2 can be used as a dry lubricant by itself or as an additive in oils and greases. [47] Its high thermal stability, greater load-carrying capacity compared to its alternatives, and the ability to perform without a humid environment, makes this lubricant very interesting to many researchers. MoS_2 is a transition metal dichalcogenide with a layered structure where each layer consists of molybdenum atoms sandwiched between sulfur atoms. Three main applications of the material are in catalysis, opto-electronics and tribology. In catalysis, the chemically active edges of MoS_2 nanoparticles have been used to catalyze various reactions, including, hydrogen evolution, [54] hydrotreatment of oil,[55] and pollutant removal. [56, 57] Additionally, in 2D form, MoS_2 is widely used as a catalyst for hydrogen evolution reactions [58, 59, 60] and CO_2 reduction. [61, 62, 63, 64] In opto-electronics, single-layer MoS_2 is a semiconductor with a direct band gap that can be used to construct high efficiency transistors. [65, 66] MoS_2 can be synthesized by chemical vapor deposition to form large-area monolayers for use as atomically thin optical and photovoltaic devices. [67] In tribology, the weak van der Waals forces between

layers provide low shear resistance, making MoS_2 an effective low-friction solid lubricant or, in nanoparticle form, a liquid lubricant additive. [47, 68, 69, 70]

MoS_2 can be doped to enhance its properties. There are four meta-stable sites for a dopant in the MoS_2 crystallographic structure. [71] Dopants can replace an Mo or an S atom in the crystal structure or they can be intercalated between MoS_2 layers either below a sulfur atom (tetrahedral) or below a hexagonal hole (octahedral). Many different elements have been explored as possible MoS_2 dopants, particularly transition metals. [47, 72, 73] Ni, Cr, Ti, Au, Zr, and Sb_2O_3 have shown to improve tribological performance of MoS_2 in terms of friction reduction and wear resistance. [74, 47, 75, 76, 77] Among these elements, it has been shown that MoS_2 films co-sputtered with Ni compare favorably to undoped MoS_2 in terms of friction, wear and useful life of mechanical parts. [78, 79, 80, 81] Ni-doped MoS_2 has also been shown to improve the tribological performance of coatings at low temperatures, which makes Ni-doped MoS_2 ideal as a solid lubricant for space applications where performance at extreme conditions is critical. [74, 82]

1.1.4 Tribofilms

Tribofilms are protective films that form between tribological surfaces. These films decrease friction and wear when a liquid lubricant can no longer entirely separate two surfaces in relative motion. Formation of such films has been shown to be a result of reactions between the lubricant additives and surfaces. [83]

Many studies have shown that tribofilms contain elements both from the additives and surfaces. [84, 85, 86, 87, 88] In mechanical components, the most common materials are ferrous which make it reasonable to have elements such as iron in the tribofilms formed on these surfaces. But since surfaces and the lubricant additives themselves contain many different elements, tribofilms have been reported to contain iron, sulfur, oxygen, carbon, phosphorus, and zinc. [84, 89, 90]

For sulfur-containing chemicals reaction with ferrous surfaces can lead to formation of iron-sulfide films. It has been shown that iron-sulfide films have many application such as solar energy, [91, 92] water treatment, [93, 94] corrosion, [95, 96] and tribology. [97, 98, 99] In tribology, iron-sulfide films have shown to decrease friction between surfaces. [100, 101] It has been shown that, with increasing concentration of sulfide on surfaces, wear decreases, which consequently increases the lifetime of the mechanical parts (Fig. 1.2). [102] Since tribological surfaces are subject to harsh conditions, such as high temperature, wear, and friction, the performance of additives (or lubricants in general) can be determined by their ability to form protective tribofilms.

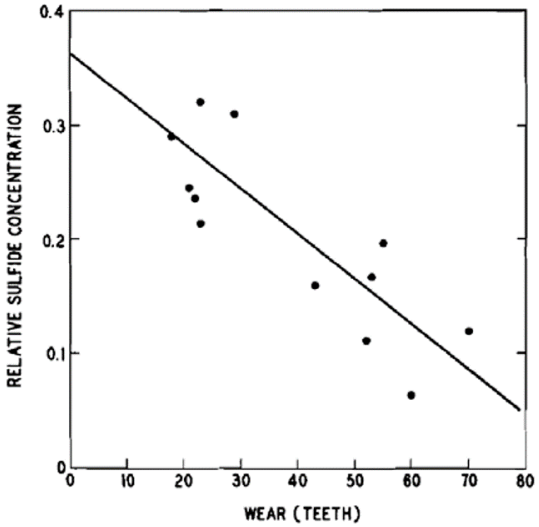

Figure 1.2: Reduction in concentration of sulfur in iron-sulfide film as a function of wear. Results show that wear decreases with increasing sulfur content in the tribofilm. Image from ref. [102]

The tribofilms formed from the reactions between these additives and surfaces are believed to be induced by mechanical forces that are inherent to tribological interfaces. Reactions between

additives and surfaces can be activated by heat generated by friction in the interface as well as mechanical force on the contact. [103, 104, 105] Many studies have been carried out to investigate the effect of force on film formation, however, the mechanisms by which the mechanical force activates these reactions are not yet fully understood.

1.2 Effect of force on film formation reactions

The effect of force on rate of chemical reactions has been studied in the context of mechanochemistry. In tribological interfaces, these are forces that exist between surfaces in relative motion, particularly, shear (friction) force. It has been shown that force accelerates these surface reactions by lowering the reaction energy barrier (and hence the amount of energy required to initiate the reaction) or opening new reaction pathways. Specifically related to lubricant additives, shear force has shown to increase the rate of reaction for ZDDP on steel [105], iron [106], silicon [107], and other non-ferrous surfaces [108], as well as for dimethyl disulfide [109, 110], diethyl disulfide, and dimethyl trisulfide on copper [111]. The effect of shear force (or force in general) on acceleration of reaction is often studied in the context of the Bell model. [112]

The Bell equation assumes a linear relationship for the lowering of a reaction energy barrier by mechanical force. [112]

$$E(F) = E_0 - \Delta x^{\ddagger} \times F \ , \tag{1.1}$$

In this equation, $E(F)$ is the reaction energy barrier as a function of force F, E_0 is the energy barrier in the absence of force, and $\Delta x^{\ddagger}$ is the activation length, i.e., the distance between reactant and transition states along the reaction coordinate. Together, $\Delta x^{\ddagger} \times F$ is the work done by the force along the reaction coordinate. This is the amount of energy that is provided to the reaction by the mechanical force which reduces the height of the energy barrier necessary to initiate the reaction. The Bell model has been used in tribochemistry to investigate the role of mechanical force in film formation reactions. The Bell equation has been used to describe the reduction of activation energy of film formation reactions in experiments for ZDDP on tungsten carbide [103] and oxygen-rich species on graphene sheets [27] as well as in computational studies for dimethyl disulfide on stainless-steel [12] and methyl thiolate on copper. [113]

1.3 Reactive molecular dynamics simulations

1.3.1 Introduction

Early work studying films formation used macroscale tools to measure friction and wear, then analyzed the composition of the resulting films with post-test characterization techniques such as X-ray photoelectron spectroscopy. Such studies revealed that the friction and/or wear reduction as well as film composition were dependent on the sliding conditions, specifically pressure and temperature, and the chemical structure of the compounds [114, 102, 115, 116, 117]. Other experimental studies have shown that there are differences between the compositions of films formed during sliding and those of thermo-oxidative films [118, 119, 120]. Experimental studies can directly measure reaction rates and observe the mechanochemical effect but they do not enable direct observation of reaction pathways. Particularly for tribological processes, identifying reaction mechanisms is challenging because the reactions happen between two surfaces in relative motion. Therefore, computational methods that provide an atomistic view of the dynamics of a chemical system can be beneficial for studying reactions.

Density Functional Theory (DFT) studies have observed the effect of the external force on reactions, [113, 121] but, because of the computationally expensive methods of DFT, it can not be used to investigate the initiation of the process of film formation over a period of time even as short as a few nanoseconds.

Hence, there is a need for a method that both provides an atomistic view and is reasonably large (in number of molecules and the time scale). Such conditions are satisfied by molecular dynamics (MD) simulation. MD simulations have been used in addition to experiments to study film formation on solid surfaces. [12, 122, 123, 124, 125, 126] These studies have used classical MD where the evolution of a system is tracked through time by solving Newtonian equations of motion for all of the atoms simultaneously. However, in classical MD, the formation and breaking of chemical bonds is not considered. Bond forming/breaking is specifically important when studying a chemical reaction in the context of the Bell model since parameters relating to

chemical bonds (e.g., bond energy and compliance) are of interest. For such studies "*reactive*" MD is used. Reactive MD simulations use a reactive empirical model (forcefield), that governs the interactions between atoms and can capture bond formation and breaking.

1.3.2 Reactive forcefields

One of the most commonly used reactive forcefields is ReaxFF. [127] ReaxFF is a bond order-based forcefield that includes covalent chemical bonds, atomic coordination and bond conjugation, van der Waals and Coulomb interactions, and more. Including both short range and long range interactions and a smooth transition between the two makes ReaxFF a useful tool to study chemical reactions. ReaxFF has been widely used to study tribochemical reactions such as sliding SiO_2 surfaces, [128] silica and water on Cu, [129] formation of carbon-based tribofilms, [130] phosphate esters and iron oxide, [131, 132] MoS_2 [133] and many more. For sulfur-containing additives, ReaxFF has been used to study the reaction of thiol molecules with surfaces including gold [134, 135, 136] and copper [137]. Additionally, for MoS_2, ReaxFF has been used for the formation of MoS_2, [138, 139, 140, 141] the active sites of MoS_2 edges, [142] creation of vacancy sites, [133, 143], the distribution and dynamics of defects, [144] and friction properties. [145]

ReaxFF is an element-specific forcefield, meaning that the empirical parameters are fit, or trained, specifically for a limited number of elements for a certain physical-chemical system. The benefit of this approach is that ReaxFF can reproduce accurate results for that system. The disadvantage is that ReaxFF is not available for every element of the periodic table and needs to be optimized for specific chemical systems and materials of interest. The process of optimizing a parameter set for a material or chemical system is called ReaxFF parameterization. In this process, the data from first principle calculations such as DFT, or experiments, is used to optimize a parameter set. The parameter set is then evaluated in several ways, including calculating correct energy barriers, physical properties, etc. to confirm its accuracy. The forcefield can then be used in reactive MD to study chemical reactions.

1.4 Dissertation outline

Studying tribochemical reactions and understanding how lubricant additives provide friction reduction and wear protection, as well as the mechanisms by which tribofilms form, is the key to selecting or developing new additives for lubricated mechanical systems. The observation of such reactions is experimentally challenging since the reactions happen between moving surfaces, so atomistic simulations of the reactions can provide mechanistic insight. DFT calculations are atomic-scale, but are only capable of studying small systems (maybe a few molecules on a small surface). However, DFT can be used to parameterize or validate an empirical forcefield for reactive MD simulations. Reactive MD simulations capture larger length scales than DFT and enable analysis of reactions that happen between two surfaces that cannot be investigated experimentally. This is the approach used here to study tribochemical reactions, reaction pathways leading to and mechanisms of film formation, and kinetics of reactions, as well as the effect of mechanical force. We specifically focus on two sulfur-containing materials that are commonly used in industry either as a lubricant additive or a solid lubricant namely, di-*tert*-butyl disulfide and Ni-doped MoS_2.

Di-*tert*-butyl disulfide is a sulfur-containing EP additive that is commonly used in applied interfacial systems and is well-studied experimentally. [146] For the case of the di-*tert*-butyl disulfide on iron surface, a reaction pathway has been suggested [46] but, due to experimental limitations that are present at tribological interfaces, is not completely understood. In chapter 2, we study this reaction by developing a simulation protocol to mimic the conditions of film formation. We use DFT calculations to validate the parameter set developed for interactions of Fe/S/C/H/O [147] by comparing both bond energies and bond lengths. Then, we identify the reaction pathway that leads to film formation. We determine the rate-limiting step of this reaction and use that to understand the conditions at which the reaction initiates.

It has been shown that shear force can accelerate the rate of film formation. In chapter 3, we study a model of sliding surfaces at a range of temperatures subject to contact pressure. We then calculate the yield of film formation reaction and use it in the context of the Bell model to measure reaction activation energy with and without the presence of mechanical activation.

In chapter 4, we investigate the reaction pathways between di-*tert*-butyl disulfide and ferrous surfaces in a more realistic environment. While lubricants include additives, most of the formula-

tion consists of base oil. Additionally, although tribological surface are subject to constant wear, which exposes pure iron to the lubricants and additives, it is important to model the tribological surface that contains an oxide layer. To address these, we introduce a base oil, namely dodecane, and an iron-oxide surface to our simulation. We then investigate the reaction pathways and analyze the effect of mechanical activation at different contact pressures. Finally, we study the effects of temperature and pressure on reaction kinetics and discuss the mechanochemical activation in the context of the Bell model.

For the case of Ni-doped MoS_2, studies have shown that, under conditions such as low temperature and in the absence of oxygen, the doped material exhibits better tribological performance than undoped MoS_2. Since there is no available ReaxFF parameter set that accurately predicts the interactions between Mo/S/Ni atoms, in chapter 5, we optimize a parameter set that can successfully reproduce the physical properties of Ni-doped MoS_2. We use equations of states for volume change with respect to lattice vectors, bond energy and bond lengths within the Ni-doped MoS_2 unit cell, vacancy-driven structural changes, and the effect of model size on total energy of the model to validate the developed forcefield. Then, we will demonstrate the applicability and accuracy of the force field by carrying out MD simulations to computationally synthesize crystallized Ni-doped MoS_2 by deposition and annealing.

Chapter 2

Reactive Molecular Dynamics Simulations of Thermal Film Growth from Di-*tert*-butyl Disulfide on an Fe(100) surface

K. Mohammadtabar et al. "Reactive molecular dynamics simulations of thermal film growth from di-*tert*-butyl disulfide on an Fe(100) surface". In: *Langmuir* 34 (2018), pp. 15681–15688

Introduction

Iron sulfide films are used for a variety of applications, including in solar energy, water treatment, corrosion and tribology [97]. In the field of tribology, sulfur-containing molecules are used as additives in lubricant formulations, where they react, typically with steel, during operation to form protective films [83]. However, the mechanisms by which these important films form are poorly understood because they arise within a sliding contact that cannot be directly probed experimentally. It has been proposed that such films form when the additive molecules thermally decompose as the temperature increases (on the order of ∼1000 K) in sliding interfaces [148]. More recent studies confirmed that shear is necessary to drive the formation of protective films of some sulfur-containing additives [103] and that reaction kinetics are different for thermal *vs.* shear-driven films [149]. In practice, it is likely that both thermal and shear effects contribute to film formation in sliding interfaces. Here, we explore the reactions leading to the formation of a thermal film, with the overall goal of both understanding the thermal film growth on its own as well as for later using this information to contrast the thermal reaction pathway with that driven by shear. We specifically focus on sulfidic films grown on iron, where iron is used as opposed to the more application-relevant steel because the composition and surface structure of iron are better defined.

Early work studying films from sulfur and iron used macroscale tools to measure friction and wear of organic disufides in oil and then analyzed the composition of the resulting films with post-test characterization such as X-ray photoelectron spectroscopy. Such studies revealed that the friction and/or wear reduction as well as film composition were dependent on the sliding conditions, specifically pressure and temperature, and the chemical structure of the sulfur compounds [114, 102, 115, 116, 117]. More recent studies applied additional surface characterization techniques, such as X-ray absorption near edge structure and atomic force microscopy, and revealed differences between the composition of films formed during sliding and that of thermo-oxidative films [118, 119, 120]. The challenge with extracting information about reaction pathways from the above studies is the complexity of the system, which contains not only the sulfur compound and iron, but also base oil and sometimes other additives. As an alternative, it has been shown that liquid phase lubrication in boundary conditions can be simulated by gaseous species having the same chemical function as the lubricant additive, which provides a means of isolating the reactions of interest [150]. This approach was implemented in experiments with only sulfide molecules (i.e., no oil) on iron foils in vacuum or ultra-high vacuum where film growth rates were obtained using a microbalance, and the composition of the film was characterized using various techniques. Such studies explored the reaction rates and film composition of dimethyl disulfide [151, 148], carbon disulfide [152], and diethyl disulfide [148, 97] on iron. These studies showed that the reaction rate varied with temperature and pressure, and analyses suggested the trends could be explained by a two-stage film formation process where

the reaction initially slows due to the formation of a saturated sulfur layer, but then resumes at higher temperatures as sulfur diffuses into the substrate.

Experimental studies have been complemented by molecular dynamics (MD) simulations, mostly focused on self-assembled monolayers. Previous simulation work dealing with alkanethiols has been primarily carried out on ideal gold or copper surfaces [122, 123, 124, 12]. There are, however, select simulation studies with sulfur-containing molecules and iron surfaces, both investigating corrosion inhibitors on Fe(110). Specifically, simulations were used to explore the adsorption behavior of three thiazole derivatives in sulfuric acid solution [125] and the packing of a self-assembled 2-mercapto-5-methyl-1,3,4-thiadiazole film [126]. Both of these studies used classical MD with the non-reactive COMPASS force field [153].

Although classical MD can provide insight into the behavior of sulfur-based films, connectivity between atoms is predefined in such simulations, so they cannot capture the formation of films through covalent bonding with a surface. The most accurate way to model the formation and breaking of covalent bonds is using first principles quantum calculations. However, this approach is often too computationally intensive to model the full dynamic evolution of a system. The alternative is a reactive potential, which uses a bond order to implicitly describe chemical bonding [154]. Reactive potentials have been used to model hydrocarbon film growth via deposition of ethylene and acetylene on diamond [155, 156, 157] and acetylene on Ag(111) [158]. One of the most commonly used reactive potentials, and the one used in this study because of the availability of parameters for the atoms in our system, is ReaxFF [127].

ReaxFF parameters have been developed to model the reaction of thiol molecules with surfaces including gold [134, 135, 136] and copper [137]. ReaxFF has also been used to model Fischer-Tropsch synthesis, with parameters developed to describe the interactions of iron or iron carbide surfaces with hydrogen and carbon monoxide [159, 160, 161]. One ReaxFF parameter set has also been developed that includes both sulfur and iron [147], albeit not specifically for reactions between organic sulfur compounds and iron. Although the parameters were originally developed to model pyrite (FeS_2), here we demonstrate that it can also capture the adsorption of di-*tert*-butyl disulfide molecules and radicals derived from them on iron surfaces.

As summarized above, experimental techniques have been used to investigate the reaction rates and composition of films grown on iron with simple sulfur-containing molecules in gas-phase. However, such experiments are limited to model molecules, i.e., not actual additives, and do not directly provide information about reaction pathways at the atomic scale. Simulations are ideally suited to address this limitation, but, typically, they are based on an assumed surface film morphology and coverage. This assumption has been made because standard, non-reactive interaction potentials are unable to reproduce the chemical processes of film formation, while the times necessary to treat the entire film formation using the much more time-consuming reactive potentials may exceed the available computational capabilities. While reactive simulations have begun to be utilized to model film growth, none yet have been applied to study the interactions of sulfur-containing molecules on iron.

In this work, to address the gap identified above, we explore the thermal film formation process of di-*tert*-butyl disulfide on iron using reactive MD. Di-*tert*-butyl disulfide is an extreme-pressure additive that is commonly used in applied interfacial systems and is well-studied experimentally [146]. The applicability of the reactive potential for this model system is justified by comparison of adsorption energies and distances to *ab-initio* calculations. Then, reactive MD simulations of di-*tert*-butyl disulfide on an Fe(100) surface are run at temperatures representative of flash temperatures expected in sliding contacts [148]. We initially model a single di-*tert*-butyl disulfide molecule on the iron surface to characterize the reaction pathway, including decomposition and chemisorption of the molecule. The rate limiting step in this process is then identified using simulations where the temperature is ramped up in a step-wise manner. Next, the initial stages of film growth are explicitly modeled. While we omit a base oil solvent for the sake of simplicity, we mimic the iterative nature of such film formation by introducing the molecules in several "waves", so that each group of molecules has sufficient time to undergo the necessary reactions to chemisorb to the surface. This approach represents the next step towards modeling dynamic thermal film growth with real, application-relevant molecules using a reactive potential. It is applied here to describe the film formed with di-*tert*-butyl disulfide interacting with iron, but could be applied subsequently to explore the growth of other films on a variety of surfaces.

2.1 method

2.1.1 Density Functional Theory

Spin-polarized density functional theory (DFT) calculations were performed using the Vienna Ab-Initio Simulation Package (VASP) [162, 163, 164, 165, 166, 167]. To describe the interaction between the core and the valence electrons, the projector augmented wave (PAW) [168] method was applied. Van der Waals (vdW) interactions were considered in the calculations via the optimized Becke86 [169] van der Waals (optB86b-vdW) [170, 171] exchange-correlation functional.

The calculation parameters were converged with respect to the total energy within 1 meV. For relaxations, a tight convergence criterion of 10^{-5}eV on the total energy in the self-consistency cycle was used, while for static calculations a value of 10^{-6}eV was applied. In both cases, a cutoff energy of 600 eV was selected for the plane-wave basis set. The k-space integrations were performed using a $2 \times 2 \times 1$ Monkhorst-Pack mesh [172, 173], static calculations employed the tetrahedron method with Blöchl corrections, and relaxations featured Gaussian smearing with a width of 0.05eV. A conjugate gradient algorithm was used to carry out the relaxations, during which the atomic nuclei were displaced while keeping the shape and volume of the cell constant until all forces were smaller than 0.1eV/nm.

To model adsorption under the DFT framework, a supercell was constructed consisting of an iron surface and either a di-*tert*-butyl disulfide molecule or a *tert*-butyl thiyl radical derived from it. The geometry of the molecule was optimized by performing a relaxation of the isolated molecule in a cubic box of 1.2 nm side length, keeping the relaxation parameters consistent with the rest of the calculations. For the iron surface, two adsorption surfaces, Fe(110) and Fe(100), were considered in this study. To model these surfaces, orthogonal (4×6) and (4×4) surface slabs of four atomic layers of bcc Fe were constructed using a lattice constant of 0.287 nm. The resulting slab surface areas of 1.148×1.218 nm and 1.148×1.118 nm reduced the effect of the interaction between the adsorbed molecule and its mirror image on the total energy to less than 1 meV/atom. To avoid slab–slab interactions, a vacuum space of 2.1 nm was introduced to the supercell. Dipole corrections were applied to compensate for the artificial electrostatic potential introduced by the periodic boundary conditions in the supercell approximation. The resulting slabs were relaxed to obtain the initial surface geometries used in the adsorption calculations. During these relaxations, the atoms of the lowest layer were kept fixed at the bulk-like positions, while the rest of the atoms were allowed to move in all directions. The di-*tert*-butyl disulfide molecule or *tert*-butyl thiyl radical was placed on top of the surface, followed by a relaxation. For each relaxed system, a static calculation with higher accuracy was carried out to determine the total energy. The relaxed structures on the (100) surface are shown in Figure 2.1.

2.1.2 Molecular Dynamics Simulations

The MD model consisted of di-*tert*-butyl disulfide molecules interacting with bcc iron. Initial atomic configurations were created in Virtual Nano Lab (VNL) [174], with di-*tert*-butyl disulfide atom coordinates downloaded from Pubchem [175]. Minimization and dynamics simulations were performed with the LAMMPS [176] simulation package. All atomic interactions were modeled using ReaxFF [127] with a parameter set from Shin *et al.* [147]. Visual analysis of the simulations was done using the OVITO [177] visualization package.

The lateral boundaries of the simulation box were periodic, while in the direction normal to the surface they were kept fixed at a height that varied depending on the position of atoms in the system. In dynamics simulations, the time step was 0.25 fs. During these simulations, the three bottom layers of iron atoms were fixed in space, the two central layers of iron were temperature controlled using a Langevin thermostat with a damping factor of 0.025 ps, and Newtonian dynamics were applied to the top three layers of iron as well as the di-*tert*-butyl disulfide molecules. Because of the system size and the small expected temperature gradients, it was not deemed necessary to implement an electron-phonon coupling scheme to better reproduce the thermal conductivity of iron [178].

Three types of reactive simulations were performed to: (i) calculate the adsorption energy and compare it to DFT results; (ii) characterize the reaction pathway and identify the rate limiting step in that reaction; and (iii) model the growth of a thermal film by cyclic addition of di-*tert*-butyl disulfide molecules.

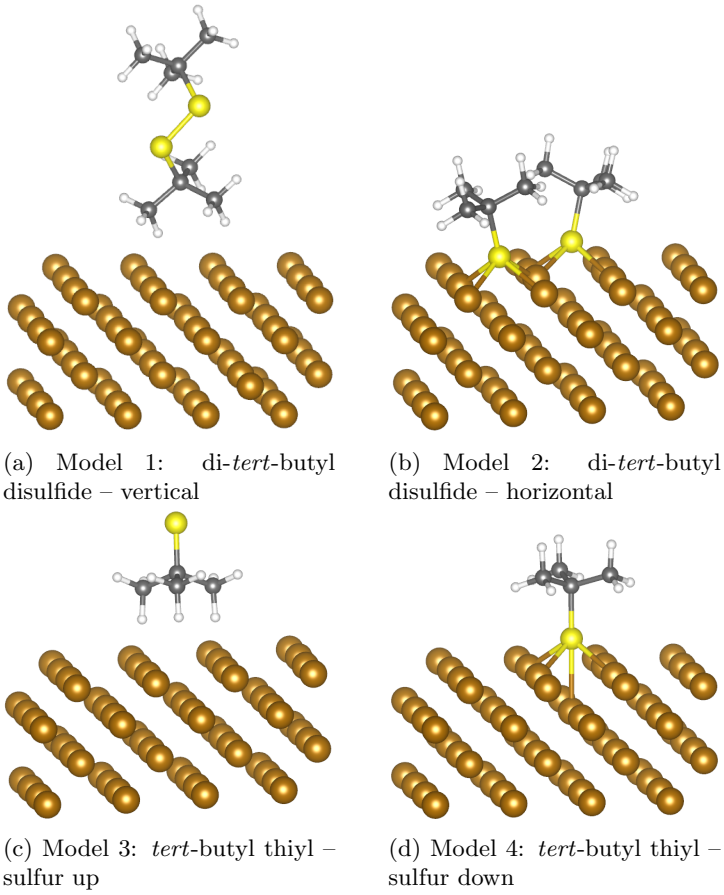

(a) Model 1: di-*tert*-butyl disulfide – vertical

(b) Model 2: di-*tert*-butyl disulfide – horizontal

(c) Model 3: *tert*-butyl thiyl – sulfur up

(d) Model 4: *tert*-butyl thiyl – sulfur down

Figure 2.1: Equilibrium geometries from DFT for the four adsorption configurations on an Fe(100) surface. Fe atoms are brown, S yellow, C gray, and H white. This figure was created by Pedro O. Bedolla at the "Excellence Centre of Tribology" (AC2T research GmbH)

Adsorption Energy Calculation

To ensure that the ReaxFF parameter set used here is applicable to the system being modeled, we first compared adsorption energies and distances to those calculated from DFT. The atom positions from the model systems in the DFT calculations (Figure 2.1) were imported into LAMMPS. This included a di-*tert*-butyl disulfide in two different orientations and a *tert*-butyl thiyl radical in two different orientations, on both the (100) and (110) surfaces of iron. In both cases, the model dimensions were the same as those in the DFT calculations. As discussed later, only the (100) surface was used in subsequent dynamics simulations, but both were evaluated here to better test the potential. Systems containing (a) only the molecule/radical, (b) only the iron slab, and (c) the molecule/radical on the iron slab were constructed. Each system was minimized with ReaxFF using the conjugate gradient algorithm.

Reaction Pathway Characterization

For the reaction pathway simulations, 18 di-*tert*-butyl disulfide molecules with random orientations were placed approximately 0.5 nm above the Fe(100) slab. The slab consisted of 1152 atoms and was 3.44×3.44×1.14 nm in the x, y and z directions, respectively (see upper left inset to Figure 2.2). The model was energy minimized, then dynamics was run, first at 300 K for 0.2 ns, and then ramped up to 900 K over 100 ps. This high temperature was chosen both to accelerate the chemical reactions as well as to be consistent with the temperature range expected for a thermal film that occurs in a sliding interface [148]. The trajectory and bonding state of individual atoms were analyzed to characterize the reaction pathway [15, 29]. Then, to isolate the rate limiting step, the simulation was repeated, but with the temperature ramped up from 300 to 900 K at 100 K increments, with the system held at each temperature for 150 ps. Throughout these simulations, the bond order of each atom was calculated by the ReaxFF potential and recorded. A Python script was written to count the number of bonds between different atom

types, where a bond order of 0.3 or more was considered to be a covalent bond.

Film Growth Protocol

The initial model described above was also used as the starting point of the thermal film growth simulations. One cycle of the process is shown in Figure 2.2. After the addition of the di-*tert*-butyl disulfide molecules 0.2 nm above the Fe(100) surface, the simulation was run at 300 K for 275 ps. The temperature was then increased linearly to 900 K over 100 ps and held at the final temperature for 245 ps. During the temperature ramp and the constant high temperature simulation, some molecule fragments detached from the surface. To limit how far the atoms in these fragments could travel, a repulsive wall was placed above the surface [158]. At the end of the high-temperature equilibration, any molecules or radicals not bonded to the surface were removed from the model. This was done to mimic the diffusion of molecules or radicals into a much larger reservoir of lubricant, as would be the case in a real lubricated contact. Then, the system was cooled down linearly to 300 K over 100 ps. These steps (1–1 through 1–4 in Figure 2.2) represent the first cycle of the film growth process. The next cycle began by adding a second set of 18 di-*tert*-butyl disulfide molecules 0.9 nm above the surface, then the process started again at step 2–1. The procedure described above for the second cycle was carried out three times, for a total of four cycles of thermal film growth. While we do not explicitly model base oil solvent for simplicity, the approach described above approximates the iterative nature of film formation in a lubricated interface by introducing the molecules in several "waves", so that each group of molecules has sufficient time to undergo the necessary reactions to chemisorb to the surface.

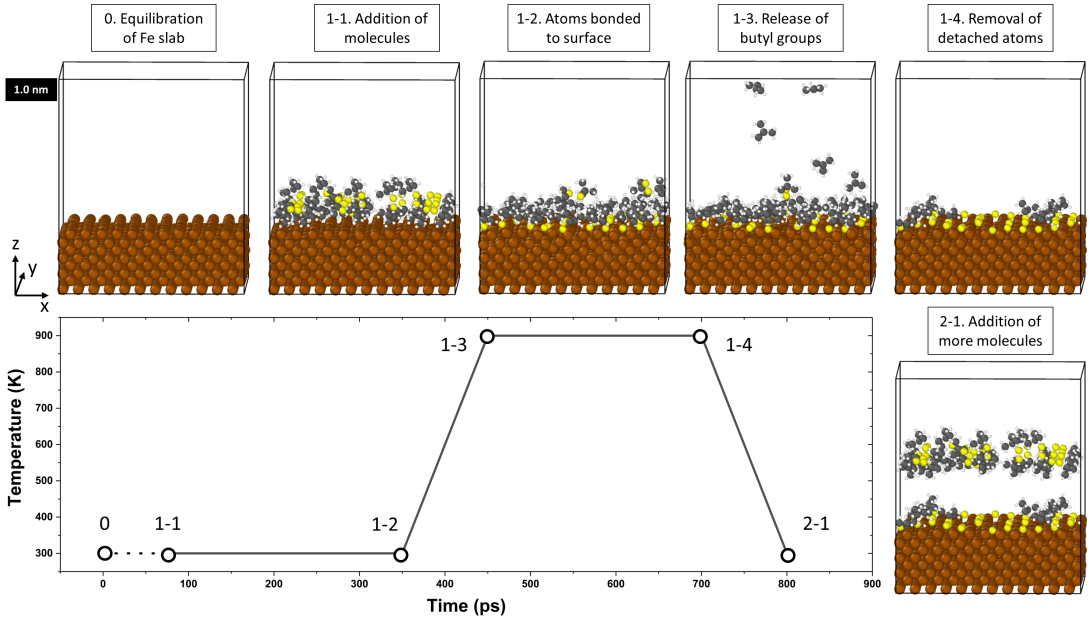

Figure 2.2: Simulation protocol for iteratively growing a thermal film of di-*tert*-butyl disulfide on an iron surface. The insets show perspective view snapshots of the simulation at points corresponding to the numbers in the plot of temperature vs. time, where labels indicate cycle–stage, e.g., 1–2 corresponds to the second stage of the first cycle. Sphere colors are: brown – iron, yellow – sulfur, gray – carbon and white – hydrogen.

2.2 Results and Discussion

2.2.1 Validation of the Empirical Model

MD simulations were performed with a ReaxFF parameter set that includes both sulfur and iron [147], but was not developed specifically for the model system we are studying here. Therefore, we first confirmed the applicability of this parameter set to modeling the interactions of di-*tert*-butyl disulfide and iron by comparing adsorption energies obtained from the force field to those calculated using DFT. In both the ReaxFF and DFT calculations, the energy of the

molecule/radical, iron slab, and molecule/radical adsorbed on the slab were used to obtain the adsorption energy according to the equation

$$E_{\text{ads}} = E_{\text{tot}}^{\text{mol+Fe}} - (E_{\text{tot}}^{\text{mol}} + E_{\text{tot}}^{\text{Fe}}), \tag{2.1}$$

where $E_{\text{tot}}^{\text{mol+Fe}}$ is the total energy of the products adsorbed on the Fe slab at the equilibrium distance, $E_{\text{tot}}^{\text{Fe}}$ is the total energy of the clean Fe slab, and $E_{\text{tot}}^{\text{mol}}$ is the total energy of the isolated gas-phase disulfide molecule or thiyl radical.

The results are shown in Tables 2.1 and 2.2 for the (110) and (100) surfaces, respectively, where the model numbers refer to the configurations shown in Figure 2.1. The adsorption energies obtained from ReaxFF are comparable to those calculated from DFT in most cases. The agreement is particularly good for the Fe(100) surface, for which the difference between DFT and ReaxFF energies is less than 1 eV for all model configurations. The equilibrium distance is defined as the perpendicular distance between the two closest atoms, one belonging to the slab and the other to the molecule or radical. All equilibrium distances are in good agreement, with a maximum difference between DFT and ReaxFF of 0.02 nm. Based on the above analysis, we used the (100) surface for all subsequent MD simulations.

System	Equilibrium distance (nm)		Adsorption energy (eV)	
	DFT	ReaxFF	DFT	ReaxFF
Model 1	0.22	0.20	-0.40	-0.80
Model 2	0.15	0.17	-5.21	-3.93
Model 3	0.20	0.18	0.11	-0.66
Model 4	0.15	0.16	-4.34	-3.26

Table 2.1: Comparison of equilibrium distances and adsorption geometries calculated with DFT and ReaxFF for the systems with an Fe(110) surface

System	Equilibrium distance (nm)		Adsorption energy (eV)	
	DFT	ReaxFF	DFT	ReaxFF
Model 1	0.19	0.18	-0.39	-0.94
Model 2	0.13	0.11	-5.75	-6.60
Model 3	0.18	0.18	-0.72	-0.56
Model 4	0.12	0.10	-4.48	-4.23

Table 2.2: Comparison of equilibrium distances and adsorption geometries calculated with DFT and ReaxFF for the systems with an Fe(100) surface. The values obtained from DFT calculations in this table (Table 2.1 and 2.2) were acquired by Pedro O. Bedolla at the "Excellence Centre of Tribology" (AC2T research GmbH)

2.2.2 Reaction Pathway for Iron Sulfide Formation

ReaxFF simulations were initially run at 300 K for 0.2 ns and then ramped up to 900 K to accelerate the chemical reactions. The movement and bonding of individual molecules was tracked to analyze the reaction pathway. A representative case is shown in Figure 2.3. We observe that the sulfur–sulfur (S–S) bond breaks soon after the molecule approaches the surface. Note that this bond does not break if the molecule is far from the surface, indicating that interactions with the iron caused a weakening of the S–S bond. This is followed by the formation of covalent bonds between sulfur and iron. Finally, the sulfur–carbon (S–C) bond breaks, and a *tert*-butyl group is released. This reaction pathway was observed for multiple initial orientations of the di-*tert*-butyl disulfide relative to the surface. Further, a second set of simulations was run with a time step of 0.1 fs, and the same reaction pathway was observed. This general reaction path – in which the S–S bond breaks, the sulfur atoms bond with the iron surface, and two *tert*-butyl radicals are released – is consistent with what has been previously proposed for dimethyl and diethyl disulfide on iron based on experimental measurements [148].

Three key steps can be identified in the reaction described above: breaking of the S–S bond, formation of the iron–sulfur (Fe–S) bond, and release of a *tert*-butyl group via breaking of the

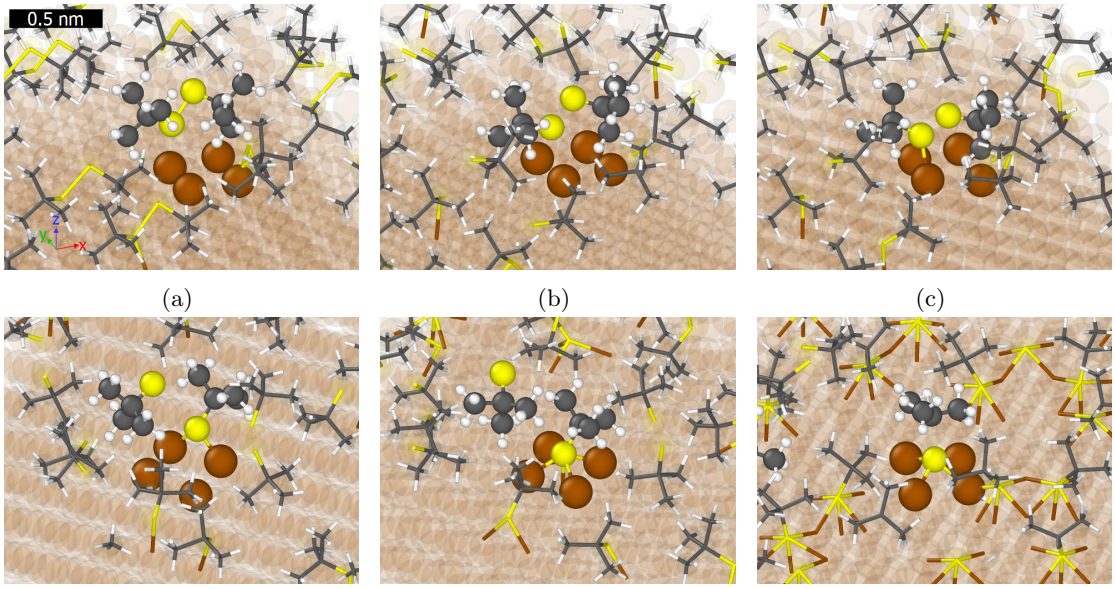

Figure 2.3: Snapshots from the simulation illustrating the reaction pathway for a representative di-*tert*-butyl disulfide. To highlight the atoms of interest, iron atoms are shown partially transparent and all other atoms not involved in the reaction are shown in stick representation. Images (a) through (e) correspond to the 300 K stage of the simulation, and (f) was taken from the simulation after the temperature increase to 900 K. The snapshots illustrate the reaction pathway consisting of (a) a di-*tert*-butyl disulfide molecule approaching the surface, (b) breaking of the sulfur–sulfur bond, (c)–(e) formation of sulfur–iron bonds, and (f) breaking of the carbon–sulfur bond and release of a *tert*-butyl group, where only one of the two sulfur atoms that chemisorbed from this di-*tert*-butyl disulfide molecule is highlighted.
The stick/sphere colors are the same as in Figure 2.2.

S–C bond. Previous work has shown that the S–S bond in disulfides is weak (bond dissociation energies of ∼65 kcal/mol for dialkyldisulfides and ∼50 kcal/mol for diaryldisulfides) compared to the S–C bond (∼73 kcal/mol in dimethylsulfide and ∼77 kcal/mol in diethylsulfide) [179]. This indicates that the S–S bond should break at lower temperatures than the S–C bond, so the release of the *tert*-butyl group is likely to be the rate limiting step in the reaction.

To confirm that our simulation reproduces this expectation, we performed simulations in which the temperature was ramped up from 300 to 900 K at 100 K increments, as illustrated in Figure 2.4. Figure 2.4a shows that the S–S bonds start breaking at room temperature and are broken in all di-*tert*-butyl disulfide molecules before the temperature reaches 500 K. The formation of Fe–S bonds occurs somewhat more slowly (Figure 2.4b), with almost all of the S atoms in the system bonded with the Fe by the time the temperature reaches 800 K. However, the slowest reaction is clearly the breaking of the S–C bond, which, as shown in Figure 2.4c, does not start happening until the temperature reaches 700 K, and only ∼ 20% of the *tert*-butyl groups have been released by the end of the temperature plateau at 800 K. Increasing the temperature to 900 K finally pushes the fraction of detached *tert*-butyl groups beyond 70%. The observation from our simulations that organic moieties are not easily released from the surface is consistent with the presence of carbon in experimental thermal films [148]. In general, a comparison of the temperature at which each reaction occurs indicates that, as expected, the release of the *tert*-butyl group through breaking of the S–C bond is the rate liming step of the reaction of di-*tert*-butyl disulfide with an iron surface.

2.2.3 Modeling Thermal Film Growth

The film growth protocol illustrated in Figure 2.2 was run four times. Throughout the simulation, the sulfur coverage was calculated from the number of sulfur atoms covalently bonded to the iron surface divided by the total number of available bonding sites (in this case 144). The coverage and actual temperature are shown in Figure 2.5 along with top view snapshots of the surface and atoms bonded to the surface at the end of each cycle. During the 300 K stage of the first cycle, we

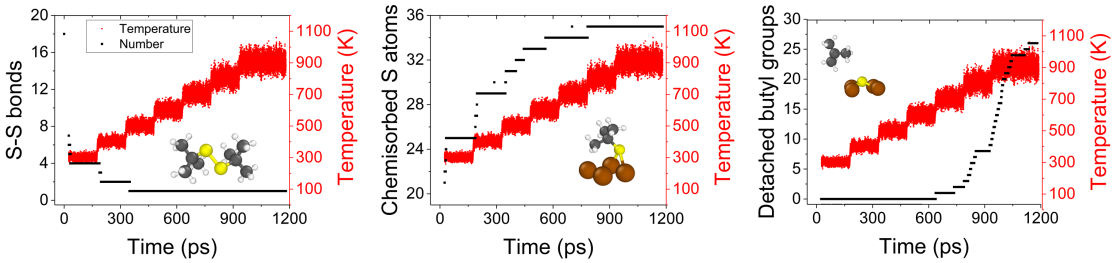

(a) (b) (c)

Figure 2.4: Temperature dependence of the three key steps in the reaction: (a) breaking of the S–S bond in the di-*tert*-butyl disulfide, quantified by the number of S–S bonds; (b) chemical bonding with the surface, quantified by the number of S atoms bonded to the surface; and (c) release of *tert*-butyl groups, quantified by the number of detached *tert*-butyl groups in the simulation.

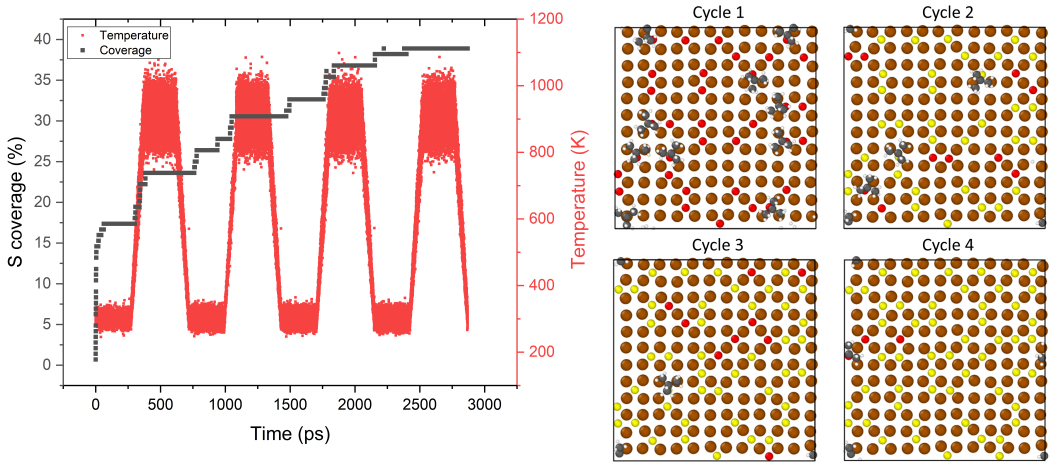

(a) (b)

Figure 2.5: (a) Sulfur coverage on the iron surface and model temperature during four cycles of the film growth protocol. (b) Top view snapshots of the model after each of the four cycles. Only the topmost Fe atoms and S atoms or *tert*-butyl thiyl radicals bonded to the surface are shown. S atoms that bonded to the surface during a given cycle are shown in red while those that bonded to the surface in a previous cycle are shown in yellow.

observe that the sulfur coverage increases rapidly, up to 18%. There are a few additional bonds formed during the temperature ramp, and then the coverage remains constant during most of the 900 K stage of the first cycle. During this time, S–C bonds break, enabling *tert*-butyl groups to leave the surface; these radicals are subsequently removed from the simulation. The reaction pathway is the same as that described above based on simulations of single molecules on iron. Further, we observe that, in most cases, S atoms from a given di-*tert*-butyl disulfide molecule bond with Fe at adjacent sites on the surface. At the end of the first cycle, the sulfur coverage is at 24%.

The second and third cycles exhibit similar behavior as the first, with sulfur chemisorption occurring during the 300 K phase and then *tert*-butyl removal during the 900 K phase. However, the rate of coverage increase with time is slower each cycle due to the decreasing availability of reaction sites. An analysis of Figure 2.5b suggests that film growth after the first cycle occurs by new sulfur atoms preferentially adsorbing to those iron atoms that are least saturated by previously adsorbed sulfur atoms. At the end of the second and third cycles of tribofilm growth, the surface coverage is 31% and 37%, respectively. During the fourth cycle, few additional reactions occurred and the film reached a maximum coverage of 39%. This is likely near the maximum coverage that can be achieved within the nanosecond-scale duration of a reactive MD simulation. Unfortunately, the results cannot be compared directly to experimental observations of Fe–S film

growth over minutes of reaction time [151, 148, 152, 97]. However, the simulations complement experimental approaches since the simulations enable direct observation of individual species involved in reactions with surfaces and their behavior under various conditions, providing information about the initial stages of film formation that is not currently accessible using even highly resolving surface analytical methods.

To evaluate the friction reducing potential of a fully grown Fe–S film, we performed some preliminary simulations of moving a hemispherical Fe(111) tip with a diameter of 1.38 nm over the surface at normal loads ranging from 0.7 to 5.5 nN, equivalent to 0.5 to 3.7 GPa. This was done on a clean Fe(100) surface and on a surface covered with 144 S atoms, which translates into 100% coverage. We analyzed the friction-versus-load behavior, $F(L) = \mu L + F_0$, where F is the friction force, μ the coefficient of friction, L the normal load, and F_0 the load-independent friction at zero load that is generally related to adhesion [180]. The friction coefficient μ was reduced by 50% in the system with the Fe–S film, and the dominating load-independent force F_0 was reduced by more than 85% of the value obtained with the clean Fe(100) surface. This led to an overall reduction of friction force by a factor of approximately six. The results of this preliminary simulation are consistent with experimental observations of the benefits of sulfur on iron surfaces, including more sulfur content leading to lower wear [102] and higher seizure load [148].

2.3 Summary and Conclusions

Films formed by chemical reactions between ferrous surfaces and di-*tert*-butyl disulfide – an important extreme pressure additive, e.g., used in gears – are critical to the efficiency and useful lifetime of mechanical components with lubricated interfaces. Here, we modeled the initial steps of the thermal formation of such a protective film using molecular dynamics simulations with a reactive empirical potential, validated for the most relevant interactions by comparison of adsorption energies to DFT calculations. The empirical model was used to identify the reaction pathway leading to iron sulfide: the S–S bond in the di-*tert*-butyl disulfide breaks, the S atoms bond to the Fe(100) surface, and then *tert*-butyl groups are released. This observation is consistent with pathways for reactions between sulfur-containing molecules and iron previously proposed based on experimental measurements. Next, simulations performed at increased temperatures suggested that the breaking of the S–C bond enabling *tert*-butyl radical release was the rate limiting step of the reaction. With this understanding of the steps associated with surface reactions, we implemented a simulation protocol to mimic the process by which films form in lubricated interfaces where the surfaces are repeatedly exposed to temperature increases due to sliding. Using this approach, the onset of the formation of an iron sulfide film was captured.

Future research efforts specifically focused on di-*tert*-butyl disulfide and ferrous surfaces can build on the foundations established in this work. For example, here we mimicked molecules at the surface being replenished through lubricant flow by manually adding new molecules to the system. However, more complex models can explicitly incorporate base oil molecules and liquid flow to confirm that the reactions we observe here are indeed representative of the precursors of a thermal film in a lubricated interface. Further, in practice, these films form through the combined effects of frictional heating and mechanical stress. Future models can incorporate load and/or shear by introducing an iron counterbody that confines the additive molecules, as demonstrated by the preliminary simulations of frictional sliding described in the previous section. Such an approach can be used to differentiate the effect of temperature from that of shear in driving chemical reactions. Moreover, the thermal film growth simulation approach was demonstrated here with an ideal Fe(100) surface. This choice reflects the assumption that nascent iron surfaces are exposed as surfaces slide relative to one another, but is a simplified approximation of the likely surface composition and structure. The approach demonstrated here can be extended to study the interaction of di-*tert*-butyl disulfide (or other additives) with other iron surfaces or with iron oxide. Lastly, thermal films, both with sulfur-containing molecules and otherwise, are present and important in many different applications. Therefore, the approach demonstrated here can be applied to explore the initial stages of film formation in a variety of scientific and engineering fields.

Chapter 3

Heat-, Load-, and Shear-Driven Reactions of Di-*tert*-butyl Disulfide on Fe(100)

K. Mohammadtabar et al. "Heat-, load-, and shear-driven reactions of di-tert-butyl disulfide on Fe(100)". In: *J. Phys. Chem. C* 123(32) (2019), pp. 19688–19692

3.1 Introduction

The surfaces of moving mechanical components are protected from damage during operation by films that form when lubricant additives are present between the sliding surfaces. Analysis of these protective films has shown that they are composed of elements from both the lubricant additives and the surface material [84, 85, 87, 88, 86]. The implication is that the films are formed through chemical reactions between the additives and surfaces. Some of these films do not form or only form very slowly if the surface is simply immersed in a lubricant with additives under ambient to moderate conditions [181, 182, 183]. Accordingly, the common understanding is that these reactions are driven by factors that arise in the sliding contact. Physical factors in sliding contacts include temperature, load and shear force [184, 185, 186, 110]. First, frictional sliding results in heat generation, which can drive film-forming chemical reactions thermally. Second, normal loads on relatively small contact patches can result in high pressures, which place reactants in closer proximity, thereby facilitating chemical reactions. Lastly, shear forces are always present in sliding interfaces and are believed to contribute to film growth through mechanochemical reactions.

Numerous studies have now shown that shear force can drive chemical reactions on surfaces; for example, film growth from reactions between zinc dithiophosphate and steel, [107, 187, 186, 188] cleavage of oxygen and fluorine from graphene, [27] or dissociation of methyl thiolate from a copper surface [12]. These observations are consistent with a modification of the Arrhenius model in which a force applied along the reaction coordinate lowers the energy barrier for a reaction, thus accelerating chemical reactions. Although this model is typically used to describe the effect of normal force, it has been applied to capture shear-driven reactions [189]. However, the mechanism by which shear accelerates reactions is still a subject of active research. For example, it is not known whether shear simply drives reactions to occur faster through the same pathway as observed thermally, or if shear enables reaction pathways that are not available thermally. There is some evidence of the latter from vapor phase lubrication experiments complemented by reactive molecular dynamics simulations [15, 131], but not specifically related to reactions between lubricant additives and surfaces. Studies of additive-surface interactions have suggested that the first step of film formation is additive decomposition, which leads to generation of radicals that interact and react with the surface [181, 183]. Decomposition is believed to be the first reaction step for thermal- and shear-induced films, which is supported by the observation that both films have similar compositions [85, 183, 86]. Therefore, it is difficult to differentiate or isolate the effects of heat and shear on film formation. Further, it is likely that the relative contribution of these two effects depends on interface conditions, and it has been proposed that film formation is thermally driven under extreme pressure conditions and driven by shear under moderate conditions [110].

Protective films frequently contain sulfur, and this element is incorporated in many surface-active additives that are critical components of common lubricant formulations. The sulfur

reacts with the surfaces, typically steel, during operation to form iron-sulfide-based films [83, 190]. However, the mechanisms through which these films form are still poorly understood, due in part to challenges with experimental investigation of additive-surface interactions. This limitation suggests the use of simulations that can capture reaction pathways at the atomic scale. In a previous study, we used reactive molecular dynamics (MD) simulations to study the thermal contribution to film formation for di-*tert*-butyl disulfide on an Fe(100) surface [1]. The simulations were used to identify the thermally driven reaction pathway as follows: S–S bonds in the di-*tert*-butyl disulfide break, S atoms in *tert*-butyl sulfide bind to the Fe(100) surface, and then S–C bonds break enabling the release of *tert*-butyl groups. These steps are consistent with the reaction pathway previously proposed for sulfur-containing molecules and iron, based on previous experimental measurements [148]. Simulations at various temperatures showed that the rate limiting step was the S–C bond scission and that significant detachment of *tert*-butyl radicals did not occur until the temperature was increased to 700 K or higher. However, film formation from organic disulfides has been observed in sliding contacts at significantly lower system temperatures [191, 151, 192], suggesting that other factors in addition to heat contribute to films observed at sliding contacts.

In practice, film formation from di-*tert*-butyl disulfide on ferrous surfaces is likely driven by a combination of heat, load and shear. However, these effects cannot be isolated experimentally since all of them are occurring simultaneously, hidden from view in a sliding interface. The inability to differentiate the roles of individual contributions to film formation limits efforts to develop optimized lubricant additives or additives with application-specific film formation properties. To address this, here we use simulations to deconvolute the effects of heat, load and shear on chemical reactions between di-*tert*-butyl disulfide and Fe(100). Specifically, reactive MD simulations that capture the formation and breaking of covalent bonds are used to characterize the key steps along the reaction pathway leading to film formation.

3.2 Methods

The initial atomic configurations of di-*tert*-butyl disulfide molecules (Fig. 3.1a) were obtained from PubChem [175]. These molecules were confined between two bcc Fe(100) slabs were created using Virtual NanoLab [174] and Packmol [193]. Energy minimization and molecular dynamics were performed using the open-source MD code LAMMPS [176]. All visualizations were done using OVITO [177]. Post processing and data analysis were performed using scripts written in Python.

Two bcc Fe(100) slabs with dimensions of 3.4×3.4×1 nm were created and positioned in the model with a 2 nm gap between them in the z-direction. The Fe(100) surfaces were model approximations of steel on which the iron oxide layer is worn off during sliding. This simplification also facilitated analysis of reaction pathways, which were same everywhere on the surfaces, in contrast to reactions that occur on irregular surfaces such as amorphous iron oxide where many different pathways can be observed [4, 194]. Then, 54 di-*tert*-butyl disulfide molecules were randomly distributed in the gap. The model fluid consisted only of additive molecules, i.e., no base oil, to limit the size of the simulation and increase the number of additive-surface interactions. A snapshot of the simulation after the initial equilibration is shown in Fig. 3.1b. The boundary conditions were periodic in the directions in the plane of the iron surfaces (x and y) and fixed in the surface-normal direction (z). The atoms in the bottom atomic layer of the lower slab and the top atomic layer of the upper slab were treated as rigid bodies to facilitate imposing the desired kinematics to the system.

Atomic interactions were modeled using the ReaxFF force field [127] with a previously developed parameter set for Fe/S/C/H/O [147]. This parameter set was shown to accurately reproduce adsorption energies calculated using density functional theory (DFT) for di-*tert*-butyl disulfide and its radicals on Fe(100) [1]. The temperature was controlled using a Langevin thermostat with a damping parameter of 25 fs, acting only on the two layers of Fe atoms adjacent to the fixed atoms in both slabs. The di-*tert*-butyl disulfide molecules and the three layers of Fe atoms adjacent to these molecules were integrated in the microcanonical ensemble with a time step of 0.25 fs, and their temperature was controlled indirectly via the thermostat applied to the adjacent atoms.

To isolate the effects of heat, pressure, and shear on reactions between the di-*tert*-butyl disulfide and the iron surfaces, simulations were run in three stages. Following energy minimization, simulations without normal load or shear were run for 2 ns each at constant temperatures of

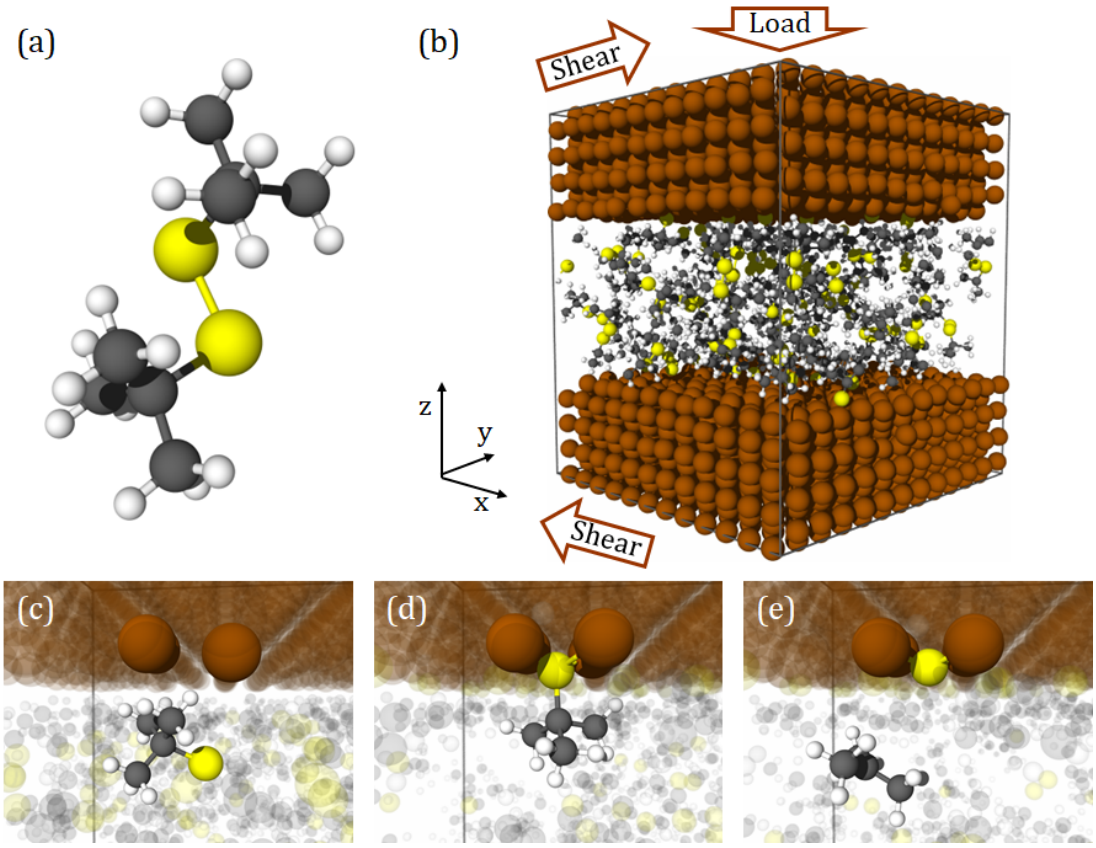

Figure 3.1: Snapshots of (a) the di-*tert*-butyl disulfide molecule and (b) the simulation domain shortly after the initial equilibration. Close-up views of specific steps in the pathway leading to the formation of iron sulfide are shown in (c) to (e), where all atoms except those involved in the reaction are faded out: (c) di-*tert*-butyl disulfide approaches the iron surface; (d) formation of Fe–S bonds by chemisorption of the *tert*-butyl sulfide radical on the iron surface; and (e) breaking of the S–C bond, leading to detachment of a *tert*-butyl radical. Sphere colors represent yellow – S, gray – C, white – H and brown – Fe.

300, 400, 500, 600, and 700 K. After completion of the first stage, a normal load was applied to the atoms in the rigid body of the top wall. The top wall moved in $-z$-direction in response to this load, reaching a final constant pressure of 1 GPa. All five temperature cases were subject to this pressure for another 2 ns. Keeping the pressure at 1 GPa, the top and bottom iron slabs were then moved laterally in opposite directions at speeds of $v_x = \pm 5$ m/s. The component of the kinetic energy in the z-direction was excluded from the temperature calculation during the load stage and the x-direction component was excluded in the load and shear stages. Shear simulations were run at all five temperatures for 2 ns. During all simulations, the positions and bond orders of the atoms were recorded every 1.25 ps. A covalent bond was identified as a bond order of at least 0.3. The three previously identified key steps in the reaction pathway [1] are illustrated in Fig. 3.1c–e. The first step, dissociation of the S-S bond, occurs rapidly at all temperatures as soon as the molecules approach one of the surfaces, and chemisorption occurs immediately after, typically within 1–2 ps. Therefore, we tracked the reaction in terms of the latter two steps: chemisorption of *tert*-butyl sulfide and *tert*-butyl radical release. Chemisorption was calculated as the number of S atoms having at least one S–Fe bond. Radical release was calculated from the difference between the number of S–C bonds at the start of the simulation and that number at each time step as the simulation ran.

3.3 Results and discussion

Figure 3.2 shows the number of chemisorbed S atoms and the number of *tert*-butyl radicals released from the surface during the three stages of the simulation at temperatures between 300 and 700 K. Generally, these results show that both chemisorption (Fe–S bond formation)

and *tert*-butyl release (S–C bond breaking) were accelerated by temperature, load, and shear. Note that the maximum possible number of chemisorbed S atoms and released *tert*-butyl groups was 108, limited by the number of di-*tert*-butyl disulfide molecules in the system. The trends observed during each stage of the simulation are analyzed in more detail below.

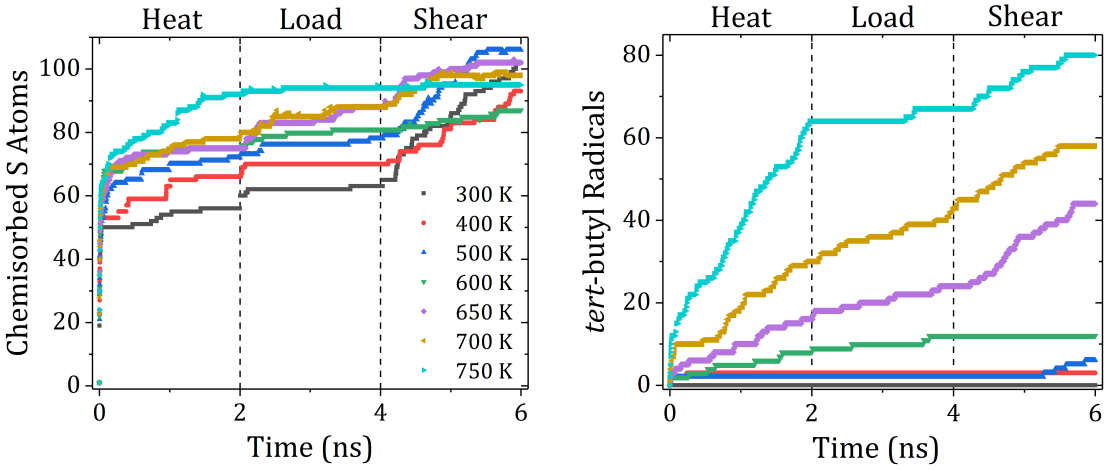

(a) (b)

Figure 3.2: Number of (a) chemisorbed sulfur atoms and (b) *tert*-butyl radicals as functions of time during the heat, load, and shear stages of the simulation at temperatures between 300 and 750 K.

The system was initially subject to heat without load or shear for 2 ns. As shown in Fig. 3.2a, chemisorption occurred rapidly at the onset of the simulation at any temperature due to the availability of reaction sites on the iron surface. During the heat stage, the number of released *tert*-butyl radicals, shown in Fig. 3.2b, was relatively small (<3), except at the higher temperatures ($\geq$600 K), consistent with our previous study of thermal film growth [1]. At the end of the heat stage, both the number of chemisorbed S atoms and released *tert*-butyl radicals increased monotonically with temperature.

Applying a normal load caused a small, sharp increase in chemisorption, as the *tert*-butyl sulfide groups were forced into nearby available reaction sites. However, the change in number of chemisorbed S atoms during the load stage was relatively small, with an increase of between 4 and 10 atoms relative to the end of the heat stage. Also, the number of chemisorbed S atoms was a monotonic function of temperature at the end of the load stage. The number of *tert*-butyl radicals slightly increased during the load stage, indicating that load does not significantly accelerate this reaction step. At the end of the load stage, additional release of *tert*-butyl radicals were only observed at 600 K and higher.

Finally, when shear was applied, the number of chemisorbed S atoms again increased rapidly, as *tert*-butyl sulfide groups were translated along the surface until they reached available reaction sites. The effect of shear was more significant than that of load, with an increase in chemisorption of between 6 and 39 atoms relative to the end of the load stage. This trend was also evident at some temperatures for the detached *tert*-butyl groups, which exhibited a sharp increase at 700 K at the onset of shear, and at 500 K approximately half-way through the shear stage. Therefore, at the end of the shear stage, detachment of *tert*-butyl radicals was observed at temperatures of 500 K and higher. However, the number of chemisorbed S atoms at the end of the shear stage was no longer monotonic with temperature.This is attributed to the presence of *tert*-butyl radicals at higher temperatures, which, in some cases, impeded the motion of *tert*-butyl sulfide groups, hindering their ability to reach available reaction sites on the surface.

Considering chemisorption, the results above show that this reaction is accelerated by heat, load, and shear. We observed that all S atoms chemisorbed at the hollow sites on the Fe(100) surfaces. The binding energy for this process has been reported to be -74.1 kcal/mol from DFT calculations and -87.6 kcal/mol from ReaxFF calculations [147]. This is consistent with the rapid chemisorption observed at the start of simulations at any temperature. Therefore, the limiting factor for chemisorption is the ease with which *tert*-butyl sulfide groups can reach reaction sites on the surface. Heat provides more thermal energy that enables molecules to move to available reaction sites, load drives molecules downward toward nearby reaction sites, and

shear moves molecules laterally on the surface toward sites further from their original position. Lateral movement was quantified in the simulations as the maximum mass diffusivity of the S atoms in the *tert*-butyl sulfide groups. During the heat stage, the maximum diffusivity was calculated to be 1.2 nm^2/ns at 300 K and 26 nm^2/ns at 700 K, so thermal motion enabled translation of the radicals. Load did not affect diffusivity at any temperature. Shear, however, significantly increased molecular movement; for example, at 300 K, the diffusivity increased from 1.2 nm^2/ns during the heat stage to 160 nm^2/ns during the shear stage of the simulation. This is significantly higher than in either of the other two stages, supporting the hypothesis that shear accelerates chemisorption by facilitating movement of molecules to available reaction sites on the surface.

Increasing sulfur coverage on the surface is expected to correspond to lower friction, so the effect of shear to increase chemisorption in our simulations should also correspond to a decrease in friction. To confirm this, the coefficient of friction (CoF) was calculated as the force in the x-direction on the fixed atoms of the upper slab divided by the normal load. The CoF was averaged over the first and last 0.5 ns of the shear stage at 300 K. The CoF decreased from 0.25 to 0.11, confirming the beneficial effect of sulfur coverage and the role of shear to cause an increase in that coverage.

The release of *tert*-butyl radicals through breaking of C–S bonds is accelerated by heat and shear, but via a different mechanism than the chemisorption. A previous study of the decomposition of methyl thiolate species on Cu(100) showed that the energy barrier for reaction was lowered by 40% due to shear [12]. Further, complementary DFT calculations of the decomposition process revealed that the methyl group moved laterally relative to the Cu(100) surface during the reaction; since shear force is in this same direction, the reaction can be accelerated by the mechanical force [12]. The results we observed for di-*tert*-butyl disulfide on Fe(100) may be explained by the same phenomena, where a mechanical force acting along the reaction coordinate lowers energy barriers to accelerate reactions.

The model for mechanochemical processes is written as follows [189]:

$$r_y = A \exp\left(-\frac{\Delta E - \Delta E^*}{k_B T}\right) , \tag{3.1}$$

where r_y is the reaction yield, A is a coefficient, ΔE is the activation energy, ΔE^* is the amount by which the energy barrier is reduced by the mechanical force, k_B is the Boltzmann constant, and T is temperature. Taking the natural logarithm, this can be re-written as [15, 131]:

$$\ln(r_y) = \ln(A) - \left(\frac{\Delta E - \Delta E^*}{k_B T}\right) \tag{3.2}$$

The reaction yield was approximated from our results (Fig. 3.2b) as the number of *tert*-butyl radicals at the end of each stage of the simulation. Then, the energy barrier ($\Delta E - \Delta E^*$) can be estimated as the slope of a linear fit of $\ln(r_y)$ vs. $1/(k_B T)$, as shown in Fig. 3.3a.

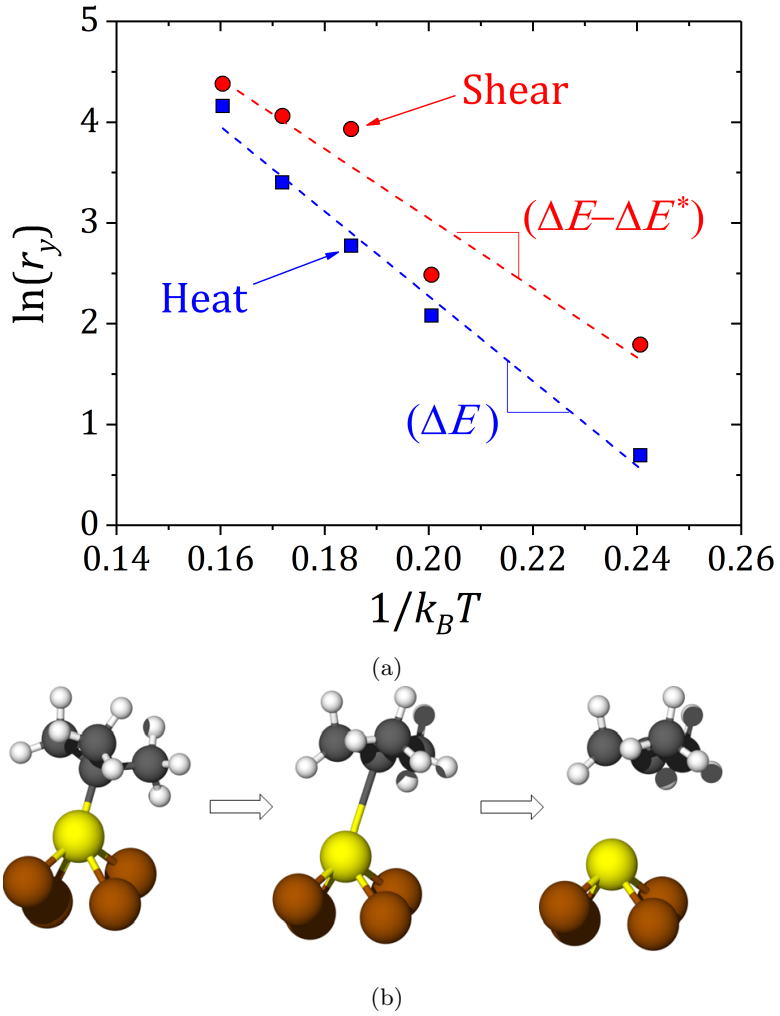

Figure 3.3: (a) Natural log of the reaction yield as a function of inverse temperature for the heat and shear stages of the simulation. The data is fit to Eq. (3.2) such that the fit slope is the reaction energy barrier. When only heat is available to drive the reaction, the energy barrier is ΔE; adding shear decreases that barrier by ΔE^*. (b) Representative snapshots from the simulation showing that S–C dissociation occurs through lateral movement of the C atom relative to the surface, enabling shear to accelerate the reaction.

In the heat stage, there is no mechanical contribution, so $\Delta E^* = 0$. During this stage of the simulations, reactions were observed at 600 K and above. Fitting the data at these temperatures led to a calculated ΔE of 10.1 kcal/mole. In the shear stage, reactions were observed at 500 K and above. These data points were fit to Eq. (3.2) to give a slope of 8.2 kcal/mole, indicating that $\Delta E^* = 1.9$ kcal/mole. These results show that shear can lower the energy barrier for this reaction. As described previously [12], this is possible because the reaction occurs through lateral movement of the C atom relative to the surface, as shown in Fig. 3.3b. Shear force acts on the *tert*-butyl sulfide radical in the same direction and so can accelerate the reaction. Since the radical has no preferred orientation in the xy-plane when bonded to the iron surface, shear in any direction will have the same effect.

Finally, the results show that the relative contributions of heat and shear depend on temperature. Specifically, as shown in Fig. 3.3a, at lower temperatures the reaction yield is much higher with shear than without, but this difference is not observed at higher temperatures. This observation is consistent with the suggestion from previous experimental work that protective film formation is thermally driven under extreme pressure conditions (where friction heating is likely to be significant) and driven by shear under moderate conditions (lower frictional heating) [110].

3.4 Conclusions

In summary, reactive MD simulations of di-*tert*-butyl disulfide confined between Fe(100) surfaces was used to explore the effects of heat, load, and shear on chemical reactions that are the precursors to film formation. Results showed that all three factors accelerated the key steps in the reaction pathway, S chemisorption and *tert*-butyl radical release. Chemisorption was limited only by the ability of *tert*-butyl sulfide radicals to reach available reaction sites on the Fe(100) surface, which was facilitated by thermal energy (heat), downward motion toward near sites (load) and lateral motion to further reaction sites (shear). The *tert*-butyl release step was driven by heat and shear, where shear lowered the energy barrier for reaction mechanically. Results confirmed previous suggestions that film formation reactions may be driven thermally and mechanically, where the role of the mechanical force is significant under moderate conditions where frictional heating will be relatively small.

Chapter 4

Shear-driven Reactions of Organosulfur Compounds on Ferrous Surfaces: A Molecular Dynamics Study

Karen Mohammadtabar et al. "Shear-driven reactions of organosulfur compounds on ferrous surfaces: A molecular dynamics study". In: *Tribology International* 176 (2022), p. 107922

4.1 Introduction

Mechanical stress can couple with chemical reactions at the molecular scale to lower the energy barrier that must be overcome for reactions to occur. Such mechanochemical reactions have several potential advantages, including higher yield and improved selectivity [195, 14, 196]. In addition to driving chemical reactions by lowering the energy barrier, it has been reported that mechanical forces can introduce new reaction pathways that are not accessible thermally. Alternative pathways due to mechanical work have been reported for synthesis of dibenzophenazine [197], ring-opening of trans and cis isomers of a 1,2-disubstituted benzocyclobutene [198, 11], and degradation of polymers [199]. Mechanochemistry is therefore highly relevant for chemical synthesis, for example as applied in ball milling, [195, 14] where mechanical stress drives chemical reactions that create products with desired properties.

Another application where mechanically driven reactions are ubiquitous is lubrication of moving mechanical components in the field of tribology [200]. During operation, tribological systems frequently run in the boundary lubrication regime. Under such conditions, surface-active additives that are added to lubricant formulations, form protective films, called tribofilms, on the contacting surfaces that facilitate relative motion with controlled friction and reduced wear. [103, 201]. While tribochemical reactions are present in nearly all lubricated (and some non-lubricated) mechanical systems, their fundamental mechanisms are not fully understood because they occur between two moving surfaces where direct experimental measurement is challenging. However, understanding these mechanisms has the potential for significant impact, specifically for optimizing tribofilm growth and more generally for enhancing our understanding of the pathways by which mechanical stress can drive chemical reactions.

Film formation occurs through adsorption and chemical reactions between additives and surfaces. These chemical reactions are believed to be driven by the local heating and mechanical stress that are inherent to tribological contacts. The study of these reactions is referred to as tribochemistry [202, 200]. The amount by which reactions leading to tribofilm formation are accelerated by mechanical stress is determined by its effect on the energy barrier for the reaction to proceed. For tribochemical reactions, shear stress due to forces acting parallel to the sliding surfaces is particularly relevant. [203]

Experimentally, the effect of shear to accelerate chemical reactions can be quantified by measuring the increase in reaction rate or yield with increasing stress. Examples of this experimental approach are studies of bond cleavage [25, 26, 27], polymerization, [28, 15, 29] and film formation [30, 204]. Specifically relevant to lubricant additives, recent studies have shown that tribofilm growth rates increase with shear stress for zinc dialkyl dithiophosphate (ZDDP) on steel [105], iron [106], silicon [107], and other non-ferrous surfaces [108], as well as for dimethyl disulfide [109, 110], diethyl disulfide, and dimethyl trisulfide on copper [111]. Such studies consistently show that shear stress increases the reaction yield or enables reactions to proceed at

lower temperatures than observed for purely thermally driven reactions.

Experimental studies of shear-driven reactions have been complemented by simulation-based investigations that provide atomic-scale information about reactions and reaction pathways. First, density functional theory (DFT) calculations have been carried out to identify the pathways of shear-driven reactions, for example, reactions of propanethiolate on gold [205] and methanethiolate on copper [12]. DFT was also used to analyze the effect of shear stress to accelerate the removal of alkoxy species from oxidized iron [206] and the effect of normal stress on molecular dissociation of organophosphorus additives on iron [207].

Reactive molecular dynamics (MD) simulations, i.e., MD simulations based on empirical models that capture chemical reactions, have also been used to study shear-driven reactions. Pathways of reactions between lubricants and surfaces were investigated for water on SiO_2 [208], hexadecane-lubricated diamond sliding against W(100) [209], di-*tert*-butyl disulfide on Fe(100) [1, 2], and phosphate esters and inorganic alkali polyphosphates on iron oxide [29, 210]. Reactive MD simulations have quantified the amount by which a reaction energy barrier is reduced by shear for oligomerization during gas phase lubrication [29], film formation from di-*tert*-butyl disulfide on Fe(100) [1], as well as chemical mechanical polishing of Cu in hydrogen peroxide and glycine [211]. Nudged elastic band calculations with a reactive potential have also been used to show how shear stress can lower energy barriers at the molecular scale [212].

While the goals of experimental work and atomistic simulations are often complementary, there are distinct differences between the material in the models and physical systems. First, in practice, film forming additives are typically used in very low concentrations in a lubricant formulation, and most of the liquid present in an interface is base oil. Previous studies have shown that hydrocarbon-based oil can react chemically with various surfaces to create thin films, even without additive.[213, 214, 215] Simulations of a model base oil, hexadecane, have shown thin film formation as well.[216, 217, 209] However, previous atomistic simulations have not included both base oil and additives to understand their interactions during film formation.

The surface with which additives react also plays an important role in both determining reaction pathways, as well as reaction rate. Most engineering components comprise ferrous materials, which are expected to have a thin oxide layer. However, these oxides can be removed by wear such that the highly reactive metallic iron surface is exposed. [218] It has been observed that the presence of freshly exposed metal surfaces (due to wear) increases the rate of the chemical reactions. [219] This implies that film formation reactions will occur on both iron and iron oxide during operation. For simplicity, many previous simulations have used crystalline iron surfaces [1, 2, 220, 221, 222, 223]. Others modeled iron oxide, either amorphous or crystalline. [190, 224, 225, 4]. However, there has been no comparison of mechanically driven film formation reactions on crystalline iron and iron oxide surfaces.

Previous computational studies have demonstrated the reaction mechanisms for di-*tert*-butyl disulfide on Fe(100), but if or how these mechanisms are relevant to more representative conditions with base oil and a surface oxide is not known. Di-*tert*-butyl disulfide is a component of sulfurized isobutylene extreme pressure additive whose number of S atoms can vary between 1 and 6.[83, 226] The disulfide compound was selected as similar chemistries, i.e., dimethyl disulfide and diethyl disulfide, have been used in experimental studies on the reaction mechanism with iron surfaces.[148, 227] Here, the reactions of di-*tert*-butyl disulfide, a component of sulfurized isobutylene extreme pressure additive, [83, 226] confined and sheared between ferrous surfaces were studied using reactive molecular dynamics simulations at a range of temperature and pressure conditions, with or without base oil molecules, either on Fe(100) or H-passivated Fe_2O_3. The reaction pathways were analyzed, and then the effects of heat and pressure on each step in the pathway were quantified as the number of observed reaction events in the simulation. The yield of the rate-limiting step of the reaction was then fit to the classic Bell model [112] to quantitatively compare the three cases. The results provide a better understanding of reactions between di-*tert*-butyl-disulfide and ferrous surfaces, as well as the effects of environment and operating conditions on the film formation reactions of extreme pressure additives.

4.2 Methods

Three model systems were created, as shown in Fig. 4.1. The first model system, referred to subsequently as "Fe(100) + additive", consisted of 54 di-*tert*-butyl disulfide molecules confined between two Fe(100) slabs. The second model, called "Fe(100) + additive + base oil", incorporated *n*-dodecane as a model base oil. It consisted of 25 di-*tert*-butyl disulfide molecules

randomly mixed with 25 *n*-dodecane molecules (base oil) between two Fe(100) slabs. While this ratio does not reflect the low concentration of extreme pressure additives in bulk lubricant formulations, it approximates the expected higher density of adsorption of these additives on surfaces. Lastly, in the third model, called "Fe_2O_3 + additive", we replaced the ideal crystalline Fe surface of the first model with H-passivated Fe_2O_3 slabs, with 54 di-*tert*-butyl disulfide molecules in between. Simulations were performed using LAMMPS [176], Python scripts were used for post-processing, and the visualization of the results was carried out with OVITO [177].

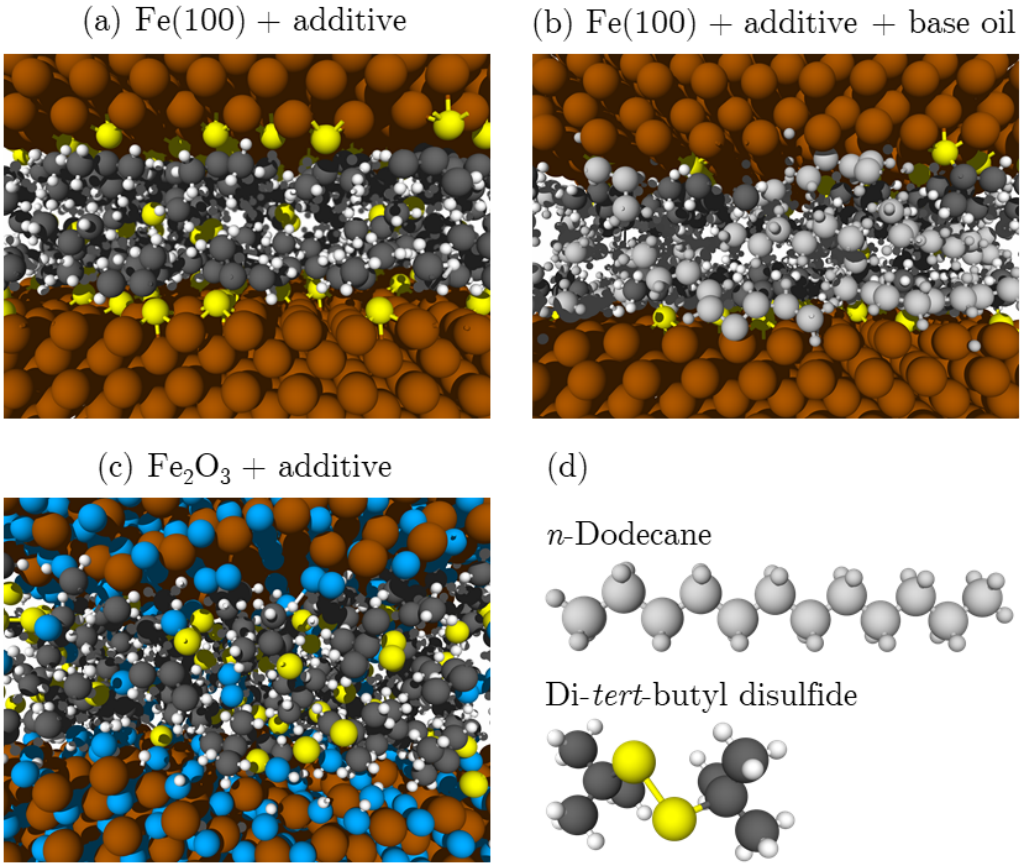

Figure 4.1: Side-view snapshots of the model systems (a) Fe(100) + additive, (b) Fe(100) + additive + base oil, and (c) Fe_2O_3 + additive. (d) Chemical structures of *n*-dodecane and di-*tert*-butyl disulfide. In all figures, the surface Fe and O atoms are shown in brown and blue, respectively. Di-*tert*-butyl disulfide atoms are shown in yellow (S), dark gray (C), and white (H). Both H and C atoms in the *n*-dodecane are shown in light gray to distinguish the base oil from the additive.

The structures of the di-*tert*-butyl disulfide and the *n*-dodecane molecules were obtained from PubChem [175] and duplicated using the Packmol [193] package. The Fe(100) slabs were created in Virtual NanoLab [174]. For the Fe(100) + additive and Fe(100) + additive + base oil models, the two Fe(100) slabs each had dimensions of 3.4×3.4×1.0 nm ($x \times y \times z$) and were initially positioned 2.0 nm and 3.5 nm apart, respectively. The H-passivated Fe_2O_3 slabs were created by heating two cyrstalline Fe_2O_3 slabs to 4000 K over 2.5 ps and then holding at that temperature for 125 ps. The model was then cooled from 4000 K to 300 K over 500 ps. The passivation process was carried out by placing 600 H atoms near the surface of each slab. The simulation was run at 700 K for 500 ps (to speed up the process) followed by cooling to 300 K over 250 ps at which point the potential energy of the system had reached steady state. Then, any H atom not bonded to the surface was removed from the model. The dimensions of the H-passivated Fe_2O_3 slabs were $3.6 \times 3.6 \times 2.5$ nm. The separation between the two slabs after the initialization process was 2.3 nm. For all models, periodic boundary conditions were applied in the directions parallel to the plane of the surfaces (x and y), and the boundaries were fixed in the direction normal to the surfaces (z). The atoms approximately 0.3 nm from the top and bottom of the models were treated as rigid bodies.

Interatomic interactions, including chemical bonding/de-bonding, were modeled using the ReaxFF potential [127] for Fe/S/C/H/O interactions using a parameter set developed by Shin *et al.* [147], with a time step of 0.25 fs. This force field has been used to model oxidation of butane on Cr_2O_3 in the presence of FeS_2 [147], reactions between H_2SO_4 and $Fe_3C(100)$ at high temperatures, [228] and carburization of iron nanoparticles in ethylene pyrolysis [229]. Further, the accuracy of the force field for di-*tert*-butyl disulfide on Fe(100) was evaluated previously by comparison of adsorption energies calculated by ReaxFF to those obtained from DFT [1, 230]. Thermostating of the model was performed by controlling the temperature of the Fe (and O) atoms in the middle layers of the Fe (H-passivated Fe_2O_3) slabs using a Langevin thermostat with a damping time constant of 25 fs. For simulations with relative motion of the slabs, the component of the kinetic energy in the direction of shear was excluded to remove the contribution of the imposed motion from the calculation of temperature used by the thermostat.

The simulations consisted of three stages – heat, load, and sliding – each 2 ns in duration. First, during the heating stage, the models were subjected only to heat at constant temperatures ranging from 500 K to 700 K. These temperatures were chosen both to accelerate the reaction due to time limitations of a reactive molecular dynamics simulation and to represent the flash temperatures expected in sliding contacts [148]. Next, a constant normal load was applied to the rigid part of the top slab while the positions of the atoms in the bottom slab were fixed, leading to contact pressures ranging from 0.50 GPa to 1.50 GPa. This pressure range is consistent with contact pressures in mechanical components with non-conformal contacts. During the loading stage, the top slab was allowed to move in the z-direction, which led to a reduction of the gap between the slabs. The distance between the slabs after loading was $\approx$1 nm, approximating the near-contact conditions of boundary or mixed lubrication at which extreme pressure additives operate in lubricated interfaces. Finally, during the sliding stage, the top and the bottom slabs were moved in opposite directions along the x direction at a speed of $\pm$5 m/s. The positions and bond orders of the atoms were recorded every 2.50 ps, and a covalent bond was identified when the bond order exceeded 0.3. The sliding stage was run at all temperatures and all pressures. The total number of temperature/pressure combinations was 30, 15, and 6 for the Fe(100) + additive, Fe(100) + additive + base oil, and Fe_2O_3 + additive models, respectively.

4.3 Results and Discussion

4.3.1 Reaction Pathways

Iron sulfide films are known to protect surfaces from friction and wear in lubricated mechanical systems [151, 231, 232]. The initiation of these reactions is the reaction between sulfur (S) in additives and surface iron (Fe). In a previous simulation-based investigation of the reaction between di-*tert*-butyl disulfide and Fe(100), [2] it was shown that this reaction occurs through three steps: S–S bond cleavage, followed by Fe–S bond formation, and lastly dissociation of the S–C bond. This pathway, here referred to as path *a* and shown in Fig. 4.2a, was observed in all three model systems studied here.

However, the presence of O and H in the H-passivated Fe_2O_3 surfaces introduced other reaction pathways, shown in Fig. 4.2b and 4.2c. These pathways both started with the S–S dissociation step, like pathway *a*. In reaction pathway *b*, the next step was chemisorption of the *tert*-butyl thiyl radical followed by dissociation of the S–C bond, leaving the S bonded to a surface O atom. In pathway *c*, the *tert*-butyl thiyl radical bonded with an OH radical released previously from the surface, then S–C bond dissociation took place, and finally the remaining sulfur-containing radical bonded with Fe or O on the surface. Chemisorption reactions in these pathways were equally likely (within the uncertainty of the simulations) on the top and bottom $Fe(100)/Fe_2O_3$ surfaces. For all three pathways, at the end of the reaction, most of the *tert*-butyl radicals either bonded to the surface or formed isobutylene. In very few cases, *tert*-butyl radicals associated with other sulfur-containing radicals to form larger intermediate species that later decomposed. Analysis of the likelihood of chemisorption showed that more *tert*-butyl radicals chemisorbed at higher pressures and temperatures.

The three reaction pathways can be summarized as:

Pathway a:
S–S cleavage $\rightarrow$ S–Fe formation $\rightarrow$ S–C dissociation
Pathway b:
S–S cleavage $\rightarrow$ S–Fe/S–O formation $\rightarrow$ S–C dissociation

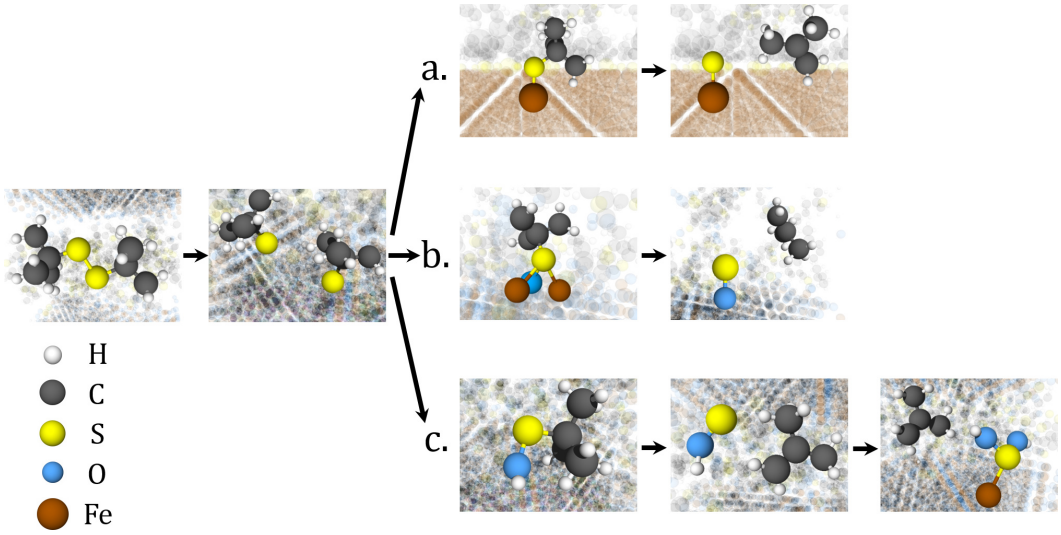

Figure 4.2: Three distinct reaction pathways were observed in the simulations. In all three pathways, the reaction involved S–S cleavage, S–C dissociation, and S chemisorption to the surface. The detailed steps in each pathway are described in the text.

Pathway c:
S–S cleavage → S–C dissociation → S–Fe/S–O formation

This general reaction pathway is consistent with that observed previously for dimethyl disulfide reacting on iron foil. [148] Importantly, although the steps of the three pathways differ slightly from one another, they all lead to sulfur bonded to the surface, which can be assumed to be the onset of formation of iron sulfide films that have been observed in tribological experiments. [151, 231, 232]

4.3.2 Reaction yield

Reaction yield was quantified in the simulations as the number of bonding/dissociation events calculated at the end of the shear stage relative to the total number of events possible given the number of di-*tert*-butyl disulfide molecules in each model system. This analysis was performed separately for each of the three main steps in the reaction: S–S cleavage, S–Fe/S–O formation, and S–C dissociation.

The S–S dissociation was always the first step in the reaction pathway. The yield for this reaction step from all simulations is summarized in Fig. 4.3a, b, and c, where yield is represented by color (dark corresponding to the highest yield) as a function of temperature on the abscissa and pressure on the ordinate axis. The heat map color indicates the model, where red corresponds to the Fe(100) + additive model, green to the Fe(100) + additive + base oil model, and blue to the Fe_2O_3 + additive system.

The heat maps show that this step of the reaction depends on temperature and pressure differently for the three model systems. For the Fe(100) + additive case, in Fig. 4.3a, S–S dissociation increases with both temperature and pressure. As shown in Figs. 4.3d and e, the effect of temperature is more significant at the lower pressures, and the effect of pressure is more significant at the lower temperatures.

In contrast, for the base oil containing model, the yield at any pressure or temperature in Figs. 4.3b, e, and h is above 90%. This indicates that nearly all of the possible bonds were broken by the end of the simulation under any condition, so temperature or pressure dependence could not be observed.

Lastly, for the H-passivated Fe_2O_3 model, the effect of temperature is more significant than the effect of pressure. As shown in Figs. 4.3c, f, and i, the yield of the S–S dissociation step increases rapidly with the increase in temperature from 500 to 700K, at any pressure. However, the effect of pressure is not significant at any temperature.

Fig. 4.4 shows the reaction yield for the Fe–S or O–S bond formation. The format of the sub-figures is the same as Fig. 4.3a, d, and g. For the Fe(100) + additive case, in Fig. 4.4, yield increases with pressure at all temperatures, with the effect of pressure being larger at

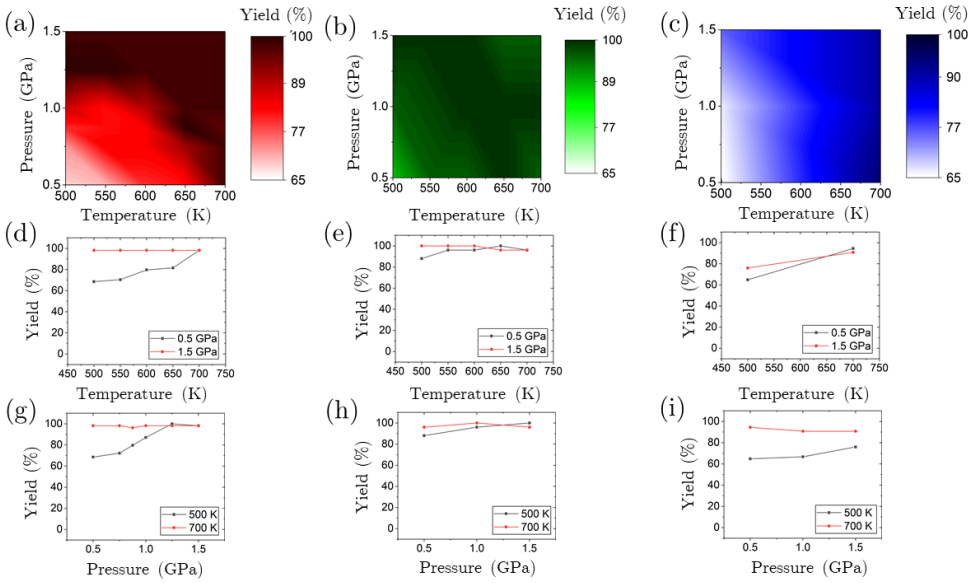

Figure 4.3: Heat maps (a, b, and c) of reaction yield for S–S bond cleavage (number of bonds broken at the end of the shear stage of the simulation) as a function of temperature and pressure. An increase in yield is shown by a color change from light (lowest) to dark (highest). The maps are created from 30, 15, and 6 data points for the red, green, and blue plots, respectively. Yield for models Fe(100) + additive, Fe(100) + additive + base oil, and Fe_2O_3 + additive are shown in red, green, and blue, respectively. 2D representations show the change in yield as a function of temperature (d, e, and f) at two pressures (0.5 and 1.5 GPa) and as a function of pressure (g, h, and i) at two temperatures (500 and 700 K).

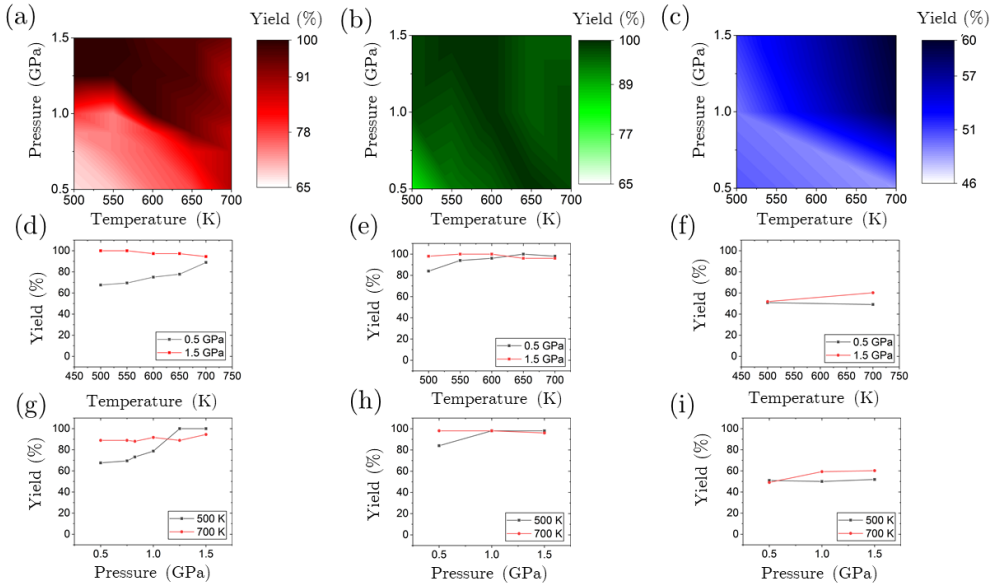

Figure 4.4: Heat maps of reaction yield for Fe–S (a and b) and Fe–S/O–S bond formation (c) as a function of temperature and pressure, and corresponding 2D plots at representative pressures and temperatures. The figure format and number of data points are the same as in Fig. 4.3. The heat map for the H-passivated Fe_2O_3 model had a smaller yield range than the plots of the other models.

lower temperatures. The thermal effect depends on pressure. Specifically, at low pressure, yield increases with increasing temperature, but the opposite is observed at high pressure. It has been observed from the simulations that some of the Fe–S bonds that form are subsequently broken by shear force at high pressure, and this process is facilitated by high temperature. The decrease is attributable to this bond breakage.

In the Fe(100) + additive + base oil case, shown in Figs. 4.4b, e, and h, like the S–S dissociation, nearly all possible Fe–S bonds are formed at any pressure or temperature. The maximum yield is reached for all cases except the lowest temperature and pressure conditions.

For the H-passivated Fe_2O_3 model, shown in Figs. 4.4c, f, and i, the reaction yield does not reach 100%. There is generally more yield at the higher pressures and temperatures, but yield does not increase significantly with either pressure or temperature.

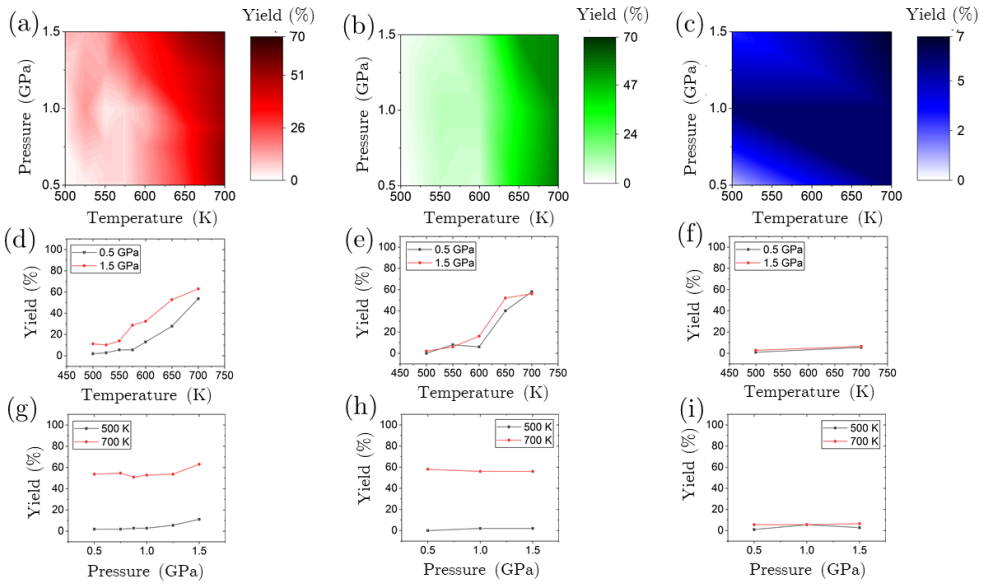

Figure 4.5: Heat maps of reaction yield for S–C dissociation as a function of temperature and pressure, and corresponding 2D plots at representative pressures and temperatures. Figure format and number of data points are the same as in Fig. 4.3. The 2D plots have the same range while the heat maps have different color ranges due to variation of the yield.

The final step we investigated was the dissociation of the S–C bond. Our previous studies identified this as the rate-limiting step of the reaction [1] and that its yield increased with increasing temperature and pressure [2]. The results for the three models here are shown in Fig. 4.5.

For the Fe(100) + additive case (Figs. 4.5a, d, and g), like in the previous two reaction steps discussed, yield increases with both pressure and temperature. However, for the S–C dissociation, the increase in yield with temperature is more significant than pressure.

For the model with base oil, shown in Figs. 4.5b, e, and h, this is the only reaction step that did not reach the maximum yield. Also, increasing the temperature increased yield at all pressures (Fig. 4.5e), although the reaction step did not appear to be accelerated by pressure (Fig. 4.5h).

Lastly, for the H-passivated Fe_2O_3 case, despite the fact that the yield increased slightly with temperature, very few reactions were observed under any set of conditions. The effects of base oil and H-passivated oxide surface on the reactions are discussed next.

4.3.3 Effect of base oil

Previous studies of film forming additives and base oil have shown that a higher concentration of additive relative to the base oil results in faster film formation [233, 234, 235, 236], because base oil that is chemically or physically adsorbed on the surface can limit access of the additives to the surface. [233] This suggests that the simulations with base oil present should have lower yield than those without base oil. However, the analyses in the previous section showed there was not much difference between the simulations with and without base oil.

The first two steps of the reaction achieved nearly 100% yield in both cases (Figs. 4.3 and 4.4). The third, rate-limiting step did not reach 100%, but the yield was comparable with and without the base oil (Fig 4.5). One reason that lower yield was not observed in the base oil case is that there were fewer di-*tert*-butyl disulfide molecules in the simulation with base oil; this was done to ensure that the model sizes would be approximately the same. Since yield is reported as the ratio of broken bonds to the total number of available bonds, the smaller number of additive molecules in the model with base oil resulted in a higher yield for the same number of broken bonds. Another difference between these simulations and experiments is the concentration of the additive. In experimental studies, the concentration of film forming additives is very low, typically less than 5 wt.%. [233] Due to the size-scale limitations of a MD simulation, an approximately 50 wt.% ratio was used here. As a result, there was very little base oil present in the model, and it had a negligible effect on yield.

Although the yield of the S–C dissociation step was similar for the cases with and without base oil, some difference in the effect of pressure was observed. For the model without base oil, there is an increase in yield with pressure in Figs. 4.5d and 4.5g. This pressure-dependence was confirmed by running two more simulations at a higher pressure (see Fig. 4.6). However, when base oil is present, no increase in yield with pressure is observed in Figs. 4.5e and 4.5h. Previous DFT calculations [12] and reactive MD simulations [2] have shown that the S–C dissociation reaction occurs through lateral displacement of the C atom with respect to the S atom. Shear stress therefore drives this step of the reaction by pushing the C atom along the reaction coordinate. In the simulations, the dodecane molecules were weakly bonded with the Fe(100) surface, but remained near the surface ($\approx$ 0.2 nm) throughout the simulations. Additionally, visualizations of the simulations showed that there were often dodecane molecules in the vicinity of the S–C bonds before dissociation. This suggests that the presence of the base oil impedes the lateral movement of the *tert*-butyl group, thereby minimizing the effect of mechanical stress to drive the reaction step.

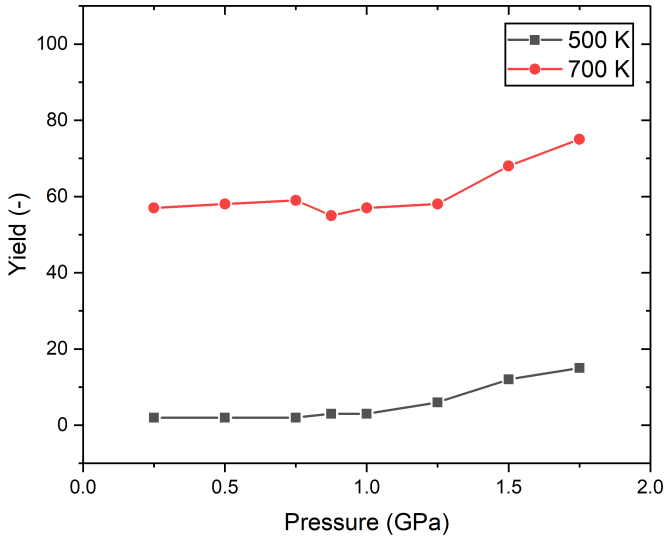

Figure 4.6: Yield of S–C bond dissociation as a function of pressure, including data from simulations run at pressures above 1 GPa, at two representative temperatures, 500 K (black) and 700 K (red). A noticeable increase in yield is observed at the higher pressures.

Lastly, our simulations showed that the dodecane molecules became aligned with the direction of sliding during the shear stage (see Fig.4.7). This phenomenon has been observed previously for dodecane molecules confined and sheared between mica surfaces, and the alignment was shown to lower friction. [237] The aligned dodecane molecules reduced the shear force and, consequently, decreased the pressure dependence of the reaction yield.

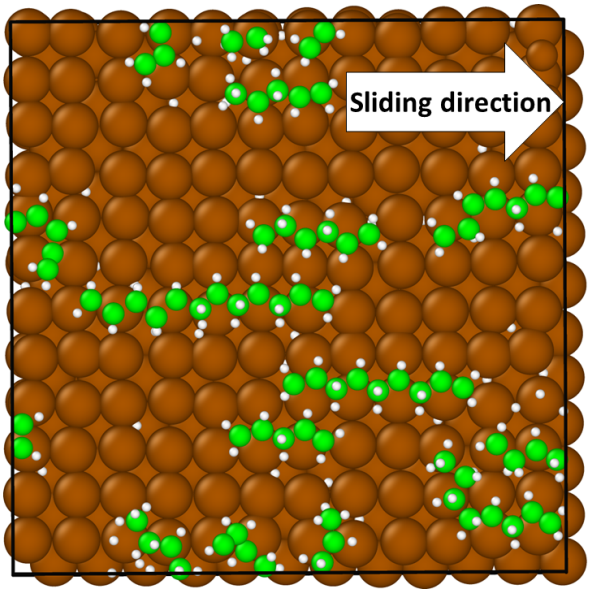

Figure 4.7: Representative top-view snapshot of the *n*-dodecane atoms close to the surface (within 0.5 nm) from the Fe(100) + additive + base oil simulation at 700 K and 1.5 GPa during sliding. Surface Fe atoms are shown in brown, near-surface *n*-dodecane H atoms in white, and near-surface *n*-dodecane C atoms in bright green. Some *n*-dodecane molecules appear to have too few C atoms due to the fact that only atoms close to the surface are shown. The direction of sliding is indicated by a white arrow. Results show that most dodecane molecules are aligned with the direction of sliding.

4.3.4 Effect of H-passivated oxide surface

Next, we analyzed the effect of the H-passivated oxide surface on film formation. For all three steps of the reaction, the yield was lower for the model with H-passivated Fe_2O_3 than either of the models with the Fe(100) surface. This difference can be attributed to several factors.

First, in the simulations with H-passivated Fe_2O_3, it was observed that the O and H atoms were released from the surface due to thermal as well as mechanical effects. These elemental H and O, as well as OH groups, are highly reactive and bonded with *tert*-butyl thiyl radicals (C_4H_9S), the main decomposition product, to form various oxide species (see Fig. 4.2). We also observed oxidation of di-*tert*-butyl disulfide molecules to derivative oxide species. Experimental studies have shown that when ZDDP is oxidized, the oxidation reaction products were ineffective as anti-wear agents. [238, 239, 240] This suggests that oxidation inhibited the ability of the additive to form protective films on surfaces, consistent with the observations in our simulations that the oxides formed from di-*tert*-butyl disulfide and its moieties were less likely to proceed through any of the reaction pathways.

Second, the chemical stability of the H-passivated Fe_2O_3 limits reactions with the surface. As seen in Fig. 4.4, the yield of the chemisorption step of the reaction for the H-passivated Fe_2O_3 is $\approx$50%, whereas it reaches nearly 100% for the other two cases. Experimental studies of reactions between disulfides and ferrous surfaces have shown that reaction rates are lower on oxide surfaces. [241, 242, 243] The H-passivated Fe_2O_3 surface was passivated with H in the simulations, prior to introducing the additive molecules, making it even more chemically stable. [244]

Lastly, Fig. 4.5 shows that the reaction yield of the rate-limiting step was much lower for Fe_2O_3 + additive than for the other two models. The models with Fe(100) proceed through pathway *a*, where chemisorption occurs via Fe–S bonding, whereas, in the H-passivated oxide model, S could bond with either Fe or O on the surface. Previous studies of a similar chemical system showed that more S–O bonds ($HSO-CH_3$ compared to HSO_3-CH_3) increased the S–C bond dissociation energy. [245, 246] Therefore, in our simulations, the S–O bonding to the *tert*-butyl sulfide moieties may have increased in S–C dissociation energy, leading to lower reaction yield.

4.3.5 Bell model

The results above are presented in terms of pressure, since load is the controllable/measurable parameter in an experiment (or a simulation mimicking an experiment). However, it is known that tribochemical reactions are driven by shear stress rather than by pressure alone [103, 104, 247]. Therefore, the change in yield with pressure observed here can be attributed to an increase in shear stress. The shear stresses in the simulations were calculated as a time average of the lateral force on the rigid part of the bottom and top Fe(100) (or H-passivated Fe_2O_3) slabs divided by the surface area (area of the model system in the xy plane).

The yield of a reaction is exponentially related to the height of the energy barrier that must be overcome for that reaction to proceed. The height of the barrier can be lowered by stress, leading to the classic Bell model [248]:

$$r_y = A \exp\left(-\frac{E_0 - \tau \cdot \Delta V^*}{k_B T}\right) , \tag{4.1}$$

where r_y is the reaction yield, A is a pre-exponential factor, k_B is the Boltzmann constant, T is the temperature, E_0 is the energy barrier in the absence of stress (thermal activation energy), ΔV^* is the activation volume, and τ is the shear stress. By taking the natural logarithm of Eq. (4.1), a linear relationship between the natural logarithm of the reaction yield and $(k_B T)^{-1}$ is obtained, where the slope corresponds to the reaction energy barrier:

$$\ln(r_y) = \ln(A) - \left(\frac{E_0}{k_B T}\right) + \left(\frac{\tau \cdot \Delta V^*}{k_B T}\right) \tag{4.2}$$

This framework is generally applicable to reactions driven by mechanical stress; for tribochemical reactions, it is used to quantify the effect of shear stress [203].

The reaction yield for the rate-limiting step of the reaction for each model system in Fig. 4.5 can be fit to Eq. (4.2). The multi-parameter fit was optimized by minimizing the mean of the squared differences between $\ln(r_y)$ as calculated from the Bell model and $\ln(r_y)$ as measured from our simulations (see Fig. 4.8). Fit parameters were $\ln(A)$, E_0, and ΔV^*. This fitting approach was previously used for shear-driven reactions. [249, 250]

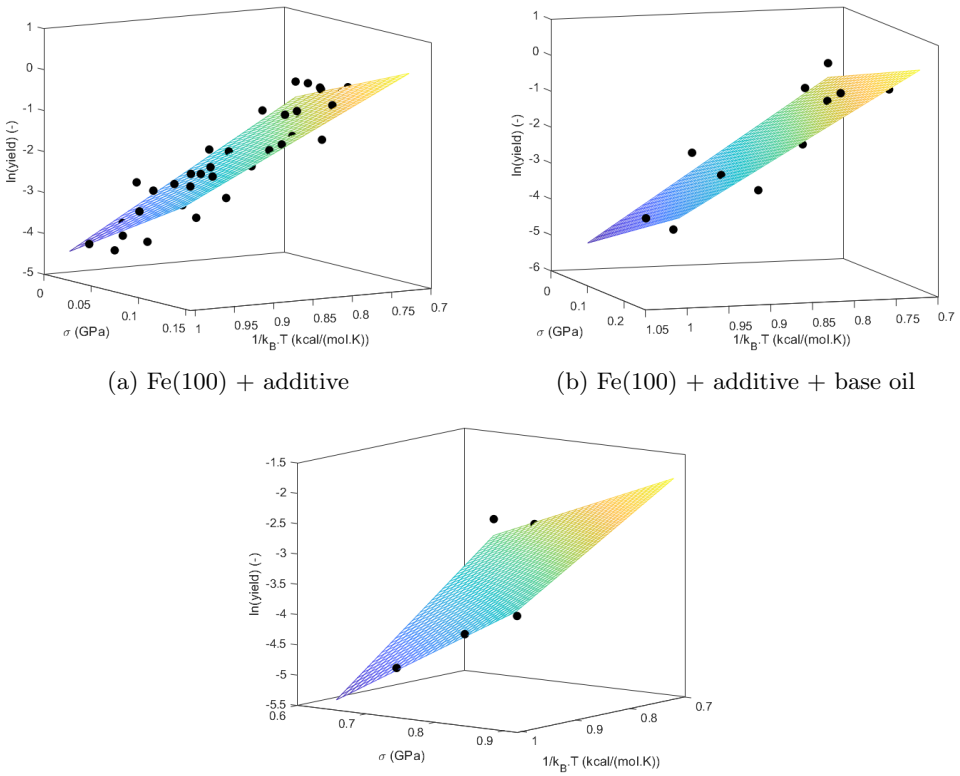

(a) Fe(100) + additive

(b) Fe(100) + additive + base oil

(c) Fe_2O_3 + additive

Figure 4.8: 3D plots of the multi-parameter fit of the S–C dissociation reaction yield to the Bell model for (a) Fe(100) + additive, (b) Fe(100) + additive + base oil, and (c) Fe_2O_3 + additive models. The data from the simulations are shown as black symbols and the prediction of the fit equation is represented as a color surface, where yield increases from purple to orange. All plots show the yield as a function of shear stress (σ) and inverse temperature ($1/k_BT$).

The first fit parameter, E_0, was found to be 11.8 ± 1.5, 12.6 ± 2.8, and 10.2 ± 4.4 kcal/mol for the Fe(100) + additive, Fe(100) + additive + base oil, and Fe_2O_3 + additive models, respectively. It has been reported that, if the reaction rate or yield is used in Eq. (4.2), as done here, the magnitudes of fit values for E_0 cannot be directly correlated to thermal activation energy [203]. Further, it has been shown that the availability of reaction sites is correlated to barrier height [151], so the finite size of the models here is expected to affect the fit value of E_0. However, for a series of systems that undergo similar chemical reactions, the relative magnitudes of E_0 obtained from linear fits are meaningful [203]. Therefore, the fact that the differences between the E_0 values for the three cases are less than the fit error indicates their thermal activation energies are similar.

More differentiation between the three cases was observed in the magnitude of the activation volume, which was found to be $\Delta V^* = 2.10 \pm 0.65$, 0.21 ± 0.59, and 0.75 ± 0.54 Å^3 for Fe(100) + additive, Fe(100) + additive + base oil, and Fe_2O_3 + additive, respectively. Although the physical meaning of activation volume has been debated, it is a measure of how susceptible a given reaction is to mechanical activation. [203] Therefore, the larger activation volume for the Fe(100) + additive case, with the comparable activation energies for all three cases, indicates that the S–C dissociation is most readily driven by shear for Fe(100) + additive.

As mentioned above, S–C dissociation occurs through lateral displacement of the C atom with respect to the S atom [12, 2], a process that is facilitated by lateral force. Shear can be transmitted from the walls to the molecules either directly, as is the case in pathways *a* and *b* when the *tert*-butyl sulfide is bonded to the surface, or indirectly by the strain field within the liquid, as would occur in pathway *c*. The latter case was demonstrated in a study of ZDDP film formation where the experiment was performed in full film lubrication, i.e., no surface-surface contact. [103]. The S–C dissociation is most readily activated by shear on the Fe(100) surface and without base oil because the direction of shear is perfectly aligned with the reaction pathway on the atomically smooth surface (unlike the H-passivated Fe_2O_3 surface). Additionally, base

oil is not present in the Fe(100) + additive model to impede the transmission of shear force from wall to reactant. Thus, compared to the Fe(100) + additive case, the activation volume is smaller with H-passivated Fe_2O_3 due to the lack of alignment of shear force with the reaction pathway and is smaller with base oil due to the interference of the base oil molecules in the transmission of shear force to the reactants.

4.4 Conclusions

In summary, the reaction pathways of di-*tert*-butyl disulfide on ferrous surfaces were investigated using reactive molecular dynamics simulations. The simulations were designed to evaluate whether mechanisms identified previously for the additive on a crystalline iron surface are relevant to more representative conditions with base oil or a surface oxide. Specifically, models were developed to simulate the additive in dodecane base oil and the additive on H-passivated Fe_2O_3, as well as the additive on Fe(100) for reference. Results showed that the reaction proceeded through different pathways, depending on the availability of O and H in the system. All reaction pathways consisted of three main steps: S–S cleavage, S chemisorption, and S–C dissociation. The reactions on Fe(100), with or without the base oil, always started with S–S cleavage followed by Fe–S bond formation and finally S–C dissociation, while on the H-passivated Fe_2O_3 surface, Fe-S bond formation and S-C dissociation occurred in either order after S–S cleavage.

Next, the effects of pressure and temperature on yield of the three steps of the reaction were quantified. The results showed that both temperature and pressure increased the reaction yield, indicating that the reaction could be driven thermally and mechanically. It was shown that the yield of all steps on the Fe(100) surface was higher than that of the model with the H-passivated Fe_2O_3 surface. This was attributed to three factors, the chemical stability of the H-passivated oxide surface, additive oxidation reactions that hindered the additive decomposition and chemisorption steps, and the increased S–C dissociation energy that lowered the yield of the rate-limiting step of the reaction.

Finally, the yield of the S–C dissociation step was investigated in the context of the Bell model. Fit values of activation energy for the three models were within the range of fit error, indicating that the presence of base oil or H-passivated Fe_2O_3 surface did not significantly affect the thermal activation energy. Additionally, the model with *tert*-butyl sulfide moieties on the atomically smooth Fe(100) surface in the absence of base oil had the largest fit activation volume. The lower activation volume of the other two models indicated that the ability of shear stress to drive these reactions was lessened by the presence of base oil or an H-passivated oxide surface.

The findings of this research are specifically relevant to the field of tribology, since a better understanding of how shear drives film formation reactions can potentially be leveraged in design of more energy efficient and longer lasting mechanical systems. Further, our study demonstrates an approach to predicting the pressure and temperature dependence of reactions between additives and surfaces, which is one of the important goals of tribochemistry, and can be applied to other additives as well as other relevant surfaces. This approach can be applied to quantify and understand mechanochemical reactions that are relevant to a wide range of current and potential applications.

Chapter 5

Development and Demonstration of a ReaxFF Reactive Force Field for Ni-doped MoS_2

5.1 Introduction

Molybdenum disulfide (MoS_2) is a transition metal dichalcogenide with a layered structure where each layer consists of molybdenum atoms sandwiched between sulfur atoms. Three main applications of the material are in catalysis, opto-electronics, and tribology. In catalysis, the chemically active edges of MoS_2 nanoparticles have been used to catalyze various reactions, including, hydrogen evolution, [54] hydrotreatment of oil,[55] and pollutant removal. [56, 57] Additionally, in 2D form, MoS_2 is widely used as a catalyst for hydrogen evolution reactions [58, 59, 60] and CO_2 reduction. [61, 62, 63, 64] In opto-electronics, single-layer MoS_2 is a semiconductor with a direct band gap that can be used to construct high efficiency transistors. [65, 66] MoS_2 can be synthesized by chemical vapor deposition to form large-area monolayers for use as atomically thin optical and photovoltaic devices. [67] In tribology, the weak van der Waals forces between layers provide low shear resistance, making MoS_2 an effective low-friction solid lubricant or, in nanoparticle form, a liquid lubricant additive. [47, 68, 69, 70]

MoS_2 can be doped to enhance its properties. [47] Many different elements have been explored as possible MoS_2 dopants, particularly transition metals. [47, 72, 73] Dopants can provide various benefits, including altering the band gap,[251] catalytic reactivity,[252] hardness,[81] and nanoscale friction.[253] Here, we focus on Ni dopants, which have been shown to improve the performance of MoS_2 for various applications. [254, 79, 55] DFT simulations have found four meta-stable sites for a Ni dopant atom in the 2H-MoS_2 crystallographic structure. [71] Dopants can replace an Mo or an S atom in the crystal structure, or they can be intercalated between MoS_2 layers, either between a sulfur site in one layer and a molybdenum site in the other layer (tetrahedral with 4 Ni–S bonds), or between hexagonal holes in both layers (octahedral with 6 Ni–S bonds). [255]

Experimental studies have investigated the atomistic structure of Ni-doped MoS_2 as well as its electronic and tribological properties. In doped MoS_2 nano-clusters, the Ni dopant was reported to substitute Mo atoms at edge sites leading to truncation of the cluster morphology relative to un-doped MoS_2. [72] Conversely, Ni doping has also been found to enhance MoS_2 crystal size by increasing the mobility of edge planes during crystallization. [256] In the process of MoS_2 growth, Ni doping has been shown to facilitate formation of edge-oriented MoS_2. [257, 258] It has been observed that Ni doping can also transform the 2H-MoS_2 structure to the metallic 1T phase. [259, 260]

Studies have shown that Ni doping increases the number of active sites which, in turn, improves the catalytic performance of MoS_2 in reduction of graphene oxide [261], gas sensing [73], and hydrogen evolution and production. [262, 263, 264, 254] Ni also increases the S-vacancy defect density, [265] resulting in better catalytic activity for hydrogen evolution reaction. [266] Ni doping changes the electronic properties of MoS_2 [267, 266, 268]: specifically, doping enhances the low electrical conductivity of MoS_2, making this material a promising candidate for electronic applications such as batteries. [269, 270] In tribology, it has been shown that MoS_2 films co-

sputtered with Ni compare favorably to un-doped MoS_2 in terms of friction, wear, and useful life of mechanical parts. [78, 79, 80, 81] The improvement in the tribological performance of MoS_2 is particularly notable at low temperatures, which makes Ni-doped MoS_2 ideal as a solid lubricant for space applications where performance at extreme conditions is critical. [74, 82]

Ni-doped MoS_2 has been studied using *ab initio* density functional theory (DFT) calculations. Such calculations have shown that the activity of edge sites is doubled [271] and that gas adsorption and sensing is enhanced [272, 273] by Ni. Other studies showed that Ni doping improves the catalytic performance of MoS_2 by decreasing the surface sulfur-metal bonding energy [274], as well as weakening the S–H bond strength. [275] Previous DFT-based studies have provided information about structures, thermodynamics, vibrational properties, elasticity, and interlayer binding in Ni-doped bulk 2H, bulk 3R, and monolayer 1H-MoS_2. [71, 255] DFT studies have also examined the energies and structural changes in frictional sliding of Ni-doped 2H and bilayer MoS_2, [276] and the range of different reconstructed phases accessible by Ni-doping of monolayer 1T-MoS_2. [277] However, such calculations are computationally demanding, limiting the time- and size-scales of model systems that can be studied.

An alternative simulation approach is molecular dynamics (MD) based on empirical models, or force fields, that describe the interactions between atoms. Several force fields have been developed, or optimized, for MoS_2, most of which are reactive, meaning they capture the formation and breaking of chemical bonds. First, a Stillinger-Weber force field was developed for MoS_2 and used to calculate mechanical and thermal properties of single layer MoS_2. [278, 279] However, the force field could not capture the behavior of MoS_2 at states far from equilibrium, [133] and did not include parameters for interlayer interactions. A many-body Mo/S potential based on the Reactive Empirical Bond Order (REBO) and Tersoff potentials was developed for MoS_2. [280] The force field was able to accurately reproduce expected lattice constants as well as mechanical properties of MoS_2, but it was unable to accurately model surface energy. Several force fields within the ReaxFF formalism have been parameterized for MoS_2 as well. [133, 140, 281, 138] These force fields have been used in simulations of crystallization, [133, 140, 281, 141, 138] active edge sites, [142] creation of vacancies, [133, 143, 282] distribution and dynamics of defects, [144] mechanical properties of MoS_2 monolayer heterostructures, [283, 284, 285] and tribological behavior of multi-layer MoS_2. [145] However, to investigate Ni-doped MoS_2, force field parameters that include the interactions between Ni and MoS_2 are needed, which is a challenge as new interactions are introduced, and the dopant's effect on the otherwise weak interlayer interactions must be described.

In this study, two new ReaxFF force fields were developed for Ni-doped MoS_2. The force field parameters were optimized by comparing ReaxFF energies to those obtained from a large set of DFT calculations of the equation of state of Ni-doped 2H-MoS_2 under uniaxial, biaxial, triaxial, and in-plane shear strain. DFT calculations were performed with Ni dopants at each of four different sites: Mo-substituted, S-substituted, octahedral, and tetrahedral intercalation. The resulting ReaxFF force field was validated by calculations of relaxed bond lengths and structural parameters in 2H, and as well as calculations of structures not in the training set such as doped 1H and 1T monolayers and doped 2H with vacancies. Finally, we demonstrated the use of the new force field to the study of sputter deposition and annealing of Ni-doped MoS_2, pointing the way to future applications.

5.2 Methods

5.2.1 DFT Calculations

As in our previous work on thermodynamics and vibrational properties of Ni-doped MoS_2[71], the plane-wave density functional theory (DFT) code Quantum ESPRESSO[286] was used for quantum calculations. The Perdew-Burke-Ernzerhof[287] (PBE) generalized gradient approximation was used with Grimme-D2[288] van der Waals correction, and the electron-ion interaction was described with optimized norm-conserving Vanderbilt pseudopotentials[289] parametrized by Schlipf and Gygi.[290] All DFT computations used a kinetic energy cutoff of 60 Ry. PBE + Grimme-D2 has been shown to accurately describe the lattice parameters, elastic constants, and phonon frequencies of MoS_2.[71]

The training set was composed of 2H-MoS_2 in $2 \times 2 \times 1$ supercells, where the third direction is perpendicular to the basal plane of the layers. Pristine 2H-bulk structures have six atoms per unit cell; a half-shifted Monkhorst-Pack k-grid of $4 \times 4 \times 4$ was used. Atomic coordinates were

relaxed using force thresholds of 10^{-4} Ry/Bohr and the stresses were relaxed to 0.1 kbar. The relaxed lattice parameters of the hexagonal cell are $a = b = 3.19$ Å, $c = 12.40$ Å, $\alpha = \beta = 90°$, and $\gamma = 120°$. The dopant sites were chosen because they are stable or meta-stable [71]; other sites such as intralayer interstitial or S–S bridge intercalation would relax to other structures. The stable doped structures (Mo-substituted, S-substituted, and intercalation at the tetrahedral and octahedral sites, shown in Figure 5.1) were taken from [71], constructed with one Ni atom in each $2 \times 2 \times 2$ supercell. For validation, bilayer calculations used identical parameters except for fixed large c-parameters and only one k-point in the z-direction, and defect calculations in $3 \times 3 \times 1$ supercells used a $3 \times 3 \times 4$ k-grid. The training set systems are shown in Figure 5.1. For convenience in reactive MD calculations, the results were used to construct nearly orthorhombic ($\alpha = \beta = 90°$) conventional cells with twice the number of atoms and twice the energy.

Strained 2H-bulk structures were studied under six strain conditions: uniaxial x-strain, uniaxial z-strain, biaxial xy-strain, triaxial strain, and xy-shear. Note that due to exact symmetries in the pristine structure, and approximate symmetries in the doped structures,[71] uniaxial y-strain would not provide further distinct information. For each strain direction, seven points were sampled with large strains ranging from -15% to 15% in intervals of 5%. Similarly, shear calculations were performed for seven points with shearing angle (the angle between orthogonal a and b lattice vectors as shown in the inset of Figure 5.6b) between $\sim 72°$ and 108°. In each case, the atomic forces were relaxed to 10^{-4} Ry/Bohr with fixed lattice vectors.

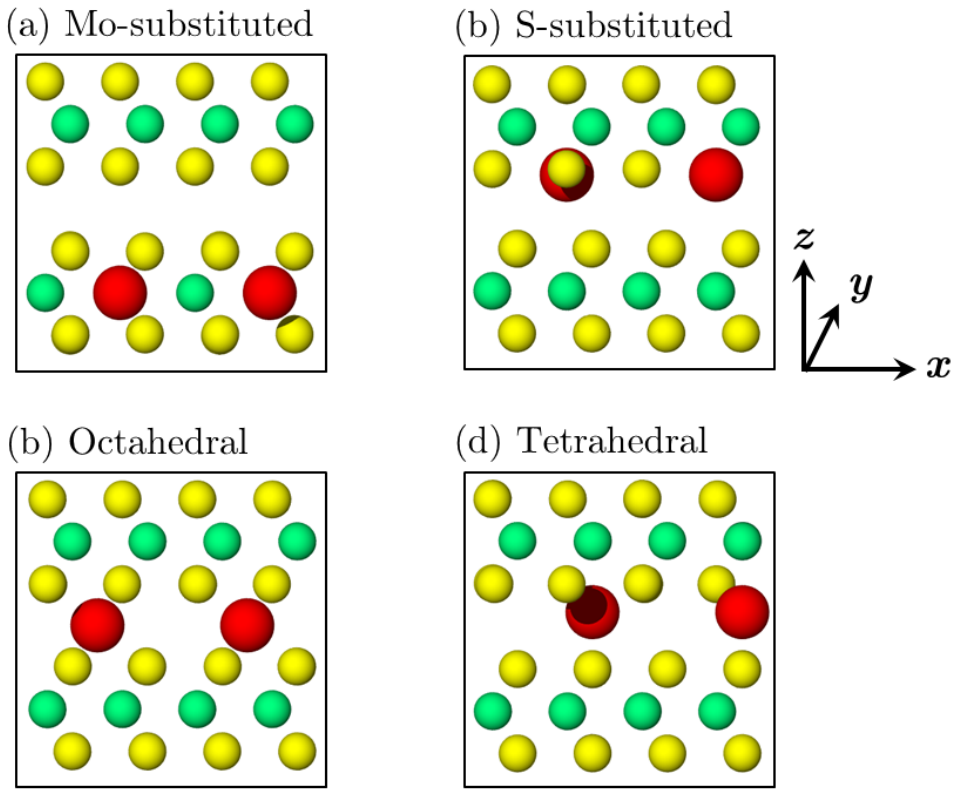

Figure 5.1: Side views of the training set structures, illustrating the four possible locations of the Ni dopant within MoS_2: (a) Mo-substituted, (b) S-substituted, (c) octahedral intercalation, and (d) tetrahedral intercalation. Sphere colors indicate S (yellow), Mo (green), and Ni (red). The structures shown in this figure were obtained by Enrique Guerrero, Department of Physics, University of California, Merced.

5.2.2 ReaxFF Force Field and Parameterization

ReaxFF is a reactive empirical force field based on bond order and bond distance that originally was developed for hydrocarbons. [127] Over the years, many different parameters have been developed for various chemical systems. ReaxFF accounts for the contributions of various partial energy terms. These terms include bond energy, valence angle, torsion angle, as well as van der

Waals and Coulomb interactions. This allows ReaxFF to accurately consider covalent and ionic bonds as well as non-bonded interactions. The total energy in the force field is the sum of the bond energy, over-coordination and under-coordination energy corrections, angle strain, torsion energy, torsion conjugation, van der Waals, and Coulomb energies. A detailed explanation of all terms can be found in the original ReaxFF article. [127]

We started from two different parameter sets that were previously developed for S/Mo interactions, one reported in 2017 [133] and the other reported in 2022. [138] The 2017 potential was developed specifically for single-layer MoS_2, with a focus on its mechanical response with and without vacancies, and included parameters to model interactions between MoS_2 and oxygen. Then, the 2022 potential was developed by modifying the Mo/S parameters in the 2017 potential to better capture crystallization of MoS_2 in bilayer and bulk form. We introduced Ni parameters for both the 2017 and the 2022 force fields, starting with Ni/Mo [291] and Ni/S [292] parameters reported in previous studies. Since this study uses bulk DFT training data, and has an application focus on deposition of crystalline MoS_2, we report the results for the new potential based on the 2022 parameters in the main text. However, results for the potential based on the 2017 force field as well as both potential files are available as supporting information.

Our force field was trained against the DFT data by optimizing the parameters specifically for Mo-S-Ni, S-Mo-Ni, and S-Ni-Mo valence angles. These parameters were the equilibrium angle, first and second force constants, undercoordination parameter, and energy/bond order. The process of parameterization included calculating the potential energy of each structure (E^{ReaxFF}) which was then compared to the energy obtained from DFT for the same structure (E^{DFT}). A weighted error was calculated as:

$$\text{Error} = \sum_i \left(\frac{E_i^{\mathrm{ReaxFF}} - E_i^{\mathrm{DFT}}}{w_i} \right)^2 \tag{5.1}$$

where w_i is the weight associated with each data point on the energy plots. The weights were chosen to prioritize minimizing the difference between the DFT and the ReaxFF energies for near-equilibrium structures. The parameters were optimized by the single-parameter search optimization technique [293] in the stand-alone ReaxFF package. The energy difference between each strained and equilibrated structure as obtained from ReaxFF and DFT was plotted as a function of strain for each strain direction. The same was done for sheared structures at each shearing angle. The parameterization process was repeated until the shapes of the energy plots were as similar as possible between ReaxFF and DFT. This procedure has been used previously to optimize ReaxFF parameters for various chemical systems. [133, 294, 295, 296, 4, 138] The developed force field was evaluated and then demonstrated using energy minimization and dynamics simulations with the Large-scale Atomic/Molecular Massively Parallel Simulator (LAMMPS) code. [176]

5.3 Results and Discussion

5.3.1 Force Field Parameterization

The energies of all 4 structures under all 5 strain conditions were used in the training of the ReaxFF force field. The results for uniaxial straining in the x- and z-directions of the four Ni-doped MoS_2 structures are shown in Figure 5.11 and Figure 5.12, respectively. The equation of state energies given are those of the conventional cell, with respect to the energy in each method of the unstrained structure. The structures used in ReaxFF are those from DFT, with no structural relaxation performed.

The uniaxial ReaxFF energies are in reasonably good agreement with the DFT energies, despite the large strains that were applied. Discrepancies are largest at large strain. Shapes are similar, though for x strain and S-substituted, ReaxFF actually has a minimum shifted to +5% strain, and for z strain and Mo-substituted the minimum is shifted to -5%. For x strain, Mo-substituted has larger energy value in ReaxFF than in DFT for all strains, whereas in the other cases, ReaxFF is higher for compressive strains and lower for tensile strains. For z strain, the ReaxFF energies are larger than in DFT in general, showing an overestimation of the elastic modulus in the z direction.

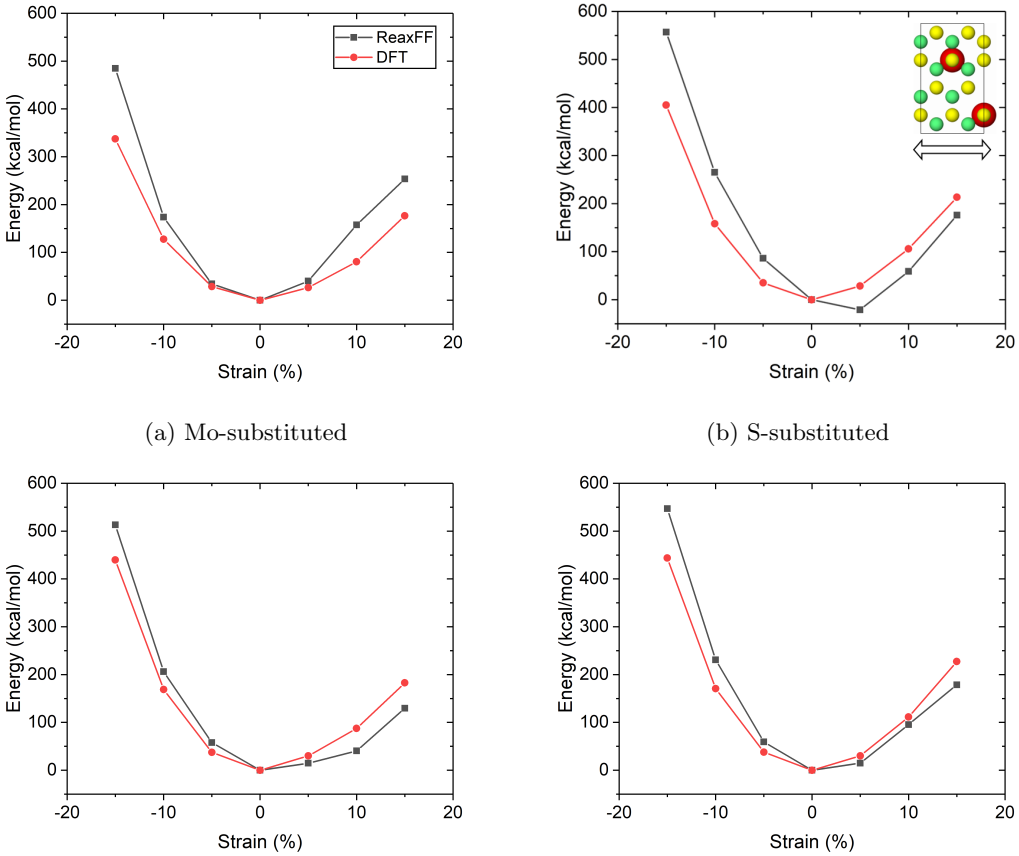

(a) Mo-substituted

(b) S-substituted

(c) Octahedral

(d) Tetrahedral

Figure 5.2: Equations of state calculated from DFT (red) and ReaxFF (black) for structures strained uniaxially in the x-direction. The inset in (b) shows a top view of the S-substituted structure with an arrow indicating the strain direction. The DFT energies in this figure were obtained by Enrique Guerrero, Department of Physics, University of California, Merced.

The results for biaxial and triaxial straining are shown in Figure 5.4 and 5.5, respectively, providing significantly better ReaxFF/DFT agreement. The energies as obtained from DFT calculations for the highest strains are $\sim$ 1000 kcal/mol for biaxial strain and even higher (up to $\sim$ 1800 kcal/mol) in the case of triaxial strain. Nevertheless, our force field is in excellent agreement with the DFT for the case of biaxial as well as triaxial straining. The ReaxFF energies are in good agreement for both the near-equilibrium structures and the far-from-equilibrium energies, and provide the correct minimum energy at zero strain.

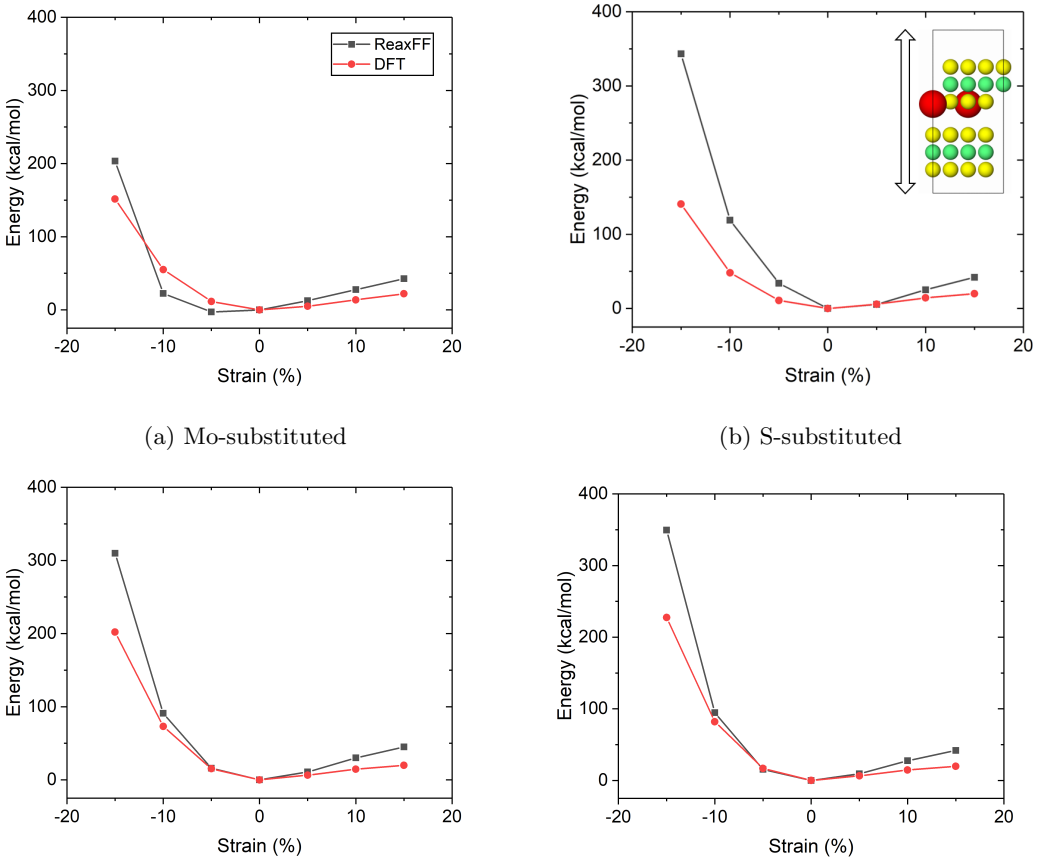

(a) Mo-substituted

(b) S-substituted

(c) Octahedral

(d) Tetrahedral

Figure 5.3: Equations of state calculated from DFT (red) and ReaxFF (black) for structures strained uniaxially in the z-direction. The inset in (b) shows a side view of the S-substituted structure with an arrow indicating the strain direction. The DFT energies in this figure were obtained by Enrique Guerrero, Department of Physics, University of California, Merced.

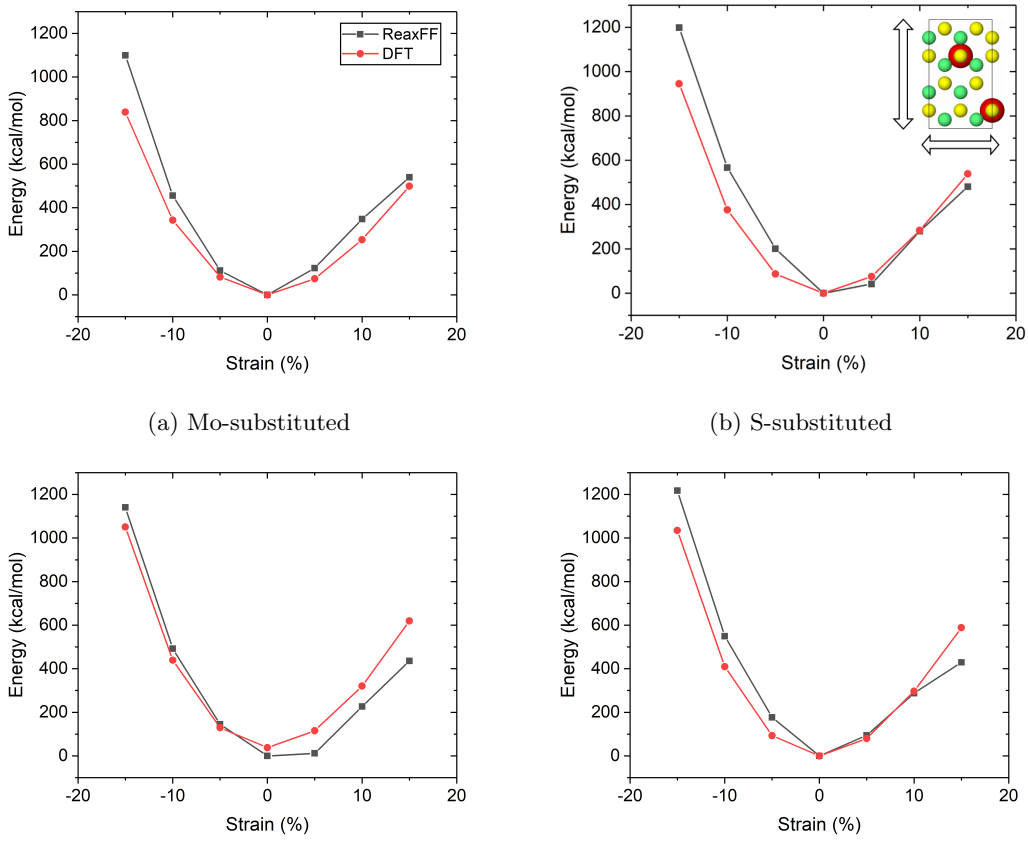

(a) Mo-substituted

(b) S-substituted

(c) Octahedral

(d) Tetrahedral

Figure 5.4: Equations of state as obtained from DFT (red) and ReaxFF (black) for structures strained biaxially for Mo-substituted, S-substituted, octahedral, and tetrahedral positions. The inset in (b) shows a top view of the S-substituted structure with two arrows indicating the strain directions. The DFT energies in this figure were obtained by Enrique Guerrero, Department of Physics, University of California, Merced.

Finally, the ReaxFF energies for sheared structures were compared with DFT. Figure 5.6 shows excellent agreement for near-equilibrium as well as far-from-equilibrium structures. The minimum is correctly at 90° and the shape is close and correctly symmetrical. Mo-substituted has an overestimated shear modulus whereas S-substituted is very close, and octahedral and tetrahedral intercalation have an underestimated shear modulus.

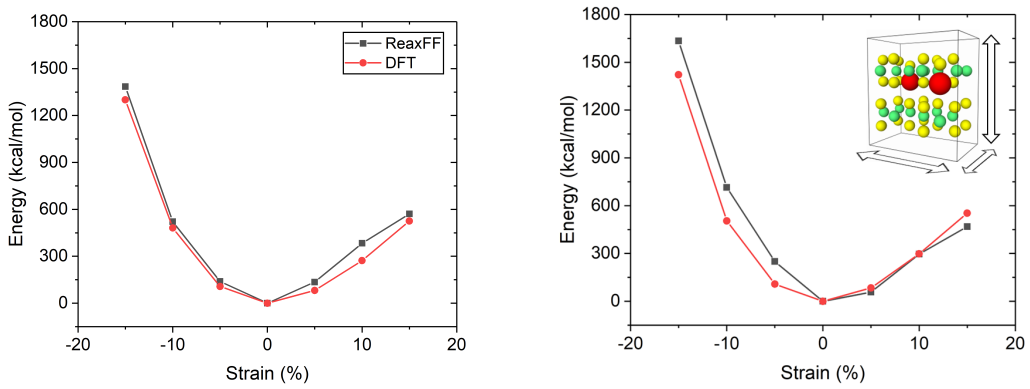

(a) Mo-substituted

(b) S-substituted

(c) Octahedral

(d) Tetrahedral

Figure 5.5: Equations of state as obtained from DFT (red) and ReaxFF (black) for structures strained triaxially for Mo-substituted, S-substituted, octahedral, and tetrahedral positions. The inset in (b) shows a perspective view of the S-substituted structure with three arrows indicating the strain directions. The DFT energies in this figure were obtained by Enrique Guerrero, Department of Physics, University of California, Merced.

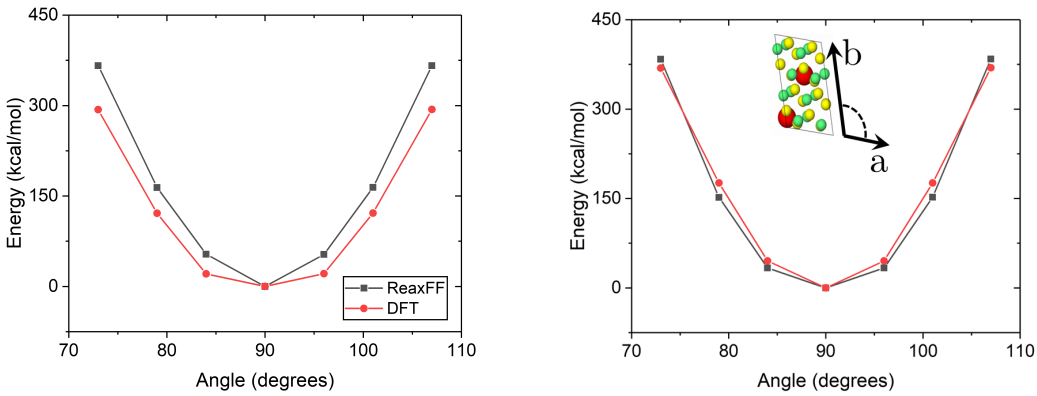

(a) Mo-substituted

(b) S-substituted

(c) Octahedral

(d) Tetrahedral

Figure 5.6: ReaxFF (black) and DFT (red) energies obtained for sheared structures in the xy basal plane for (a) Mo-substituted, (b) S-substituted, (c) octahedral, and (d) tetrahedral structures. The inset in (b) shows a top view of the basal plane of the S-substituted structure with arrows indicating the shearing angle as calculated from the angle between in-plane conventional cell vectors a and b. The DFT energies in this figure were obtained by Enrique Guerrero, Department of Physics, University of California, Merced.

5.3.2 Force Field Evaluation

Next we evaluated the force field's ability to predict parameters that were not included in the training. This evaluation was based on atom positions and distances obtained from energy minimization of the model structures using the conjugate gradient algorithm with force and energy criteria of 10^{-6} $\frac{kcal}{mol.Ansgtrom}$ and 10^{-6} (unitless), respectively. The cell was fixed and the minimization began from the DFT equilibrium structures. First, the Ni–Mo and Ni–S atomic distances in all four structures were calculated. Results for Ni–Mo and Ni–S bond lengths are shown in Table 5.1a and 5.1b, respectively.

In most cases, the differences between ReaxFF and DFT bond lengths were within 0.1 Å, indicating the force field can accurately capture bond lengths within the Ni-doped MoS_2 structure. The local symmetry around Ni, as shown by the multiplicity of the atomic distances, was correctly preserved in each case. However, for S-substituted and octahedral structures, ReaxFF predicted the position of the Ni atom to be slightly out of the MoS_2 layer. This caused the ReaxFF and DFT predicted Ni–Mo bond lengths be off by 0.13 Å and 0.19 Å, respectively. It is worth mentioning that even for the mentioned structures, the Ni–S bonds are still consistent within 0.1 Å.

Next, the force field's ability to reproduce Ni-doped MoS_2 structures with correct lattice parameters was tested. The parameters considered, illustrated in Figure 5.7, were the lattice constant a, the average distance h between S planes in a single layer, and the average interlayer separation d. The values for these parameters after energy minimization in DFT and with ReaxFF are shown in Table 5.2. The difference between the DFT- and ReaxFF-calculated

Table 5.1: Atomic distances (below 3.6 Å) between Ni and its neighbors from DFT and ReaxFF. Repeated distances are indicated with a multiplier. The DFT results used in this table were obtained by Enrique Guerrero, Department of Physics, University of California, Merced.

(a) a. Ni–Mo distances

Structure	DFT (Å)	ReaxFF (Å)
Mo-substituted	3.20 ×6	3.19 ×6
S-substituted	2.55 ×3	2.68 ×3
Octahedral	3.57 ×6	3.36 ×6
Tetrahedral	2.61 ×1	2.71 ×1

(b) b. Ni–S distances

Structure	DFT (Å)	ReaxFF (Å)
Mo-substituted	2.38 ×3	2.38 ×3
S-substituted	3.18 ×6	3.18 ×6
Octahedral	2.34 ×3, 2.38 ×3	2.31 ×3, 2.46 ×3
Tetrahedral	2.17 ×3, 2.12 ×1	2.25 ×3, 2.20 ×1

parameters was less than 0.1 Å for most doped structures, as well as the pristine MoS_2 case which is shown for reference and relies only on the pre-existing Mo-S potential. This is consistent with the equation of state findings, since the optimized values of a and $c = 2h + 2d$ are by definition the minima of the uniaxial x and z curves.

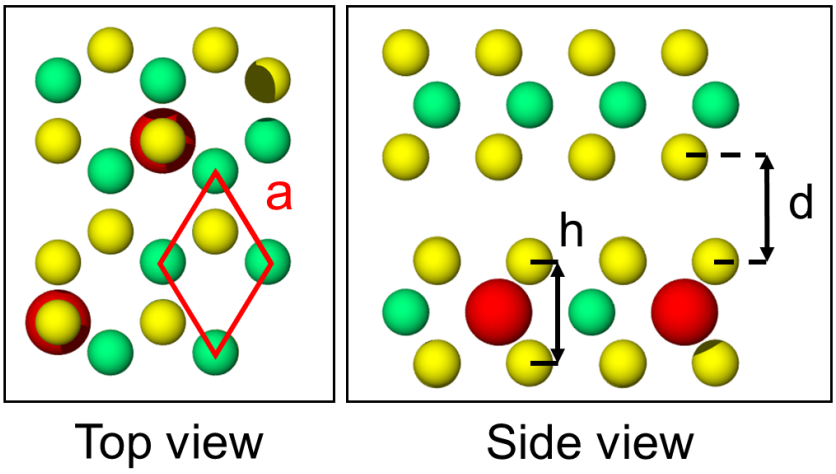

Figure 5.7: Structural parameters for Ni-doped MoS_2 illustrated for Mo-substituted configuration: in-plane lattice constant a, average distance h between S planes in a single layer, and average interlayer separation d.

The accuracy of the developed force field was also tested in distinguishing the relative energies of Ni-doped 1H and 1T monolayer structures. We used 2×2, 3×3, and 4×4 in-plane supercells of the three-atom unit cell of 1H and 1T, where each supercell contained one Ni atom; these structures were then doubled to create orthogonal unit cells with two Ni atoms per cell. The different doping sites [255, 277] were: adatoms at the hollow position (three-fold hollow space between top S atoms), Mo atop (on top of Mo), or S atop (on top of S); Mo-substituted, or S-substituted. The pristine structures were also included for reference, which had been studied in the 2017 work. [133] Note that neither 1H or 1T structures nor adatoms were in our training data. Snapshots of representative structures (S atop) of different sizes are shown in Figure 5.8.

Table 5.2: Structural parameters (Å) compared between ReaxFF and DFT. The DFT results used in this table were obtained by Enrique Guerrero, Department of Physics, University of California, Merced.

Structure	a-DFT	a-ReaxFF	h-DFT	h-ReaxFF	d-DFT	d-ReaxFF
Pristine	3.19	3.18	3.12	3.13	3.08	3.07
Mo-substituted	3.20	3.20	3.01	3.07	3.05	2.96
S-substituted	3.17	3.17	3.12	3.39	2.93	2.65
Octahedral	3.19	3.33	3.12	3.29	3.04	2.87
Tetrahedral	3.19	3.19	3.12	3.28	3.16	3.00

The energy differences between 1H and 1T polytypes were compared between ReaxFF and DFT in Figure 5.8, using DFT results from [255] and [277].

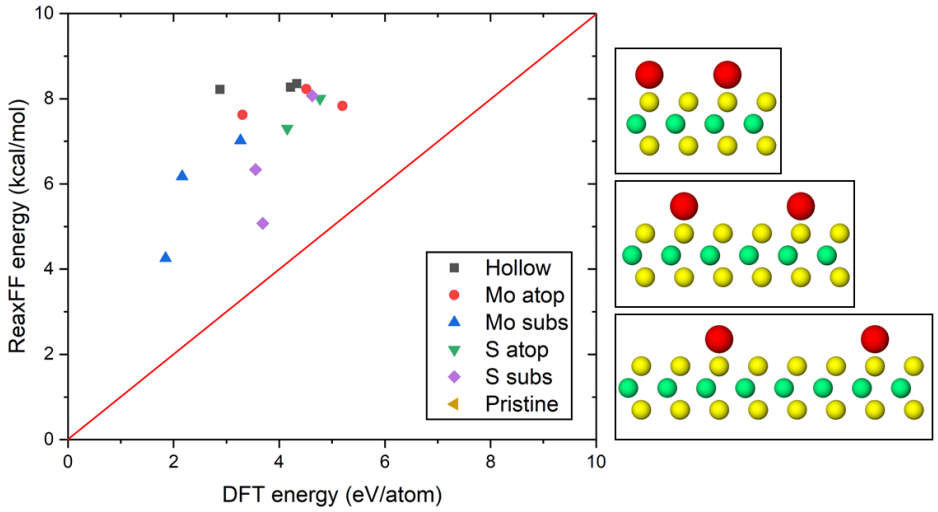

Figure 5.8: Energy difference between 1H and 1T polytypes for each structure of Ni-doped (or pristine) MoS_2. Results show an approximately linear relationship between DFT and ReaxFF energy differences, with underestimation by ReaxFF for higher energy configurations. Snapshots (right) show 2×2, 3×3, and 4×4 supercells of S atop site of 1H-MoS_2. The DFT energies shown in this figure were obtained by Enrique Guerrero, Department of Physics, University of California, Merced.

Given the prevalence of vacancies in real MoS_2 [297] samples, and studies of vacancies with the 2017 ReaxFF potential,[133] we tested our reactive force field on defective bulk 2H structures that combine Mo and S vacancies and Ni dopants. Structures based on a $3 \times 3 \times 1$ supercell were constructed and underwent variable-cell relaxation in DFT, and then the DFT-relaxed structure was converted to a conventional cell, imported to ReaxFF and relaxed using the developed force field. The goal to have an agreement between DFT and ReaxFF required that the final (i.e., after relaxation) atomic positions of Ni-doped MoS_2 atoms be the same (i.e., no structural changes during ReaxFF relaxation). A summary of atomic rearrangements during each relaxation is shown in Table 5.3.

Table 5.3 shows that, according to DFT, for the intercalated structures, Ni moved to the vacancy position, essentially converting an intercalated structure to a substituted structure (Mo-substituted for Ni→Mo and S-substituted for Ni→S). This observation is consistent with the findings in [71] that the formation energy for tetrahedral intercalation in a $3 \times 3 \times 1$ supercell is 0.401 eV, greater than the energy for filling an Mo vacancy with Ni (-2.575 eV), and for filling an S vacancy (0.194 eV). The formation energy for octahedral intercalation is 0.9 eV higher, making the migration to a vacancy yet more exothermic. The calculations performed here additionally

Table 5.3: Summary of atomic rearrangements of 2H-MoS_2 with a Ni dopant and a vacancy, both at variable locations. In intercalations and S-substituted with a vacancy, Ni moves into the vacancy. All rearrangements predicted by DFT remain in ReaxFF. The DFT results used in this table were obtained by Enrique Guerrero, Department of Physics, University of California, Merced.

Ni initial site	Vacancy initial site	Ni relaxed site	Vacancy relaxed site
Mo	Mo	Mo	Mo
Mo	S	Mo	S
S	Mo	Mo	S
S	S	S	S
Octahedral	Mo	Mo	-
Octahedral	S	S	-
Tetrahedral	Mo	Mo	-
Tetrahedral	S	S	-

show that these migrations have no barrier. The ReaxFF relaxed structures preserved the same rearrangements as in DFT for all combinations of dopant and vacancy positions.

5.3.3 Simulations of Deposition and Annealing

To demonstrate the newly developed force field, the process of sputter deposition and annealing to grow Ni-doped MoS_2 films [298] was simulated. The simulations were performed using LAMMPS in the NVE ensemble with the Langevin thermostat, a damping parameter of 10.0 fs, and a time step of 0.1 fs. The simulation box was $2.5 \times 2.4 \times 10.0$ nm in the x-, y-, and z-directions, respectively, with periodic boundary conditions in the x- and y-directions. The initial configuration was two sheets of AB-stacked 2H-MoS_2 with a total thickness of 1.0 nm, with the bottom-most layer of the substrate held fixed during the simulation. Atoms were deposited from 7.0 nm above the substrate surface, and a reflective virtual wall (which reflects downward only) was placed parallel to the surface at a distance of 4.8 nm to ensure deposited atoms remain near the substrate. The deposition process followed a simulation protocol used previously for SiO_2 thin film formation. [299] First, energy minimization was performed to obtain the relaxed atomic positions, followed by thermal equilibration for 50 ps at room temperature. Next, Mo, S, and Ni atoms were continuously deposited onto the MoS_2 substrate at a 1:2 Mo to S ratio with Ni atoms replacing Mo atoms as 7% by weight, expected to promote Ni substitution for Mo. [81] The deposition rates for Mo and Ni were one atom every 40 fs with a deposition energy of 230 kcal/mol; for S atoms the deposition rate was one atoms every 20 fs with a deposition energy of 1.5 kcal/mol. The total number of deposited S, Mo, and Ni atoms after 50 ps was 1000, 405, and 95, respectively. At the end of the deposition process, the system was relaxed at 300 K for 50 ps. The second stage was annealing the deposited Ni-doped MoS_2 film, following the simulation process used previously for the crystallization of un-doped MoS_2. [138] The annealing process was carried out by heating the model at the end of the deposition stage to 5000 K over 50 ps at a ramping rate of 100 K/ps. The structure was equilibrated at high temperature for 50 ps. Then, the structure was cooled to 2000 K at a rate of 30 K/ps followed by equilibration for 300 ps to trigger nucleation. Finally, the model was cooled to 300 K over 170 ps (10 K/ps).

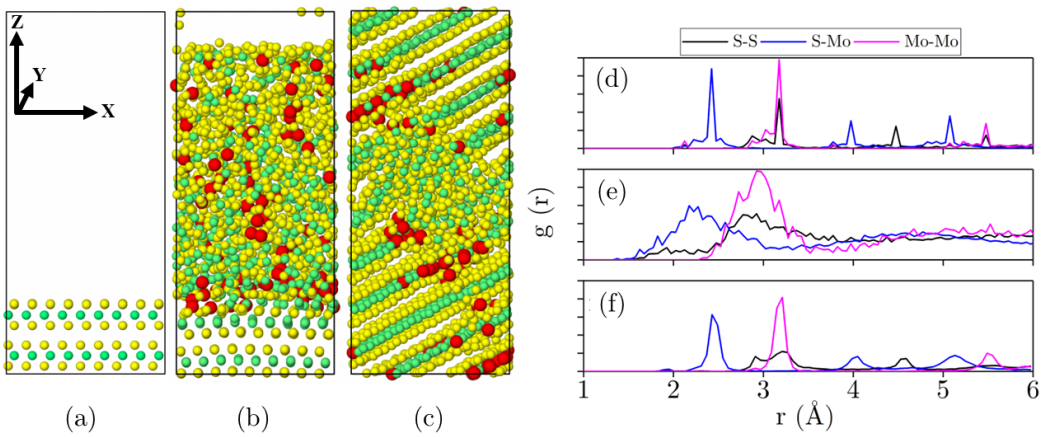

Figure 5.9: Side-view snapshots of the model system (a) before deposition, (b) at the end of the deposition, and (c) at the end of the annealing stage. A clear transition from amorphous to crystalline is observed (b) → (c). Spheres represent S (yellow), Mo (green), and Ni (red) atoms. Radial distribution functions are shown in (d), (e), and (f) for before deposition, after deposition, and after annealing, respectively. This figure was partly created by Sergio Romero Garcia, Department of Mechanical Engineering, University of California, Merced.

Snapshots of the model system before deposition, after deposition, and after annealing are shown in Figure 5.9(a), (b), and (c), respectively. Visually, the model system appears amorphous at the end of deposition, consistent with experimental observations for magnetron-sputtered MoS_2, [300, 298] but then is mostly crystalline after annealing, as observed after annealing in experiments. [300, 298] Note that the middle region of the material (Figure 5.9(c)) does not appear crystalline from this view, but is in fact crystalline at an angle relative to the perspective shown here. The crystallization process can be quantified using radial distribution functions (RDFs) of S–S, S–Mo, and Mo–Mo atom distances at different stages of the simulation. The RDF of the initial crystal substrate after equilibration, shown in Figure 5.9(d), exhibits clear peaks indicative of a perfect crystal. At the end of the deposition, Figure 5.9(e) shows broad close-distance peaks and only a weak further-distance (second neighbor) peak, indicating an amorphous structure. Then, the RDF after annealing, shown in Figure 5.9(f), has the regular peaks again, only slightly broadened from the before-deposition peaks, confirming that the material is in fact crystalline.

A close-up snapshot of the Ni-doped MoS_2 at the end of annealing stage is shown in Figure 5.10(a). This visual analysis suggests that most of the Ni atoms positioned themselves at Mo vacancies, resulting in a Mo-substituted Ni-doped MoS_2 structure. To confirm this, the distribution of Ni–S and Ni–Mo distances at the end of deposition and annealing are shown in Figure 5.10(b) and (c), respectively. The heights of the first Ni–S (black) and Ni–Mo (red) RDF peaks are comparable in the amorphous state but, after annealing, the Ni–S peak is much higher. This indicates that more of the Ni atoms are bonded to S, as opposed to Mo, consistent with the Mo-substituted Ni-doped MoS_2 structure. Previous DFT calculations have shown that under S-rich conditions, Mo-substituted is the most favorable doping location for Ni. [71] Visual analysis of the post-annealing simulations also indicated that the Ni atoms were not randomly distributed throughout the crystal, but rather formed few-atom clusters. This observation is consistent with phase separation predicted for Mo substitution according to convex hull analysis of DFT calculations.[71] Similar behavior has been previously observed for gold atoms co-sputtered with MoS_2, [301] which is further support for the physical realism of these simulations and the new force field.

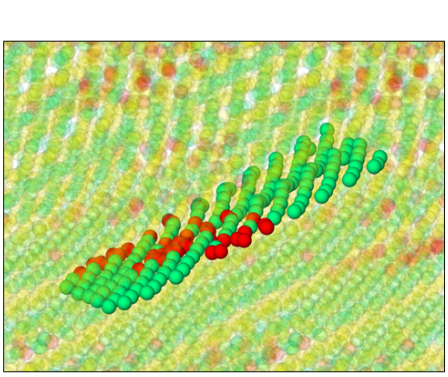

(a) Mo-substituted Ni-doped MoS_2

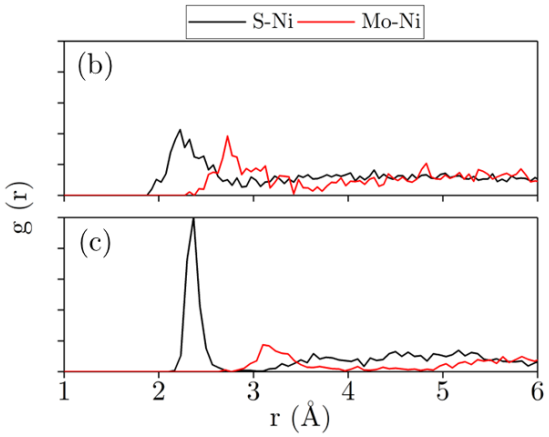

Figure 5.10: (a) Close-up snapshot of the model system at the end of the annealing stage with all atoms faded except for one Mo layer and the substituted Ni atoms. (b) Radial distribution function for Ni–Mo (red) and Ni–S (black) bonds at the end of (b) deposition and (c) annealing. This figure was partly created by Sergio Romero Garcia, Department of Mechanical Engineering, University of California, Merced.

5.4 Conclusion

Two new ReaxFF force fields were developed for Ni-doped MoS_2. The force fields were developed by adding the parameters for Ni-Mo-S, Ni-S-Mo, and S-Ni-Mo angles to a previously optimized force field for MoS_2, [138, 133] and tuning those parameters to match DFT-calculated energies. The parameterization was based on strained DFT calculations of Mo-substituted, S-substituted, octahedral, and tetrahedral intercalation structures of the Ni dopant. The final force field was able to accurately predict the lengths of Mo–Ni and S–Ni bonds as well as lattice constants, S–S distance, and interlayer separation. Furthermore, the developed force field agreed with DFT on the relaxed geometries of Ni-doped MoS_2 structures with vacancies. We note that the force field was not trained for interlayer sliding,[276] and our initial testing indicates that it was not be able to accurately capture sliding behavior for some dopant configurations; improvement of the force field to capture sliding energies could be considered in future work. However, the force field is robust for modeling the crystal structures of Ni-doped MoS_2 and their elastic behavior, as well as the phase transition between amorphous and crystalline, and also the underlying mechanisms of doping. The ReaxFF force fields developed in this work will enable future simulation-based studies of the fundamental mechanisms by which Ni dopants affect MoS_2 for applications in catalysis and tribological, as well as other possible new applications of the material.

5.5 Supporting information

5.5.1 Equation of state results from DFT and MD using the potential developed based on the 2017 ReaxFF MoS_2 parameters

Strained uniaxially in the x-direction

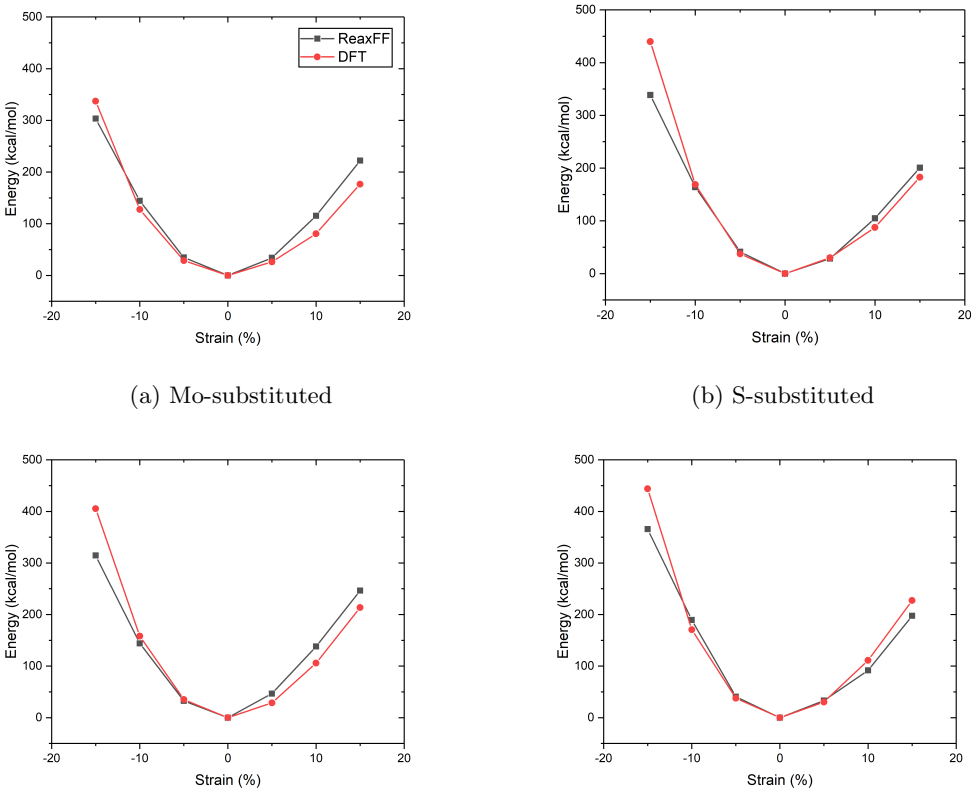

(a) Mo-substituted

(b) S-substituted

(c) Octahedral

(d) Tetrahedral

Figure 5.11: Equations of state calculated from DFT (red) and ReaxFF (black) for structures strained uniaxially in the x-direction. The DFT energies in this figure were obtained by Enrique Guerrero, Department of Physics, University of California, Merced.

Strained uniaxially in the z-direction

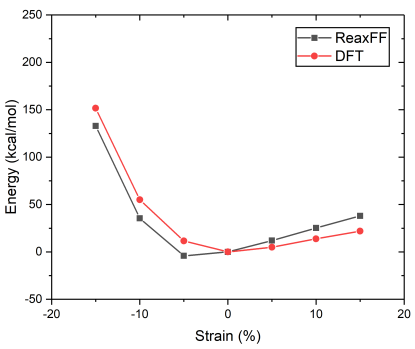

(a) Mo-substituted

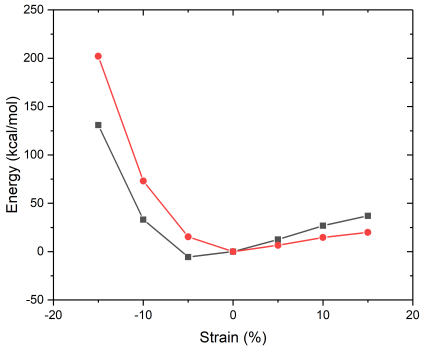

(b) S-substituted

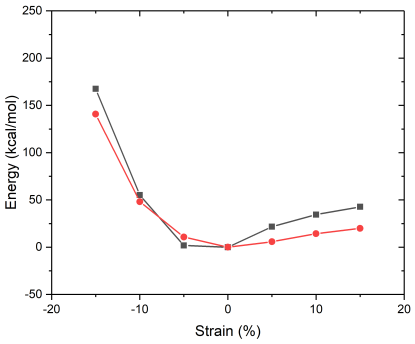

(c) Octahedral

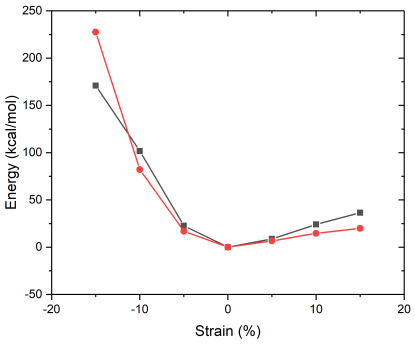

(d) Tetrahedral

Figure 5.12: Equations of state calculated from DFT (red) and ReaxFF (black) for structures strained uniaxially in the z-direction. The DFT energies in this figure were obtained by Enrique Guerrero, Department of Physics, University of California, Merced.

Strained biaxially in the xy-plane

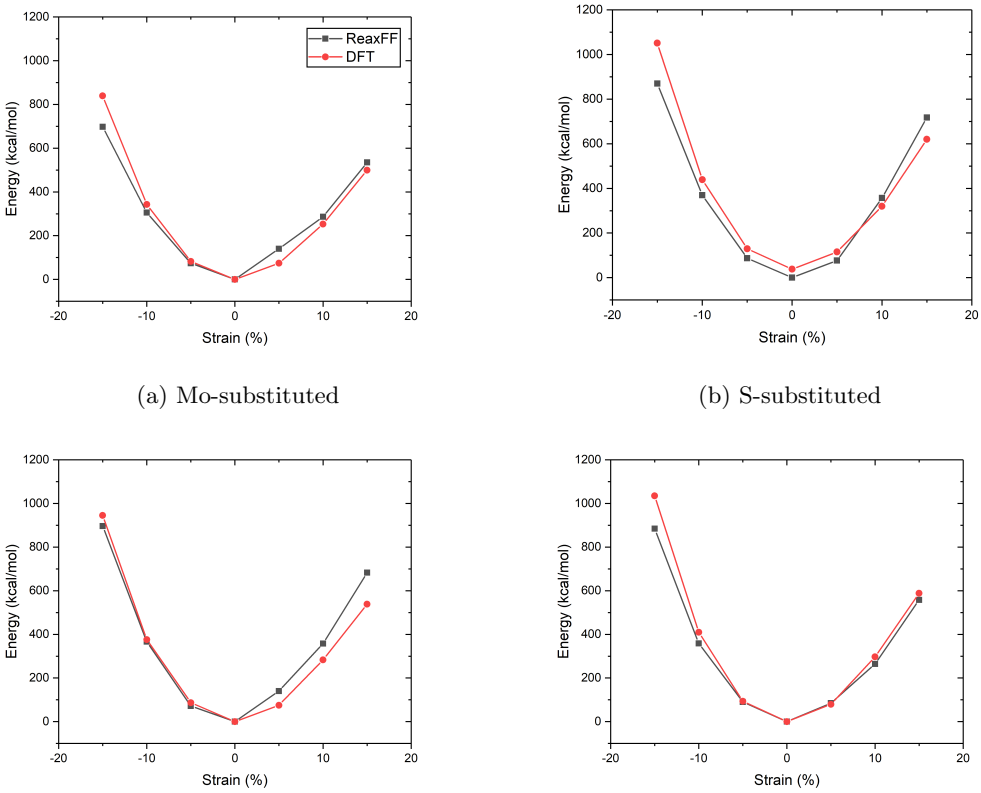

(a) Mo-substituted

(b) S-substituted

(c) Octahedral

(d) Tetrahedral

Figure 5.13: Equations of state calculated from DFT (red) and ReaxFF (black) for structures strained biaxially in the xy-plane. The DFT energies in this figure were obtained by Enrique Guerrero, Department of Physics, University of California, Merced.

Strained triaxially

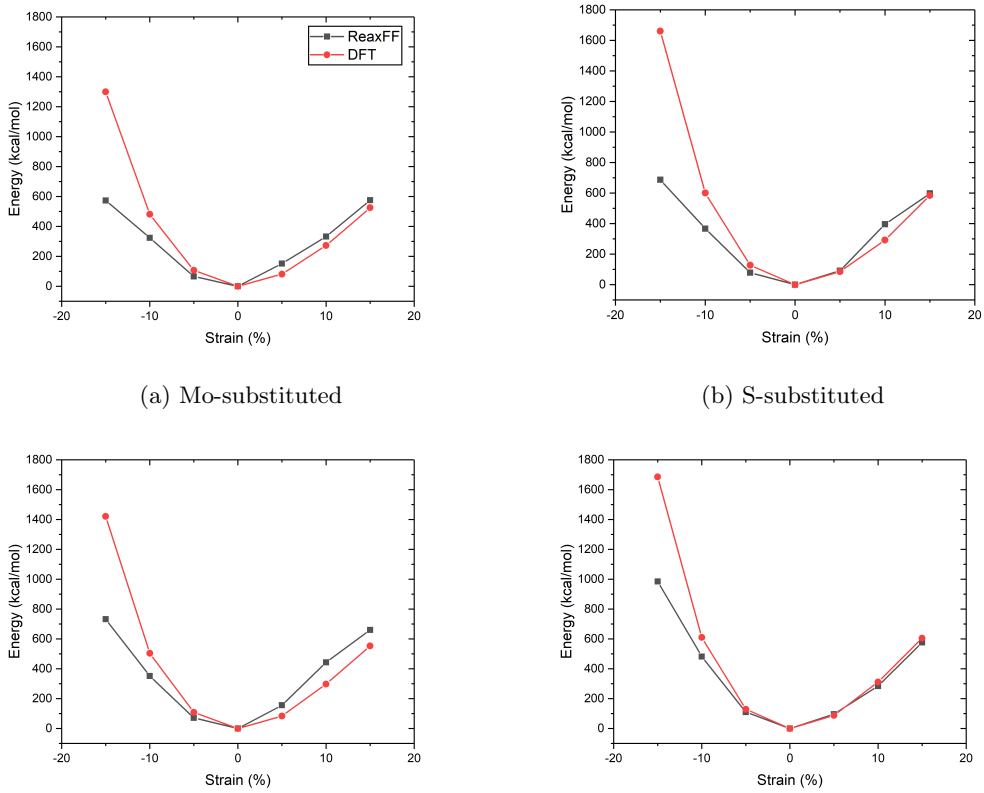

(a) Mo-substituted

(b) S-substituted

(c) Octahedral

(d) Tetrahedral

Figure 5.14: Equations of state calculated from DFT (red) and ReaxFF (black) for structures strained triaxially. The DFT energies in this figure were obtained by Enrique Guerrero, Department of Physics, University of California, Merced.

Sheared in the xy-plane

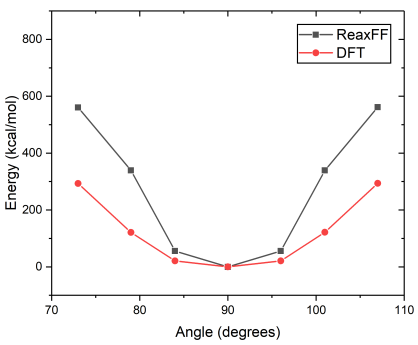

(a) Mo-substituted

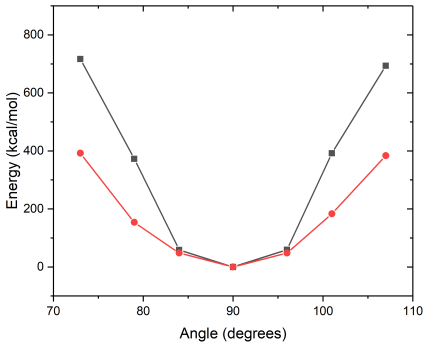

(b) S-substituted

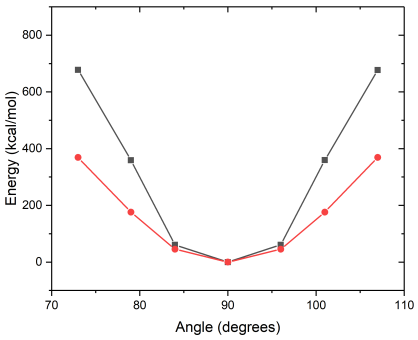

(c) Octahedral

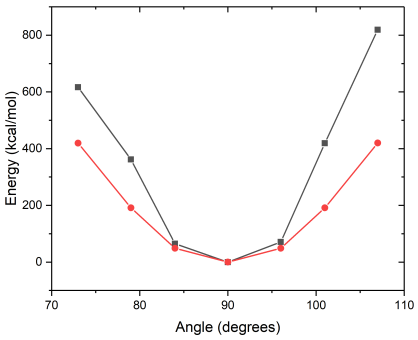

(d) Tetrahedral

Figure 5.15: Equations of state calculated from DFT (red) and ReaxFF (black) for structures sheared in the xy-plane. The DFT energies in this figure were obtained by Enrique Guerrero, Department of Physics, University of California, Merced.

Chapter 6

Summary, Next Steps, and Conclusions

6.1 Summary

This research aimed to study the fundamental mechanisms by which lubricant additives protect tribological surfaces. Specifically, sulfur-containing additives were investigated. sulfur is a key element in a family of lubricant additives that create protective films on mechanical components during operation to increase their life. These are EP and AW additives which are commonly used in many applications where the mechanical system is subject to high pressures, such as metalworking fluids, cutting tools, gear boxes, hydraulics, and more. Understanding the role of sulfur in creating protective films on a fundamental level can help engineers configure the lubrication formulation to optimize their performance as well as reduce their environmentally unfavorable byproducts.

Initially the reactions between di-*tert*-butyl disulfide, a common EP additive, and an iron surface were investigated using reactive MD simulations in chapter 2. Since reactive simulations use an empirical model (force field) to predict the behavior of the system on an atomic and molecular level, the accuracy of the force field was evaluated using DFT-based calculations. Next, a protocol was developed that emulated the process by which an additive interacts and reacts with tribological surfaces. Results showed that the reactions between a disulfide and an iron surface proceeds through three steps, namely, S–S bond cleavage, followed by Fe–S bond formation, and lastly, dissociation of the S–C bond. This is in agreement with a previously suggested reaction pathway. [39] Next, the rate-limiting step of the reaction was investigated. It was shown that the S–C bond dissociation, the last step to film formation, occurs slower than all other steps. Lastly, the friction reduction behavior of a sulfur-covered iron surface was studied. The sulfur-covered iron surface exhibited a coefficient of friction that was $\approx 50\%$ lower than a pure iron–iron contact.

It is known that some chemical reactions on tribological surfaces can be driven by mechanical force. In chapter 3, the effect of heat, load, and shear on chemical reactions between a disulfide additive and an iron surface was investigated. The reactions were studied at a range of temperatures (300–700 K) and at 1 GPa load. Additionally, the reactants were sheared to deconvolute the effect of shear from load and heat. Two sliding iron surfaces were created to simulate the movement of mechanical components during operation. Results showed that both heat and load accelerate the reaction. However, shear showed to drive the reaction at temperatures below the initiation reaction temperature. This confirms that the reaction between disulfides and iron surface can be driven mechanically at low temperatures and that the essence of the film formation reaction is mechanochemical in nature. To further determine *how* the reaction is driven by mechanical means and *how much* of the reaction is driven by mechanical forces (as opposed to heat), the reaction yield was studied in the context of an Arrhenius based model, Bell model, that relates the reaction yield to the shear that is driving the reaction. It was concluded that mechanical force drives the reactions that happen on the surface by lowering the reaction energy barrier and hence accelerating the reaction or making it possible for the reaction to occur at low temperatures when thermal energy is not enough to initiate the reaction. It was also shown that mechanical energy reduces the reaction energy barrier height by $\approx 20\%$.

In chapter 4, the reaction between disulfides and ferrous surfaces was investigated in more

realistic conditions. Disulfide additives are added to lubricant formulations to enhance their performance, however, most of the lubricant is base oil. Therefore, here, the interactions between di-*tert*-butyl disulfide and dodecane (a model base oil) were investigated. Additionally, in the real applications, iron surfaces are almost always covered with a thin oxide layer. Based on this, the reactions of the additive was investigated in the absence and presence of an iron oxide surface. Results showed that the base oil did not chemically react with either the additive or the surface and hence the presence of the base oil did not change the mechanism by which the iron sulfide film was formed. Consequently, the reaction proceeded through the same intermediate steps that were observed in previous chapters. Interestingly, the oxide surface introduced two new reaction pathways that lead to film formation. The presence of H and O near the reactants introduced many steps that involved oxidation and hydroxylation of either the additive or its products. The same main three reaction steps were identified for the reactions that occurred on the oxide surface, however, not necessarily in the order that was previously observed. Investigation of the reaction yield of the three steps showed that the S–C dissociation was still the rate-limiting step in all cases. While base oil did not chemically interfere with the reactions, it was observed that the physical presence of the dodecane molecule on the surface hindered the transfer of shear force to reacting molecule and consequently slowed the reaction rate's dependence on shear stress. Conversely, the presence of the oxygen and hydrogen and their products on the iron oxide surface significantly reduced the reactivity of the additive molecules, its derivative species, and the ferrous surface. The magnitude of the reduction in reaction yield was surprisingly more than 90% for some cases. This was in agreement with the experimental studies that showed the reactions of disulfides on the iron oxide surface are slower than that of iron. [243] Lastly, investigating the effect of shear on driving the reactions in the context of the Bell model revealed that the reaction occurs through lateral motion of the hydrocarbon group which results in cleavage of the S–C bond leading to iron sulfide film formation.

Finally, an investigation into another sulfur-containing lubricating compound, Ni-doped MoS_2, was carried out. Over the years, MoS_2 has shown to perform as an excellent solid lubricant, or in the nanoparticle form, as a lubricant additive. Ni dopant has shown to enhance the performance of MoS_2 in catalysis and tribology. To study the catalytic and tribological properties of Ni-doped MoS_2, reactive MD simulation can be a powerful tool, but there was previously no ReaxFF force field specifically developed for Ni-doped MoS_2. In chapter 5, a ReaxFF force field parameter set was optimized against extensive DFT calculations. Equations of state of a Ni-doped MoS_2 structure was used to train the ReaxFF force field. The force field showed an excellent agreement in the energies corresponding to straining and shearing the Ni-doped MoS_2 structure in different directions. Additionally, the force field was able to accurately predict the lengths of different bonds that exist within a Ni-doped MoS_2 structure. The developed force field also successfully predicted the lattice constants of the crystal structure as well as the transfer of Ni dopant due to defects such as vacancies. Additionally, the force field performed fairly in predicting the energies of a MoS_2 structure with an adatom at different doping sites for 1T and 1H polytypes.

Finally, the applicability and accuracy of the developed ReaxFF force field was demonstrated by performing a MD simulation of a crystallization procedure. The process included depositing Mo, Ni, and S atoms on a substrate to create an amorphous Ni-doped MoS_2 layer followed by an annealing process. Results showed that the developed force field was able to create a Ni-doped MoS_2 crystal from an amorphous structure and that the dominant dopant position was Mo-substitution.

6.2 Future work

This dissertation reports an extensive study carried out for sulfur-containing lubricant additives. The results of this work will add to an already extensive body of work in the literature. However, there remains more work to be done that can extend our fundamental understanding of the mechanisms by which sulfur-containing lubricant additives protect mechanical components. There are opportunities for improving our knowledge of tribology both in the case of liquid lubricant additives and solids.

6.2.1 Liquid lubricant additives

Research was carried out in this dissertation to identify and understand the mechanisms of film formation from the reactions between di-*tert*-butyl disulfide, an extreme-pressure additive, and ferrous surfaces. However, there is more to be done. Firstly, the effect of heat, load, and shear was investigated, however, the effect of sliding speed on this reaction is still unknown. Secondly, simulations were carried out in the presence of a base oil, dodecane. However, there are other base oils that are more commonly used in industry, for example, polyalphaolefin and phosphate ester. Thirdly, the weight ratio of the additive content used in this dissertation was 50%. However, a more realistic by weight ratio is less than 10%. This high ratio was chosen due to the time and size limitations of a molecular dynamics simulation. This was a first step towards understanding the role of base oil; next steps could be to use a more realistic weight ratio and take advantage of either accelerated MD methods and more efficient computational resources.

6.2.2 Solid lubricants

The Ni-doped MoS_2 ReaxFF force field that was developed in this dissertation enables reactive MD simulations of a this materials for various applications. There have been MoS_2 ReaxFF force fields that were previously developed in the literature. However, introduction of the Ni dopant to this force field can be utilized to improve our fundamental understanding of how dopants affect the performance of MoS_2. Another application of the force field could be to investigate the doping mechanisms under different deposition and or operating conditions, e.g different temperatures. Additionally, the developed force field can be used to study the enhanced catalytic properties of the doped MoS_2 and mechanisms behind it or to address the elastic response of the Ni-doped MoS_2 to mechanical stimuli. Finally, the develop force field, by itself, can be improved further. The current version of the force field does not include sliding, an important property that is inherent to tribological applications. If added, the force field can be used to model the material for applications that involve relative motion of surfaces.

6.3 Concluding words

The work done in this dissertation helped improve our fundamental understanding of sulfur-containing lubricant additives and the mechanisms by which they protect mechanical components during operation. Specifically, the following developments were made through the research. (i) A new simulation protocol was developed to study film formation from the chemical reactions that occur between additives and surfaces. (ii) The reaction pathway of a disulfide additive and iron surface was observed and compared to the pathway hypothesized previously based on experimental measurements. (iii) The rate limiting step of the reaction that leads to film formation was identified and the friction reduction behavior of the resulting sulfur-covered surface was investigated. (iv) The effects of heat, load, and shear on driving and accelerating the reaction was studied and the mechanism by which shear drives the tribological reaction was identified. (v) The role of a base oil as well as an oxide surface in modifying both the reaction pathways and the reaction rate was addressed. (vi) A new ReaxFF force field was developed that made the investigation of doped MoS_2 possible. (vii) A first step towards understanding the mechanism of crystallization of a doped MoS_2 was taken.

Finally, sulfur-containing additives and lubricants are widely used in applications, but there is a need for a fundamental understanding of the mechanisms by which they function. Particularly, new understanding can be used to optimize the efficiency of the lubrication formula or operating conditions, as well as potentially resolve concerns about toxicity and sustainability. The work presented in this dissertation provides such understanding that can be utilized as a baseline for future work towards more efficient and environmentally aware design of lubricant formulations.

Bibliography

[1] K. Mohammadtabar et al. “Reactive molecular dynamics simulations of thermal film growth from di-*tert*-butyl disulfide on an Fe(100) surface”. In: *Langmuir* 34 (2018), pp. 15681–15688.

[2] K. Mohammadtabar et al. “Heat-, load-, and shear-driven reactions of di-tert-butyl disulfide on Fe(100)”. In: *J. Phys. Chem. C* 123(32) (2019), pp. 19688–19692.

[3] Karen Mohammadtabar et al. “Shear-driven reactions of organosulfur compounds on ferrous surfaces: A molecular dynamics study”. In: *Tribology International* 176 (2022), p. 107922.

[4] A. Khajeh et al. “Statistical analysis of tri-cresyl phosphate conversion on an iron oxide surface using reactive molecular dynamics simulations”. In: *J. Phys. Chem. C* 123.20 (2019), pp. 12886–12893.

[5] E. Barraud et al. “Mechanically activated solid-state synthesis of hafnium carbide and hafnium nitride nanoparticles.” In: *J. Alloys Compd.* 456(1-2) (2008), pp. 224–233.

[6] M.K. Beyer and H. Clausen-Schaumann. “Mechanochemistry: the mechanical activation of covalent bonds.” In: *Chem. Rev.* 105(8) (2005), pp. 2921–2948.

[7] H.M. Klukovich et al. “A backbone lever-arm effect enhances polymer mechanochemistry.” In: *Nat. Chem.* 5(2) (2013), pp. 110–114.

[8] A.S. Duwez et al. “Mechanochemistry: targeted delivery of single molecules.” In: *Nat. Nanotechnol.* 1(2) (2006), pp. 122–125.

[9] C.R. Hickenboth et al. “Biasing reaction pathways with mechanical force.” In: *Nature* 446(7134) (2007), pp. 423–427.

[10] Douglas A Davis et al. “Force-induced activation of covalent bonds in mechanoresponsive polymeric materials”. In: *Nature* 459.7243 (2009), pp. 68–72.

[11] S. L. Potisek et al. “Mechanophore-linked addition polymers”. In: *J. Am. Chem. Soc.* 129.45 (2007), pp. 13808–13809.

[12] H. L. Adams et al. “Shear-induced mechanochemistry: Pushing molecules around”. In: *J. Phys. Chem. C* 119 (2015), pp. 7115–7123.

[13] Resham Rana et al. “Anisotropy of shear-induced mechanochemical reaction rates of surface adsorbates; Implications for theoretical models”. In: *The Journal of Physical Chemistry C* 126.28 (2022), pp. 11585–11593.

[14] A. Takacs. “The historical development of mechanochemistry”. In: *Chem. Soc. Rev.* 42 (2013), pp. 7649–7659.

[15] J. Yeon et al. “Mechanochemistry at solid surfaces: polymerization of adsorbed molecules by mechanical shear at tribological interfaces”. In: *ACS Appl. Mater. Int.* 9 (2017), pp. 3142–3148.

[16] H. Spikes. “Stress-augmented thermal activation: Tribology feels the force”. In: *Friction* 6(1) (2018), pp. 1–31.

[17] A. Stolle et al. “Ball milling in organic synthesis: solutions and challenges.” In: *Chem. Soc. Rev.* 40(5) (2011), pp. 2317–2329.

[18] Evelina Colacino et al. “Introducing students to mechanochemistry via environmentally friendly organic synthesis using a solvent-free mechanochemical preparation of the antidiabetic drug tolbutamide”. In: *Journal of Chemical Education* 96.4 (2019), pp. 766–771.

[19] V. Šepelák et al. “Mechanochemical reactions and syntheses of oxides”. In: *Chem. Soc. Rev.* 42 (2013), pp. 7507–7520.

[20] VV Zyryanov. “Mechanochemical synthesis of complex oxides”. In: *Russian chemical reviews* 77.2 (2008), p. 105.

[21] A.L. Garay, A. Pichon, and S.L. James. “Solvent-free synthesis of metal complexes.” In: *Chem. Soc. Rev.* 36(6) (2007), pp. 846–855.

[22] Mohammad Yaser Masoomi, Ali Morsali, and Peter C Junk. “Rapid mechanochemical synthesis of two new Cd (II)-based metal–organic frameworks with high removal efficiency of Congo red”. In: *CrystEngComm* 17.3 (2015), pp. 686–692.

[23] A. Bruckmann, A. Krebs, and C. Bolm. “Organocatalytic reactions: effects of ball milling, microwave and ultrasound irradiation.” In: *Green Chem.* 10(11) (2008), pp. 1131–1141.

[24] Dario Braga et al. “Mechanically induced expeditious and selective preparation of disubstituted pyridine/pyrimidine ferrocenyl complexes”. In: *Organometallics* 23.11 (2004), pp. 2810–2812.

[25] M. K. Beyer and H. Clausen-Schaumann. “Mechanochemistry: The mechanical activation of covalent bonds”. In: *Chem. Rev.* 105(8) (2004), pp. 2921–2948.

[26] B. M. Rosen and V. Percec. “A reaction to stress”. In: *Nature* 446 (2007), pp. 381–382.

[27] J.R. Felts et al. “Direct mechanochemical cleavage of functional groups from graphene”. In: *Nat. Commun.* 6 (2015), pp. 6467, 1–7.

[28] Xin He, Dien Ngo, and Seong H. Kim. “Mechanochemical reactions of adsorbates at tribological interfaces: Tribopolymerizations of allyl alcohol coadsorbed with water on silicon oxide”. In: *Langmuir* 35.48 (2019), pp. 15451–15458.

[29] A. Khajeh et al. “Mechanochemical association reaction of interfacial molecules driven by shear”. In: *Langmuir* 34 (2018), pp. 5971–5977.

[30] D.C. Sutton et al. “Interpreting the effects of interfacial chemistry on the tribology of diamond-like carbon coatings against steel in distilled water.” In: *Wear* 302(1-2) (2013), pp. 918–28.

[31] M.I. de BarrosBouchet et al. “Boundary lubrication mechanisms of carbon coatings by MoDTC and ZDDP additives.” In: *Tribol. Int.* 38(3) (2005), pp. 257–264.

[32] J. Fontaine, C. Donnet, and A. Erdemir. “Fundamentals of the tribology of DLC coatings. In Tribology of diamond-like carbon films”. In: *Springer, Boston, MA.* (2008), pp. 139–154.

[33] J.P. ed. Byers. “Metalworking fluids.” In: *crc Press* (2017).

[34] E. Brinksmeier et al. “Metalworking fluids—mechanisms and performance.” In: *CIRP Annals* 64(2) (2015), pp. 605–628.

[35] W. Dai et al. “Roles of nanoparticles in oil lubrication.” In: *Tribol. Int.* 102 (2016), pp. 88–98.

[36] J. Tannous et al. “Understanding the tribochemical mechanisms of IF-MoS 2 nanoparticles under boundary lubrication.” In: *Tribol. Lett.* 41(1) (2011), pp. 55–64.

[37] Y. Zhou and J. Qu. “Ionic liquids as lubricant additives: a review.” In: *ACS Appl. Mater. Interfaces* 9(4) (2017), pp. 3209–3222.

[38] V. Totolin et al. “Lubrication mechanism of phosphonium phosphate ionic liquid additive in alkylborane–imidazole complexes.” In: *Tribol. lett.* 53(2) (2014), pp. 421–432.

[39] T. Mang and W. Dresel. *Lubricants and lubrication.* John Wiley & Sons., 2007.

[40] Y. Zhou et al. “Understanding tribofilm formation mechanisms in ionic liquid lubrication.” In: *Sci. Rep.* 7(1) (2017), pp. 1–8.

[41] B. Li et al. “Tribochemistry and antiwear mechanism of organic–inorganic nanoparticles as lubricant additives.” In: *Tribol. Lett.* 22(1) (2006), pp. 79–84.

[42] Meini Yang et al. “In-situ synthesis of calcium borate/cellulose acetate-laurate nanocomposite as efficient extreme pressure and anti-wear lubricant additives”. In: *Int. J. Biol. Macromol.* 156 (2020), pp. 280–288.

[43] Md Hafizur Rahman et al. “Recent progress on phosphonium-based room temperature ionic liquids: Synthesis, properties, tribological performances and applications”. In: *Tribology International* 167 (2022), p. 107331.

[44] Arash Khajeh et al. “Thermal decomposition of phosphonium salicylate and phosphonium benzoate ionic liquids”. In: *Journal of Molecular Liquids* 352 (2022), p. 118700.

[45] AG Papay. “Antiwear and extreme-pressure additives in lubricants”. In: *Lubrication Science* 10.3 (1998), pp. 209–224.

[46] E.S. Forbes. “Antiwear and extreme pressure additives for lubricants.” In: *Tribology* 3(3) (1970), pp. 145–152.

[47] M. R. Vaziripereshk et al. “Solid lubrication with MoS_2: A review”. In: *Lubricants* 7(7) (2019), p. 57.

[48] Ming Shi et al. “Coal-derived synthetic graphite with high specific capacity and excellent cyclic stability as anode material for lithium-ion batteries”. In: *Fuel* 292 (2021), p. 120250.

[49] T. Sunil et al. “A critical review on solid lubricants.” In: *Int. J. Mech. Eng. Technol* 7 (2016), pp. 193–199.

[50] EW Roberts and MJ Todd. “Space and vacuum tribology”. In: *Wear* 136.1 (1990), pp. 157–167.

[51] Ye Sujuan and Zeng Xingrong. “Tribological properties of PTFE and PTFE composites at different temperatures”. In: *Tribology Transactions* 57.3 (2014), pp. 382–386.

[52] N.L. McCook et al. “Wear resistant solid lubricant coating made from PTFE and epoxy.” In: *Tribol. Lett.* 18(1) (2005), pp. 119–124.

[53] JA Conesa and R Font. “Polytetrafluoroethylene decomposition in air and nitrogen”. In: *Polymer Engineering & Science* 41.12 (2001), pp. 2137–2147.

[54] Thomas F Jaramillo et al. “Identification of active edge sites for electrochemical H2 evolution from MoS_2 nanocatalysts”. In: *science* 317.5834 (2007), pp. 100–102.

[55] Gwangsik Jeong et al. “Ni-Doped MoS_2 Nanoparticles Prepared via Core–Shell Nanoclusters and Catalytic Activity for Upgrading Heavy Oil”. In: *Energy Fuels* 32 (2018), pp. 9263–9270.

[56] Yasuhiro Araki, Kosaku Honna, and Hiromichi Shimada. “Formation and catalytic properties of edge-bonded molybdenum sulfide catalysts on TiO2”. In: *Journal of Catalysis* 207.2 (2002), pp. 361–370.

[57] Didhiti Bhattacharya et al. “Size-dependent optical properties of MoS_2 nanoparticles and their photo-catalytic applications”. In: *Nanotechnology* 31.14 (2020), p. 145701.

[58] J. Deng et al. “Triggering the electrocatalytic hydrogen evolution activity of the inert two-dimensional MoS_2 surface via single-atom metal doping.” In: *Energy Environ. Sci.* 8(5) (2015), pp. 1594–1601.

[59] X. Zong et al. “Visible light driven H_2 production in molecular systems employing colloidal MoS_2 nanoparticles as catalyst”. In: *Chem. Commun.* 30 (2009), pp. 4536–4538.

[60] M. J. Cuddy et al. “Fabrication and atomic structure of size-selected, layered MoS_2 clusters for catalysis”. In: *Nanoscale* 6(21) (2014), pp. 12463–12469.

[61] J. Mao et al. “The rise of two-dimensional MoS_2 for catalysis.” In: *Frontiers of Physics* 13(4) (2018), p. 138118.

[62] Sangita Kumari et al. “Direct growth of nanostructural MoS_2 over the *h*-BN nanoplatelets: An efficient heterostructure for visible light photoreduction of CO_2 to methanol”. In: *J. CO2 Util.* 42 (2020), p. 101345.

[63] Yifei Li et al. “The heterojunction between 3D ordered macroporous TiO_2 and MoS_2 nanosheets for enhancing visible-light driven CO_2 reduction”. In: *J. CO2 Util.* 51 (2021), p. 101648.

[64] Wei Chen et al. “Solid-state synthesis of ultrathin MoS_2 as a cocatalyst on mesoporous g-C_3N_4 for excellent enhancement of visible light photoactivity”. In: *J. Alloys Compd.* 836 (2020), p. 155401.

[65] B. Radisavljevic et al. “Single-layer MoS_2 transistors”. In: *Nat. Nanotechnol.* 6 (2011), pp. 147–150.

[66] H. Yuan et al. “Influence of metal–MoS_2 interface on MoS_2 transistor performance: Comparison of Ag and Ti contacts”. In: *ACS Appl. Mater. Interfaces* 7(2) (2015), pp. 1180–1187.

[67] A. M. van der Zande et al. “Grains and grain boundaries in highly crystalline monolayer molybdenum disulphide”. In: *Nat. Mater.* 12 (2013), pp. 554–561.

[68] S. Domı'nguez-Meister et al. “Solid lubricant behavior of MoS_2 and WSe_2-based nanocomposite coatings.” In: *Sci. Technol. Adv. Mater.* 18(1) (2017), pp. 122–133.

[69] Junde Guo et al. “The application of nano-MoS_2 quantum dots as liquid lubricant additive for tribological behavior improvement”. In: *Nanomaterials* 10.2 (2020), p. 200.

[70] Seyed Borhan Mousavi, Saeed Zeinali Heris, and Patrice Estellé. “Experimental comparison between ZnO and MoS_2 nanoparticles as additives on performance of diesel oil-based nano lubricant”. In: *Sci. Rep.* 10 (2020), p. 5813.

[71] Enrique Guerrero, Rijan Karkee, and David A Strubbe. “Phase stability and Raman/IR signatures of Ni-doped MoS_2 from DFT studies”. In: *J. Phys. Chem. C* 125 (2021), pp. 13401–13412.

[72] J.V. Lauritsen et al. “Location and coordination of promoter atoms in Co-and Ni-promoted MoS_2-based hydrotreating catalysts.” In: *J. Catal.* 249(2) (2007), pp. 220–233.

[73] D. Zhang et al. “Room-temperature SO_2 gas-sensing properties based on a metal-doped MoS_2 nanoflower: An experimental and density functional theory investigation”. In: *J. Mater. Chem. A* 5(39) (2017), pp. 20666–20677.

[74] M.A. Hamilton et al. “A possible link between macroscopic wear and temperature dependent friction behaviors of MoS 2 coatings.” In: *Tribol. Lett.* 32(2) (2008), pp. 91–98.

[75] P. Stoyanov et al. “Microtribological performance of Au–MoS 2 and Ti–MoS 2 coatings with varying contact pressure.” In: *Tribol. Lett.* 40(1) (2010), pp. 199–211.

[76] H. Li et al. “Exploring the tribophysics and tribochemistry of MoS 2 by sliding MoS_2/Ti composite coating under different humidity.” In: *Tribol. Lett.* 65(2) (2017), p. 38.

[77] A. Paul et al. “An improved solid lubricant for bearings operating in space and terrestrial environments.” In: *In 44th Aerospace Mechanisms Symposium* (2018), p. 141.

[78] B. C. Stupp. “Synergistic effects of metals co-sputtered with MoS_2”. In: *Thin Solid Films* 84(3) (1981), pp. 257–266.

[79] Naveenkumar Rajendhran et al. “Enhancing of the tribological characteristics of the lubricant oils using Ni-promoted MoS_2 nanosheets as nano-additives”. In: *Tribol. Int.* 118 (2018), pp. 314–328.

[80] J. S. Zabinski et al. “The effects of dopants on the chemistry and tribology of sputter-deposited MoS_2 films.” In: *Tribol. Trans.* 38(4) (1995), pp. 894–904.

[81] A. Vellore et al. “Ni-Doped MoS_2 dry film lubricant life.” In: *Adv. Mater. Interfaces* 7(22) (2020), p. 2001109.

[82] T. Z. Zou et al. “Friction and wear properties of electroless Ni-P-(IF-MoS_2) composite coatings in humid air and vacuum”. In: *J. Mater. Sci. Eng. A* 426(1-2) (2006), pp. 162–168.

[83] L. R. Rudnick. *Lubricant additives: Chemistry and applications*. CRC press, 2009.

[84] Z. Pawlak. “Tribochemistry of lubricating oils”. In: *Tribology and Interface Engineering Series, no. 45*. Ed. by B. J. Briscoe. Amsterdam, The Netherlands: Elsevier, 2003.

[85] V. Sharma et al. “Mechanism of tribofilm formation with P and S containing ionic liquids”. In: *Tribol. Int.* 92 (2015), pp. 353–364.

[86] V. Sharma et al. “Antiwear properties of binary ashless blend of phosphonium ionic liquids and borate esters in partially formulated oil (No Zn)”. In: *Tribol. Lett.* 67 (42 2019), pp. 1–13.

[87] S. Soltanahmadi et al. “Experimental Observation of Zinc Dialkyl Dithiophosphate (ZDDP)-Induced Iron Sulphide Formation”. In: *Appl. Surf. Sci.* 414 (2017), pp. 41–51.

[88] M. Rodríguez Ripoll et al. “Diallyl Disulphide as Natural Organosulphur Friction Modifier via the In-Situ Tribo-Chemical Formation of Tungsten Disulphide”. In: *Appl. Surf. Sci.* 428 (2018), pp. 659–668.

[89] Roman Heuberger, Antonella Rossi, and Nicholas D Spencer. "XPS study of the influence of temperature on ZnDTP tribofilm composition". In: *Tribology Letters* 25.3 (2007), pp. 185–196.

[90] Makoto Miyajima et al. "Structural characterization of iron sulfide tribofilms formed on carbon and stainless steels". In: (2022).

[91] Jinhua Ou et al. "Highly transparent nickel and iron sulfide on nitrogen-doped carbon films as counter electrodes for bifacial quantum dot sensitized solar cells". In: *Solar Energy* 193 (2019), pp. 766–773.

[92] Cyrus Wadia, A Paul Alivisatos, and Daniel M Kammen. "Materials availability expands the opportunity for large-scale photovoltaics deployment". In: *Environmental science & technology* 43.6 (2009), pp. 2072–2077.

[93] Tian Tian and Han-Qing Yu. "Iron-assisted biological wastewater treatment: synergistic effect between iron and microbes". In: *Biotechnology Advances* 44 (2020), p. 107610.

[94] Yaoning Chen et al. "Modification, application and reaction mechanisms of nano-sized iron sulfide particles for pollutant removal from soil and water: A review". In: *Chemical Engineering Journal* 362 (2019), pp. 144–159.

[95] Shujun Gao et al. "Formation of iron oxide and iron sulfide at high temperature and their effects on corrosion". In: *Corrosion Science* 135 (2018), pp. 167–176.

[96] Qiao Sun et al. "Ion-selectivity of iron sulfides and their effect on H2S corrosion". In: *Corrosion Science* 158 (2019), p. 108085.

[97] T Ocampo-Macias et al. "Synthesis of iron sulfide films through solid–gas reaction of iron with diethyl disulfide". In: *J. Sulfur Chem.* 36.4 (2015), pp. 385–394.

[98] K Sathickbasha et al. "Synergistic effect of bismuth III sulfide and iron sulfide in the tribological performance of brake friction composite". In: *Surface Topography: Metrology and Properties* 10.2 (2022), p. 025015.

[99] Mingsuo Zhang et al. "Hydrothermal synthesis and tribological properties of FeS 2 (pyrite)/ reduced graphene oxide heterojunction". In: *RSC Advances* 5.2 (2015), pp. 1417–1423.

[100] H. Wang et al. "The friction-reduction model of the iron sulfide film prepared by plasma source ion sulfuration". In: *Surf. Coat. Tech.* 201 (9-11 2007), pp. 5236–5239.

[101] J.R. Fehling and N.K. Sarkar. "The friction of copper-nickel and iron-sulfur alloys in air and vacuum". In: *Wear* 14.1 (1969), pp. 33–47.

[102] B. A. Baldwin. "Relationship between surface composition and wear: an X-ray photoelectron spectroscopic study of surfaces tested with organosulfur compounds". In: *ASLE Trans.* 19.4 (1976), pp. 335–344.

[103] Jie Zhang and Hugh Spikes. "On the Mechanism of ZDDP Antiwear Film Formation". In: *Tribol. Lett.* 63 (2016), p. 24.

[104] W. Tysoe. "On stress-induced tribochemical reaction rates". In: *Tribol. Lett.* 65 (2017), p. 48.

[105] J. Zhang et al. "Mechanochemistry of zinc dialkyldithiophosphate on steel surfaces under elastohydrodynamic lubrication conditions." In: *ACS Appl. Mater. Interfaces* 12(5) (2020), pp. 6662–6676.

[106] M. Ueda, A. Kadiric, and H. Spikes. "On the crystallinity and durability of ZDDP tribofilm." In: *Tribol. Lett.* 67(4) (2019), p. 123.

[107] N.N. Gosvami et al. "Mechanisms of antiwear tribofilm growth revealed *in situ* by single-asperity sliding contacts". In: *Science* 348 (2015), pp. 102–106.

[108] M. Ueda, A. Kadiric, and H. Spikes. "ZDDP tribofilm formation on non-ferrous surfaces." In: *Tribol. Online* 15(5) (2020), pp. 318–331.

[109] O.J. Furlong et al. "Low-temperature, shear-induced tribofilm formation from dimethyl disulfide on copper." In: *ACS Appl. Mater. Interfaces* 3(3) (2011), pp. 795–800.

[110] O. Furlong et al. "Shear and Thermal Effects in Boundary Film Formation During Sliding". In: *RSC Adv.* 4 (2014), pp. 24059–24066.

[111] O. Furlong, B. Miller, and W. T. Tysoe. "Shear-induced boundary film formation from dialkyl sulfides on copper". In: *Wear* 274–275, 27 (2012), pp. 183–187.

[112] G. Bell. “Models for the specific adhesion of cells to cells”. In: *Science* 200(4342) (1978), pp. 618–627.

[113] Alejandro Boscoboinik et al. “Measuring and modelling mechanochemical reaction kinetics”. In: *Chemical Communications* 56.56 (2020), pp. 7730–7733.

[114] R. J. Bird and G. D. Galvin. “The application of photoelectron spectroscopy to the study of E.P. films on lubricated surfaces”. In: *Wear* 37 (1976), pp. 143–167.

[115] D. R. Wheeler. “X-ray photoelectron spectroscopic study of surface chemistry of dibenzyl disulfide on steel under mild and severe wear conditions”. In: *Wear* 47.2 (1978), pp. 243–254.

[116] S. Plaza. “Some chemical reactions of organic disulfides in boundary lubrication”. In: *ASLE Trans.* 30.4 (1986), pp. 493–500.

[117] J. Zhang et al. “A study of 2-(n-alkyldithio)-benzoxazoles as novel additives”. In: *Tribol. Lett.* 7.4 (1999), pp. 173–177.

[118] M.N. Najman, M. Kasrai, and G.M. Bancroft. “X-ray absorption spectroscopy and atomic force microscopy of films generated from organosulfur extreme-pressure (EP) oil additives”. In: *Tribol. Lett.* 14 (2003), pp. 225–235.

[119] Z. Zhang et al. “Study of interaction of EP and AW additives with dispersants using XANES”. In: *Tribol. Lett.* 18.1 (2005), pp. 43–51.

[120] M. T. Costello and M. Kasrai. “Study of surface films of overbased sulfonates and sulfurized olefins by X-Ray Absorption Near Edge Structure (XANES) spectroscopy”. In: *Tribol. Lett.* 24.2 (2006), pp. 163–169.

[121] Resham Rana et al. “Critical stresses in mechanochemical reactions”. In: *Chemical Science* (2022).

[122] Mark H Dishner, John C Hemminger, and Frank J Feher. “Direct observation of substrate influence on chemisorption of methanethiol adsorbed from the gas phase onto the reconstructed Au (111) surface”. In: *Langmuir* 13.8 (1997), pp. 2318–2322.

[123] Ryo Yamada, Hiromi Wano, and Kohei Uosaki. “Effect of temperature on structure of the self-assembled monolayer of decanethiol on Au (111) surface”. In: *Langmuir* 16.13 (2000), pp. 5523–5525.

[124] J Christopher Love et al. “Self-assembled monolayers of thiolates on metals as a form of nanotechnology”. In: *Chem. rev.* 105.4 (2005), pp. 1103–1170.

[125] KF Khaled and Mohammed A Amin. “Corrosion monitoring of mild steel in sulphuric acid solutions in presence of some thiazole derivatives–molecular dynamics, chemical and electrochemical studies”. In: *Corros. Sci.* 51.9 (2009), pp. 1964–1975.

[126] Juanjuan Zhou et al. “Studies of protection of self-assembled films by 2-mercapto-5-methyl-1, 3, 4-thiadiazole on iron surface in 0.1 M H_2SO_4 solutions”. In: *J. Electroanal. Chem.* 612.2 (2008), pp. 257–268.

[127] A. C. T. van Duin et al. “ReaxFF: A reactive force field for hydrocarbons”. In: *Phys. Chem. A* 105 (2001), pp. 9396–9409.

[128] D.C. Yue et al. “Tribochemical mechanism of amorphous silica asperities in aqueous environment: a reactive molecular dynamics study.” In: *Langmuir* 31(4) (2015), pp. 1429–1436.

[129] J. Wen et al. “Atomistic insights into Cu chemical mechanical polishing mechanism in aqueous hydrogen peroxide and glycine: ReaxFF reactive molecular dynamics simulations.” In: *J. Phys. Chem. C* 123(43) (2019), pp. 26467–26474.

[130] A. Erdemir et al. “Carbon-based tribofilms from lubricating oils.” In: *Nature* 536(7614) (2016), pp. 67–71.

[131] A. Khajeh et al. “Mechanochemical association reaction of interfacial molecules driven by shear”. In: *Langmuir* 34.21 (2018), pp. 5971–5977.

[132] J.P. Ewen et al. “Substituent effects on the thermal decomposition of phosphate esters on ferrous surfaces.” In: *J. Phys. Chem. C* 124(18) (2020), pp. 9852–9865.

[133] A. Ostadhossein et al. “ReaxFF reactive force-field study of molybdenum disulfide (MoS_2).” In: *J. Phys. Chem. Lett.* 8(3) (2017), pp. 631–640.

[134] Tommi T. Jarvi et al. “Development of interatomic ReaxFF potentials for Au–S–C–H systems”. In: *J. Phys. Chem. A* 115 (2011), pp. 10315–10322.

[135] Gyun-Tack Bae and Christine M. Aikens. “Improved ReaxFF force field parameters for Au–S–C–H systems”. In: *J. Phys. Chem. A* 117 (2013), pp. 10438–10446.

[136] Velachi Vasumathi, José Luis Cagide Fajin, and Maria Natália Dias Soeiro Cordeiro. “How reliable is the ReaxFF potential for describing the structure of alkanethiols on gold? A molecular dynamics study”. In: *International Journal of Modeling, Simulation, and Scientific Computing* 5 (2014), p. 1441011.

[137] Jejoon Yeon et al. “Development of a ReaxFF force field for Cu/S/C/H and reactive MD simulations of methyl thiolate decomposition on Cu (100)”. In: *J. Phys. Chem. B* 122 (2018), p. 888.

[138] I Ponomarev, T Polcar, and P Nicolini. “New reactive force field for simulations of MoS_2 crystallization”. In: *J. Phys. Chem. C* (2022).

[139] R. Chen et al. “Formation of MoS_2 from elemental Mo and S using reactive molecular dynamics simulations.” In: *J. Vac. Sci. Technol., A* 38(2) (2020), p. 022201.

[140] S. Hong et al. “Computational synthesis of MoS_2 layers by reactive molecular dynamics simulations: initial sulfidation of MoO_3 surfaces.” In: *Nano Lett.* 17(8) (2017), pp. 4866–4872.

[141] R. Chen et al. “Limiting domain size of MoS_2: effects of stoichiometry and oxygen.” In: *J. Phys. Chem. C* (2020).

[142] G. Hu et al. “Predicting synthesizable multi-functional edge reconstructions in two-dimensional transition metal dichalcogenides.” In: *npj Comput. Mater.* 6(1) (2020), pp. 1–9.

[143] D. E. Yilmaz et al. “Defect design of two-dimensional MoS_2 structures by using a graphene layer and potato stamp concept.” In: *J. Phys. Chem. C* 122(22) (2018), pp. 11911–11917.

[144] T. K. Patra et al. “Defect dynamics in 2-D MoS_2 probed by using machine learning, atomistic simulations, and high-resolution microscopy.” In: *ACS nano* 12(8) (2018), pp. 8006–8016.

[145] Y. Shi et al. “Interfacial molecular deformation mechanism for low friction of MoS_2 determined using ReaxFF-MD simulation.” In: *Ceram. Int.* 45(2) (2019), pp. 2258–2265.

[146] Terence FJ Quinn. *Physical analysis for tribology*. Cambridge University Press, 2005.

[147] Yun Kyung Shin et al. “Development of a ReaxFF reactive force field for Fe/Cr/O/S and application to oxidation of butane over a pyrite-covered Cr_2O_3 catalyst”. In: *ACS Catal.* 5 (2015), pp. 7226–7236.

[148] M. Kaltchev et al. “A molecular beam study of the tribological chemistry of dialkyl disulfides”. In: *Tribol. Lett.* 10.1-2 (2001), pp. 45–50.

[149] A. Dorgham et al. “An *In situ* synchrotron XAS methodology for surface analysis under high temperature, pressure, and shear”. In: *Rev. Sci. Instrum.* 88 (2017), p. 015101.

[150] J. Tannous et al. “Contribution of gas phase lubrication in understanding tribochemistry of organosulphur compounds”. In: *Tribol.-Mater., Surf. Interfaces* 1.2 (2007), pp. 98–104.

[151] J. Lara et al. “Surface chemistry and extreme-pressure lubricant properties of dimethyl disulfide”. In: *J. Phys. Chem. B* 102.10 (1998), pp. 1703–1709.

[152] J. Lara et al. “The surface and tribological chemistry of carbon disulfide as an extreme-pressure additive”. In: *Wear* 239.1 (2000), pp. 77–82.

[153] Huai Sun. “COMPASS: an ab initio force-field optimized for condensed-phase applications overview with details on alkane and benzene compounds”. In: *J. Phys. Chem. B* 102.38 (1998), pp. 7338–7364.

[154] Thomas P Senftle et al. “The ReaxFF reactive force-field: development, applications and future directions”. In: *npj Comput. Mater.* 2 (2016), p. 15011.

[155] L. Qi and S. B. Sinnott. “Atomistic simulations of organic thin film deposition through hyperthermal cluster impacts”. In: *J. Vac. Sci. Technol., A* 16 (2002), p. 1293.

[156] L. Qi and S. B. Sinnott. “Generation of 3D hydrocarbon thin films via organic molecular cluster collisions”. In: *Surf. Sci.* 398.1–2 (1998), pp. 195–202.

[157] Y. Hu and S. B. Sinnott. “Molecular dynamics simulation of thin film nucleation through molecular cluster beam deposition: Effect of incident angle”. In: *Nucl. Instrum. Methods Phys. Res., Sect. B* 195.3–4 (2002), pp. 329–338.

[158] Mohammad Zarshenas et al. “Molecular dynamics simulations of hydrocarbon film growth from acetylene monomers and radicals: Effect of substrate temperature”. In: *J. Phys. Chem. C* 122.27 (2018), pp. 15252–15263.

[159] Chenyu Zou and Adri C. T. van Duin. “Investigation of complex iron surface catalytic chemistry using the ReaxFF reactive force field method”. In: *JOM* 64 (2012), pp. 1426–1437.

[160] Chenyu Zou, Adri C. T. van Duin, and Dan C. Sorescu. “Theoretical Investigation of Hydrogen Adsorption and Dissociation on Iron and Iron Carbide Surfaces Using the ReaxFF Reactive Force Field Method”. In: *Top. Catal.* 55 (2012), pp. 391–401.

[161] Md Mahbubul Islam et al. “Interactions of hydrogen with the iron and iron carbide interfaces: a ReaxFF molecular dynamics study”. In: *Phys. Chem. Chem. Phys.* 18 (2016), pp. 761–771.

[162] G. Kresse and J. Hafner. “Ab initio molecular dynamics for liquid metals”. In: *Phys. Rev. B* 47(1) (1993), pp. 558–561.

[163] G Kresse and J Hafner. “Norm-conserving and ultrasoft pseudopotentials for first-row and transition elements”. In: *J. Phys.: Condens. Matter* 6(40) (1994), pp. 8245–8257.

[164] G. Kresse and J. Hafner. “Ab initio molecular-dynamics simulation of the liquid-metal–amorphous-semiconductor transition in germanium”. In: *Phys. Rev. B* 49(20) (1994), pp. 14251–14269.

[165] Georg Kresse and Jürgen Furthmüller. “Efficient iterative schemes for ab initio total-energy calculations using a plane-wave basis set”. In: *Phys. Rev. B* 54.16 (1996), p. 11169.

[166] G. Kresse and J. Furthmüller. “Efficiency of ab-initio total energy calculations for metals and semiconductors using a plane-wave basis set”. In: *Comput. Mater. Sci.* 6(1) (1996), pp. 15–50.

[167] G. Kresse and D. Joubert. “From ultrasoft pseudopotentials to the projector augmented-wave method”. In: *Phys. Rev. B* 59(3) (1999), pp. 1758–1775.

[168] P. E. Blöchl. “Projector augmented-wave method”. In: *Phys. Rev. B* 50(24) (1994), pp. 17953–17979.

[169] A. D. Becke. “On the large-gradient behavior of the density functional exchange energy”. In: *J. Chem. Phys.* 85(12) (1986), pp. 7184–7187.

[170] Jiři Klimeš, David R Bowler, and Angelos Michaelides. “Chemical accuracy for the van der Waals density functional”. In: *J. Phys.: Condens. Matter* 22(2) (2009), p. 022201.

[171] Jiři Klimeš, David R. Bowler, and Angelos Michaelides. “Van der Waals density functionals applied to solids”. In: *Phys. Rev. B* 83(19) (2011).

[172] Hendrik J. Monkhorst and James D. Pack. “Special points for Brillouin-zone integrations”. In: *Phys. Rev. B* 13(12) (1976), pp. 5188–5192.

[173] M. Methfessel and A. T. Paxton. “High-precision sampling for Brillouin-zone integration in metals”. In: *Phys. Rev. B* 40(6) (1989), pp. 3616–3621.

[174] QuantumATK 2017.0. “Synopsys QuantumATK”. In: (), https://www.synopsys.com/ silicon/quantumatk.html.

[175] Sunghwan Kim et al. “PubChem substance and compound databases”. In: *Nucleic Acids Res.* 44.D1 (2016), pp. D1202–D1213.

[176] S. Plimpton. “Fast parallel algorithms for short-range molecular dynamics”. In: *J. Comp. Phys.* 117 (1995), pp. 1–19.

[177] Alexander Stukowski. “Visualization and analysis of atomistic simulation data with OVITO–the open visualization tool”. In: *Model. Simul. Mater. Sci. Eng.* 18 (2010), pp. 015012, 1–7.

[178] Stefan J Eder et al. “Thermostat influence on the structural development and material removal during abrasion of nanocrystalline ferrite”. In: *ACS Appl. Mater. Interfaces* 9.15 (2017), pp. 13713–13725.

[179] Fabrice Dénès et al. “Thiyl Radicals in Organic Synthesis”. In: *Chem. Rev.* 114 (2014), pp. 2587–2693.

[180] Stefan J Eder, András Vernes, and Gerhard Betz. “On the Derjaguin offset in boundary-lubricated nanotribological systems”. In: *Langmuir* 29.45 (2013), pp. 13760–13772.

[181] M. L. S. Fuller et al. “Solution Decomposition of Zinc Dialkyl Dithiophosphate and Its Effect on Antiwear and Thermal Film Formation Studied by X-Ray Absorption Spectroscopy”. In: *Tribol. Int.* 31 (1998), pp. 627–644.

[182] J.M. Martin. “Antiwear mechanisms of zinc dithiophosphate: A chemical hardness approach”. In: *Tribol. Lett.* 6 (1999), pp. 1–8.

[183] B. H. Kim, V. Sharma, and P. B. Aswath. “Chemical and mechanistic interpretation of thermal films formed by dithiophosphates using XANES”. In: *Tribol. Int.* 114 (2017), pp. 15–26.

[184] R. Heuberger, A. Rossi, and N. Spencer. “XPS Study of the Influence of Temperature on ZnDTP Tribofilm Composition”. In: *Tribol. Lett.* 25 (2007), pp. 185–196.

[185] R. Heuberger, A. Rossi, and N. Spencer. “Pressure Dependence of ZnDTP Tribochemical Film Formation: A Combinatorial Approach”. In: *Tribol. Lett.* 28 (2007), pp. 209–222.

[186] J. Zhang and H. Spikes. “On the mechanism of ZDDP antiwear film formation”. In: *Tribol. Lett.* 63 (2016), p. 24.

[187] A. Ghanbarzadeh et al. “A semi-deterministic wear model considering the effect of zinc dialkyl dithiophosphate tribofilm”. In: *Tribol. Lett.* 61 (2016), pp. 12, 1–15.

[188] X. Liu et al. “Local chemo-mechanical insights into the efficacy of ZDDP additives from *in situ* single asperity growth and mechanical testing”. In: *Tribol. Int.* 112 (2017), pp. 103–107.

[189] H. Spikes and W. T. Tysoe. “On the commonality between theoretical models for fluid and solid friction, wear and tribochemistry”. In: *Tribol. Lett.* 59 (2015), pp. 21, 1–14.

[190] C. Minfray et al. “Experimental and molecular dynamics simulations of tribochemical reactions with ZDDP: Zinc phosphate-iron oxide reaction”. In: *Tribol. Trans.* 51 (5 2008), pp. 589–601.

[191] I. Minami et al. “Investigation of wear mechanism by organic sulphides in vegetable oils”. In: *Lubr. Sci.* 19 (2007), pp. 113–126.

[192] W. Davey and E. D. Edwards. “The extreme-pressure lubricating properties of some sulphides and disulphides, in mineral oil, as assessed by the four-ball machine”. In: *Wear* 1 (1958), pp. 291–304.

[193] L. Martinez et al. “Packmol: A package for building initial configurations for molecular dynamics simulations”. In: *J. Comput. Chem.* 30(13) (2009), pp. 2157–2164.

[194] A. Khajeh, J. Krim, and A. Martini. “Synergistic effect of nanodiamonds on the adsorption of tricresyl phosphate on iron oxide surfaces”. In: *Appl. Phys. Lett.* 114.171602 (2019), pp. 1–4.

[195] V. Šepelák et al. “Mechanochemical reactions and syntheses of oxides”. In: *Chem. Soc. Rev.* 42 (2013), pp. 7507–7520.

[196] M. M. Caruso et al. “Mechanically-induced chemical changes in polymeric materials.” In: *Chem. Rev.* 109, 11 (2009), pp. 5755–5798.

[197] N. Haruta et al. “Force-induced dissolution of imaginary mode in mechanochemical reaction: Dibenzophenazine synthesis”. In: *J. Phys. Chem. C* 123.35 (2019), pp. 21581–21587.

[198] C. R. Hickenboth et al. “Biasing reaction pathways with mechanical force”. In: *Nature* 446.7134 (2007), pp. 423–427.

[199] K. L. Berkowski et al. “Ultrasound-induced site-specific cleavage of azo-functionalized poly (ethylene glycol)”. In: *Macromolecules* 38.22 (2005), pp. 8975–8978.

[200] A. Martini, S. J. Eder, and N. Dörr. “Tribochemistry: A review of reactive molecular dynamics simulations”. In: *Lubricants* 8 (2020), p. 44.

[201] J. Zhao et al. “Friction-induced nano-structural evolution of graphene as a lubrication additive.” In: *Appl. Surf. Sci.* 434 (2018), pp. 21–27.

[202] H. Spikes. “Stress-augmented thermal activation: Tribology feels the force”. In: *Friction* 6(1) (2018), pp. 1–31.

[203] A. Martini and S. H. Kim. “Activation volume in shear-driven chemical reactions”. In: *Tribol. Lett.* 69.4 (2021), pp. 1–14.

[204] L. Wang et al. “High temperature lubrication and mechanism of sodium carbonate by interface tailoring”. In: *Appl. Surf. Sci.* 530 (2020), p. 147288.

[205] P. Seema, J. Behler, and D. Marx. “Force-induced mechanical response of molecule–metal interfaces: Molecular nanomechanics of propanethiolate self-assembled monolayers on Au(111).” In: *Phys. Chem. Chem. Phys.* 15(38) (2013), pp. 16001–16011.

[206] R. Rana and W. Tysoe. “Tribochemical mechanisms of trimethyl and triethyl phosphite on oxidized iron in ultrahigh vacuum.” In: *Tribol. Lett.* 67(3) (2019), p. 93.

[207] S. Loehlé and M.C. Righi. “First principles study of organophosphorus additives in boundary lubrication conditions: Effects of hydrocarbon chain length.” In: *Lubr. Sci.* 29(7) (2017), pp. 485–491.

[208] D.C. Yue et al. “Tribochemical mechanism of amorphous silica asperities in aqueous environment: A reactive molecular dynamics study”. In: *Langmuir* 31.4 (2015), pp. 1429–1436.

[209] P. A. Romero et al. “Atomistic insights into lubricated tungsten/diamond sliding contacts”. In: *Front. Mech. Eng.* 5 (2019), p. 6.

[210] J. P. Ewen et al. “Substituent effects on the thermal decomposition of phosphate esters on ferrous surfaces”. In: *J. Phys. Chem. C* 124.18 (2020), pp. 9852–9865.

[211] J. Wen et al. “Atomistic insights into Cu chemical mechanical polishing mechanism in aqueous hydrogen peroxide and glycine: ReaxFF reactive molecular dynamics simulations”. In: *J. Phys. Chem. C* 123 (2019), pp. 26467–26474.

[212] J. Yeon et al. “Development of a ReaxFF force field for Cu/S/C/H and reactive MD simulations of methyl thiolate decomposition on Cu(100)”. In: *J. Phys. Chem. B* 122(2) (2018), pp. 888–896.

[213] C. Kajdas, M. Makowska, and M. Gradkowski. “Tribochemistry of n-hexadecane in different material systems”. In: *Lubr. Sci.* 18.4 (2006), pp. 255–263.

[214] M. Makowska, C. Kajdas, and M. Gradkowski. “Mechanism of boundary film formation from n-hexadecane”. In: *Lubr. Sci.* 16.2 (2004), pp. 101–110.

[215] C. Kajdas, M. Makowska, and M. Gradkowski. “Influence of temperature on the tribochemical reactions of hexadecane”. In: *Lubr. Sci.* 15.4 (2003), pp. 329–340.

[216] P. Stoyanov et al. “Friction and wear mechanisms of tungsten–carbon systems: A comparison of dry and lubricated conditions”. In: *ACS Appl. Mater. Interfaces* 5.13 (2013), pp. 6123–6135.

[217] P. Stoyanov et al. “Nanoscale sliding friction phenomena at the interface of diamond-like carbon and tungsten”. In: *Acta Mater.* 67 (2014), pp. 395–408.

[218] S. M. Hsu and R. S. Gates. “Effect of materials on tribochemical reactions between hydrocarbons and surfaces”. In: *J. Phys. D: Appl. Phys.* 39.15 (2006), p. 3128.

[219] S. M. Hsu and E. E. Klaus. “Estimation of the molecular junction temperatures in four-ball contacts by chemical reaction rate studies”. In: *ASLE Trans.* 21.3 (1978), pp. 201–210.

[220] J. P. Ewen et al. “Nonequilibrium molecular dynamics simulations of stearic acid adsorbed on iron surfaces with nanoscale roughness”. In: *Tribol. Int.* 107 (2017), pp. 264–273.

[221] S. Loehlé and M. C. Righi. “Ab initio molecular dynamics simulation of tribochemical reactions involving phosphorus additives at sliding iron interfaces”. In: *Lubricants* 6.2 (2018), p. 31.

[222] S. Peeters et al. “Tribochemical reactions of MoDTC lubricant additives with iron by quantum mechanics/molecular mechanics simulations”. In: *J. Phys. Chem. A* 124.25 (2020), pp. 13688–13694.

[223] A. E. Elkholy, S. A. Rizk, and A. M. Rashad. “Enhancing lubricating oil properties using novel quinazolinone derivatives: DFT study and molecular dynamics simulation”. In: *J. Mol. Struct.* 1175 (2019), pp. 788–796.

[224] H. Berro, N. Fillot, and P. Vergne. “Molecular dynamics simulation of surface energy and ZDDP effects on friction in nano-scale lubricated contacts”. In: *Tribol. Int.* 43.10 (2010), pp. 1811–1822.

[225] T. Onodera et al. “A theoretical investigation on the abrasive wear prevention mechanism of ZDDP and ZP tribofilms”. In: *Appl. Surf. Sci.* 254.23 (2008), pp. 7976–7979.

[226] J. Shen et al. “Study on the relationship between extreme pressure properties and component contents of high pressured sulfurized isobutylene”. In: *Ind. Lubr. Tribol.* (2018).

[227] E. S. Forbes. “The load-carrying action of organo-sulphur compounds—a review”. In: *Wear* 15.2 (1970), pp. 87–96.

[228] N. Farzi, M. H. Hydarifar, and M. E. Izadi. “The investigation of surface corrosion of Fe_3C in H_2SO_4 solution and the role of thiophene as an inhibitor by ReaxFF molecular dynamics”. In: *Mater. Chem. Phys.* 283 (2022), p. 125984.

[229] X. Wang, X. Xue, and C. Zhang. “Early events of the carburization of Fe nanoparticles in ethylene pyrolysis: Reactive force field molecular dynamics simulations”. In: *J. Phys. Chem. C* 122.20 (2018), pp. 10835–10845.

[230] P. O. Bedolla et al. “Density functional investigation of the adsorption of isooctane, ethanol, and acetic acid on a water-covered Fe(100) surface”. In: *J. Phys. Chem. C* 118.37 (2014), pp. 21428–21437.

[231] J. M. Rhodes et al. “Phase-controlled colloidal syntheses of iron sulfide nanocrystals via sulfur precursor reactivity and direct pyrite precipitation”. In: *Chem. Mater.* 29.19 (2017), pp. 8521–8530.

[232] T. Ocampo-Macias et al. “Synthesis of iron sulfide films through solid–gas reaction of iron with diethyl disulfide”. In: *J. Sulfur Chem.* 36.4 (2015), pp. 385–394.

[233] A. N. Suarez et al. “The influence of base oil polarity on the tribological performance of zinc dialkyl dithiophospate additives”. In: *Tribol. Int.* 43.12 (2010), pp. 2268–2278.

[234] J. Lin, L. Wang, and G. Chen. “Modification of graphene platelets and their tribological properties as a lubricant additive”. In: *Tribol. Lett.* 41.1 (2011), pp. 209–215.

[235] J. Lara et al. “The surface and tribological chemistry of carbon disulfide as an extreme-pressure additive”. In: *Wear* 239.1 (2000), pp. 77–82.

[236] H. Fujita, R. P. Glovnea, and H. A. Spikes. “Study of zinc dialkydithiophosphate anti-wear film formation and removal processes, part I: Experimental”. In: *Tribol. Trans.* 48.4 (2005), pp. 558–566.

[237] A. Jabbarzadeh, P. Harrowell, and R. I. Tanner. “Very low friction state of a dodecane film confined between mica surfaces”. In: *Phys. Rev. Lett.* 94.12 (2005), p. 126103.

[238] P. A. Willermet, L. R. Mahoney, and C. M. Haas. “The effects of antioxidant reactions on the wear behavior of a zinc dialkyldithiophosphate”. In: *ASLE Trans.* 22.4 (1979), pp. 301–306.

[239] P. A. Willermet, L. R. Mahoney, and C. M. Bishop. “Lubricant degradation and wear III. Antioxidant reactions and wear behavior of a zinc dialkyldithiophosphate in a fully formulated lubricant”. In: *ASLE Trans.* 23.3 (1980), pp. 225–231.

[240] M. Masuko et al. “Fundamental study of changes in friction and wear characteristics due to ZnDTP deterioration in simulating engine oil degradation during use”. In: *Tribol. Ser.* 43 (2003). Elsevier, pp. 359–366.

[241] T. Sakurai, S. Ikeda, and H. Okabe. “The mechanism of reaction of sulfur compounds with steel surface during boundary lubrication, using S35 as a tracer”. In: *ASLE Trans.* 5.1 (1962), pp. 67–74.

[242] M. Tomaru, S. Hironaka, and T. Sakurai. “Effects of oxygen on the load-carrying action of some additives”. In: *Wear* 41.1 (1977), pp. 117–140.

[243] S. Hironaka, Y. Yahagi, and T. Sakurai. “Effects of adsorption of some surfactants on antiwear properties”. In: *ASLE Trans.* 21.3 (1978), pp. 231–235.

[244] T. Yamaguchi, T. Jin, and K. Tanabe. “Structure of acid sites on sulfur-promoted iron oxide”. In: *J. Phys. Chem.* 90.14 (1986), pp. 3148–3152.

[245] J. P. Guthrie and R. T. Gallant. "Thermodynamics of methanesulfonic acid revisited". In: *Can. J. Chem.* 78.10 (2000), pp. 1295–1298.

[246] Wen-Ching Hung et al. "Photoionization spectra and ionization thresholds of CH_3SO, CH_3SOH, and CH_3SS (O) CH_3". In: *J. Chem. Phys.* 105.17 (1996), pp. 7402–7411.

[247] Y. Zhang et al. "One step synthesis of ZnO nanoparticles from ZDDP and its tribological properties in steel-aluminum contacts." In: *Tribol. int.* 141 (2020), p. 105890.

[248] Y. Tian and R. Boulatov. "Comparison of the predictive performance of the Bell–Evans, Taylor-expansion and statistical-mechanics models of mechanochemistry". In: *Chem. Commun.* 49 (2013), pp. 4187–4189.

[249] C. A. Latorre et al. "Mechanochemistry of phosphate esters confined between sliding iron surfaces". In: *Commun. Chem.* 4.1 (2021), pp. 1–11.

[250] A. Dorgham et al. "Single-asperity study of the reaction kinetics of P-based triboreactive films". In: *Tribol. Int.* 133 (2019), pp. 288–296.

[251] T.S. Ko et al. "Electrical and optical properties of Co-doped and undoped MoS_2." In: *Jpn. J. Appl. Phys.* 55(4S) (2016), 04EP06.

[252] Y.C. Xie and Y.M. Li. "Preparation of Ni-doped MoS_2 microsphere and its superior electrocatalytic hydrogen evolution ability." In: *Adv. Mater. Res.* 871 (2014), pp. 206–210.

[253] Ogulcan Acikgoz et al. "Intercalation leads to inverse layer dependence of friction on chemically doped MoS_2". In: *Nanotechnology* 34.1 (2022), p. 015706. DOI: 10.1088/1361-6528/ac9393. URL: https://doi.org/10.1088/1361-6528/ac9393.

[254] Xiangbin Kong et al. "Ni-doped MoS_2 as an efficient catalyst for electrochemical hydrogen evolution in alkine media". In: *ChemistrySelect* 3.32 (2018), pp. 9493–9498.

[255] Rijan Karkee, Enrique Guerrero, and David A Strubbe. "Enhanced interlayer interactions in Ni-doped MoS_2, and structural and electronic signatures of doping site". In: *Phys. Rev. Materials* 5 (2021), p. 074006.

[256] N. Kondekar et al. "The Effect of Nickel on MoS_2 Growth Revealed with in Situ Transmission Electron Microscopy." In: *ACS Nano* 13(6) (2019), pp. 7117–7126.

[257] Xiao Zhang, Ping Yang, and San Ping Jiang. "Ni diffusion in vertical growth of MoS_2 nanosheets on carbon nanotubes towards highly efficient hydrogen evolution". In: *Carbon* 175 (2021), pp. 176–186.

[258] P. Sundara Venkatesh et al. "Transition metal doped MoS_2 nanosheets for electrocatalytic hydrogen evolution reaction". In: *Int. J. Hydrog. Energy* (2022).

[259] Uday Narayan Pan et al. "Covalent doping of Ni and P on 1T-enriched MoS_2 bifunctional 2D-nanostructures with active basal planes and expanded interlayers boosts electrocatalytic water splitting". In: *J. Mater. Chem. A* 8.37 (2020), pp. 19654–19664.

[260] Yimin Jiang et al. "Metal-semiconductor 1T/2H-MoS_2 by a heteroatom-doping strategy for enhanced electrocatalytic hydrogen evolution". In: *Catal. Commun.* 156 (2021), p. 106325.

[261] D. Geng, X. Bo, and L. Guo. "Ni-doped molybdenum disulfide nanoparticles anchored on reduced graphene oxide as novel electroactive material for a non-enzymatic glucose sensor." In: *Sens. Actuators, B* 244 (2017), pp. 131–141.

[262] D. Escalera-López et al. "Enhancement of the hydrogen evolution reaction from Ni-MoS_2 hybrid nanoclusters." In: *ACS Catal.* 6(9) (2016), pp. 6008–6017.

[263] D. Wang et al. "Ni-doped MoS_2 nanoparticles as highly active hydrogen evolution electrocatalysts". In: *RSC Adv.* 6(20) (2016), pp. 16656–16661.

[264] J. Zhang et al. "Engineering water dissociation sites in MoS_2 nanosheets for accelerated electrocatalytic hydrogen production". In: *Energy Environ. Sci.* 9(9) (2016), pp. 2789–2793.

[265] Jie Xu et al. "Frenkel-defected monolayer MoS_2 catalysts for efficient hydrogen evolution". In: *Nat. Commmun.* 13.1 (2022), pp. 1–8.

[266] Tao Dong et al. "Formation of Ni-doped MoS_2 nanosheets on N-doped carbon nanotubes towards superior hydrogen evolution". In: *Electrochim. Acta* 338 (2020), p. 135885.

[267] MI Khan et al. “Effect of Ni doping on the structural, optical and photocatalytic activity of MoS_2, prepared by Hydrothermal method”. In: *Mater. Res. Express* 7.1 (2020), p. 015061.

[268] Ningning Xuan et al. “Single-atom electroplating on two dimensional materials”. In: *Chem. Mater.* 31.2 (2018), pp. 429–435.

[269] Ran Zhang et al. “Insights into the sandwich-like ultrathin Ni-doped MoS_2/rGO hybrid as effective sulfur hosts with excellent adsorption and electrocatalysis effects for lithium-sulfur batteries”. In: *J. Energy Chem.* 60 (2021), pp. 85–94.

[270] M Arockia Jenisha et al. “Interfacial engineering effect and bipolar conduction of Ni-doped MoS_2 nanostructures for thermoelectric application”. In: *J. Alloys Compd.* 895 (2022), p. 162493.

[271] H. Wang et al. “Transition-metal doped edge sites in vertically aligned MoS_2 catalysts for enhanced hydrogen evolution”. In: *Nano Res.* 8(2) (2015), pp. 566–575.

[272] H. Wei et al. “A DFT study on the adsorption of H_2S and SO_2 on Ni doped MoS_2 monolayer”. In: *Nanomaterials* 8(9) (2018), p. 646.

[273] D. Ma et al. “The adsorption of CO and NO on the MoS_2 monolayer doped with Au, Pt, Pd, or Ni: A first-principles study.” In: *Appl. Surf. Sci.* 383 (2016), pp. 98–105.

[274] P. Raybaud et al. “Structure, energetics, and electronic properties of the surface of a promoted MoS_2 catalyst: an ab initio local density functional study”. In: *J. Catal.* 190(1) (2000), pp. 128–143.

[275] Yu Hao et al. “1T-MoS_2 monolayer doped with isolated Ni atoms as highly active hydrogen evolution catalysts: A density functional study”. In: *Appl. Surf. Sci.* 469 (2019), pp. 292–297.

[276] Enrique Guerrero and David A. Strubbe. “Atomistic mechanisms of sliding in few-layer and bulk doped MoS_2”. In: *arXiv:2209.15629* (2022). DOI: 10.48550/ARXIV.2209.15629.

[277] Rijan Karkee and David A. Strubbe. “Panoply of doping-induced reconstructions and electronic phases in Ni-doped 1T-MoS_2”. In: *arXiv:2107.07541* (2022). submitted 11 Mar 2022, https://doi.org/10.48550/arXiv.2107.07541. DOI: 10.48550/ARXIV.2107.07541. URL: https://arxiv.org/abs/2107.07541.

[278] Jin-Wu Jiang, Harold S Park, and Timon Rabczuk. “Molecular dynamics simulations of single-layer molybdenum disulphide (MoS_2): Stillinger-Weber parametrization, mechanical properties, and thermal conductivity”. In: *J. Appl. Phys.* 114.6 (2013), p. 064307.

[279] Jin-Wu Jiang and Yu-Ping Zhou. “Parameterization of Stillinger-Weber potential for two-dimensional atomic crystals”. In: *Handbook of Stillinger-Weber Potential Parameters for Two-Dimensional Atomic Crystals*. Ed. by Jin-Wu Jiang and Yu-Ping Zhou. Rijeka: IntechOpen, 2017. Chap. 1. DOI: 10.5772/intechopen.71929. URL: https://doi.org/10.5772/intechopen.71929.

[280] Tao Liang, Simon R Phillpot, and Susan B Sinnott. “Parametrization of a reactive many-body potential for Mo–S systems”. In: *Phys. Rev. B* 79.24 (2009), p. 245110.

[281] Rimei Chen et al. “Formation of MoS_2 from elemental Mo and S using reactive molecular dynamics simulations”. In: *J. Vac. Sci. Technol. A* 38.2 (2020), p. 022201.

[282] Hamidreza Noori et al. “Nanopore creation in MoS_2 and graphene monolayers by nanoparticles impact: a reactive molecular dynamics study”. In: *Appl. Phys. A* 127.7 (2021), pp. 1–13.

[283] Reza Khademi Zahedi et al. “Mechanical properties of all MoS_2 monolayer heterostructures: crack propagation and existing notch study”. In: *Comput. Mater. Contin.* 70.3 (2022), pp. 4635–4655.

[284] Sergio Mejıa-Rosales et al. “Mechanical properties of MoS_2 nanotubes under tension: a molecular dynamics study”. In: *Mol. Simul.* 47.6 (2021), pp. 471–479.

[285] Bohayra Mortazavi et al. “Mechanical response of all-MoS_2 single-layer heterostructures: a ReaxFF investigation”. In: *Phys. Chem. Chem. Phys.* 18.34 (2016), pp. 23695–23701.

[286] P Giannozzi et al. “Advanced Capabilities for Materials Modelling with QUANTUM ESPRESSO”. In: *J. Phys.: Condens. Matter* 29 (2017), p. 465901. DOI: 10.1088/1361-648X/aa8f79.

[287] John P. Perdew, Kieron Burke, and Matthias Ernzerhof. "Generalized gradient approximation made simple". In: *Phys. Rev. Lett.* 77 (1996), pp. 3865–3868. DOI: 10.1103/PhysRevLett.77.3865.

[288] Stefan Grimme. "Semiempirical GGA-type density functional constructed with a long-range dispersion correction". In: *J. Comput. Chem.* 27.15 (2006), pp. 1787–1799. DOI: 10.1002/jcc.20495.

[289] D. R. Hamann. "Optimized norm-conserving Vanderbilt pseudopotentials". In: *Phys. Rev. B* 88 (8 2013), p. 085117. DOI: 10.1103/PhysRevB.88.085117.

[290] Martin Schlipf and François Gygi. "Optimization algorithm for the generation of ONCV pseudopotentials". In: *Comput. Phys. Commun.* 196 (2015), pp. 36–44. DOI: 10.1016/j.cpc.2015.05.011.

[291] Alex Vasenkov et al. "Reactive molecular dynamics study of Mo-based alloys under high-pressure, high-temperature conditions". In: *J. Appl. Phys.* 112.1 (2012), p. 013511.

[292] Hsiu-Pin Chen et al. "Embrittlement of metal by solute segregation-induced amorphization". In: *Phys. Rev. Lett.* 104.15 (2010), p. 155502.

[293] Adri CT van Duin, Jan MA Baas, and Bastiaan Van De Graaf. "Delft molecular mechanics: a new approach to hydrocarbon force fields. Inclusion of a geometry-dependent charge calculation". In: *J. Chem. Soc., Faraday Trans.* 90.19 (1994), pp. 2881–2895.

[294] J. E. Mueller, A. C. van Duin, and W. A. Goddard III. "Development and validation of ReaxFF reactive force field for hydrocarbon chemistry catalyzed by nickel." In: *J. Phys. Chem. C* 114(11) (2010), pp. 4939–4949.

[295] Seung Ho Hahn et al. "Development of a ReaxFF reactive force field for $NaSiO_x$/water systems and its application to sodium and proton self-diffusion". In: *J. Phys. Chem. C* 122.34 (2018), pp. 19613–19624.

[296] Nadire Nayir, Adri CT Van Duin, and Sakir Erkoc. "Development of the Reaxff reactive force field for inherent point defects in the Si/silica system". In: *J. Phys. Chem. A* 123.19 (2019), pp. 4303–4313.

[297] Wu Zhou et al. "Intrinsic structural defects in monolayer molybdenum disulfide". In: *Nano Lett.* 13.6 (2013), pp. 2615–2622.

[298] Benjamin Sirota, Nicholas Glavin, and Andrey A Voevodin. "Room temperature magnetron sputtering and laser annealing of ultrathin MoS_2 for flexible transistors". In: *Vacuum* 160 (2019), pp. 133–138.

[299] Masafumi Taguchi and Satoshi Hamaguchi. "MD simulations of amorphous SiO_2 thin film formation in reactive sputtering deposition processes". In: *Thin Solid Films* 515.12 (Apr. 2007), pp. 4879–4882.

[300] Michael E McConney et al. "Direct synthesis of ultra-thin large area transition metal dichalcogenides and their heterostructures on stretchable polymer surfaces". In: *Journal of Materials Research* 31.7 (2016), pp. 967–974.

[301] T W Scharf et al. "Synthesis of Au-MoS(2) nanocomposites: thermal and friction-induced changes to the structure". en. In: *ACS Appl. Mater. Interfaces* 5.22 (Nov. 2013), pp. 11762–11767.